

THERMAL CONDUCTIVITY OF EARTH MATERIALS
AT HIGH TEMPERATURES

by

JOHN FRANK SCHATZ

B.S., Massachusetts Institute of Technology
(1964)

SUBMITTED IN
PARTIAL FULFILLMENT
OF THE REQUIREMENTS FOR THE
DEGREE OF DOCTOR OF PHILOSOPHY

at the

MASSACHUSETTS INSTITUTE OF TECHNOLOGY
June, 1971

Signature of Author.....
Department of Earth and Planetary Sciences, May 21, 1971

Certified by.....
Thesis Supervisor

Accepted by.....
Chairman, Departmental Committee on Graduate Students

Lindgren



Abstract

Thermal Conductivity of Earth Materials
at High Temperatures

by

John Frank Schatz

Submitted to the Department of Earth and
Planetary Sciences on May 21, 1971
in partial fulfillment of the requirements
for the degree of Doctor of Philosophy.

The total thermal conductivity (lattice plus radiative) of several important earth materials is measured in the temperature range 500°K to 1900°K . A new technique is described which uses a CO_2 laser to generate a low frequency temperature wave at one face of a small, disk-shaped sample, and an infrared detector focused on the other face to detect the phase of the emerging radiation. A mathematical expression is derived which enables phase data at several frequencies to be used for the simultaneous determination of the thermal diffusivity and mean extinction coefficient of the sample. The lattice and radiative thermal conductivities may then be calculated.

Results for single crystal and polycrystalline forsterite-rich olivines indicate that, even in relatively pure, large-grained material, the radiative conductivity does not increase rapidly with temperature. The predicted total thermal conductivity at 500 km depth in the earth's mantle is less than twice the surface olivine value of about $0.012 \text{ cal cm}^{-1} \text{ sec}^{-1} \text{ }^{\circ}\text{C}^{-1}$.

Thesis Supervisor: Gene Simmons

Title: Professor of Geophysics

Acknowledgements

This work is the result of more than three years of thought and experimentation, including at least two complete rebuildings of the apparatus. Throughout it all, the seemingly infinite patience of my advisor, Professor Gene Simmons, has been amazing, and I thank him for it. Professor Dave Strangway planted the initial idea, and it has grown to a degree I think he never expected. Dr. Paul Hoff showed me how to build the laser, giving freely of his time and spare parts. John Smith taught me a great deal about experimental electronics and Pete McFarlin provided x-ray and thin section analyses. I have also benefitted by discussions with Dr. Dave Jackson (who provided the aluminum oxide and forsterite samples), Dr. Sean Solomon, Dr. James Aronson, Norman Sleep, and Paul Kasameyer. Metaphysical guidance was provided by my wife, Mary.

Most of this work was done while the author held a National Science Foundation Graduate Fellowship. The experiment was supported by the National Aeronautics and Space Administration under contract NAS 9-8102.

TABLE OF CONTENTS

| | Page |
|---|------|
| Abstract | 2 |
| Acknowledgements | 3 |
| List of Figures | 6 |
| List of Tables | 10 |
| Introduction | 12 |
| 1. Mechanisms of heat transport in solids | 14 |
| 2. Lattice thermal conductivity | 21 |
| Phonon mean free path | 22 |
| Effect of temperature and pressure | 25 |
| Lattice conductivity in the mantle | 29 |
| 3. Radiative thermal conductivity | 35 |
| Radiation heat flux in a solid | 36 |
| Scattering | 50 |
| Absorption | 57 |
| Effect of temperature and pressure | 60 |
| 4. Experimental method | 68 |
| General remarks | 68 |
| Background of the new technique | 76 |
| Description of apparatus | 78 |
| 5. Mathematical analysis | 96 |
| Radiation at the detector | 99 |
| Temperature in the sample | 105 |
| Phase of the output signal | 114 |
| Method of data reduction | 116 |

| | Page |
|---|------|
| 6. Results | 119 |
| Discussion | 156 |
| Thermal conductivity of mantle olivine | 159 |
| 7. Geophysical applications | 167 |
| Thermal Conductivity and temperature in the upper mantle | 168 |
| Thermal conductivity in the moon | 175 |
| Temperature field of a downgoing slab | 175 |
| Summary | 183 |
| References | 186 |
| Appendix | 195 |
| Biographical Note | 199 |

LIST OF FIGURES

| | Page |
|---|------|
| 2.1 Lattice thermal conductivity of olivine as a function of temperature. | 28 |
| 2.2 Example of a calculation of lattice thermal conductivity as a function of depth in the mantle. | 32 |
| 3.1 Geometry of medium for calculation of radiation heat flux. | 39 |
| 3.2 Black body emission at various temperatures compared to typical absorption spectrum of olivine. | 47 |
| 3.3 Radiative thermal conductivity as a function of temperature for several values of mean extinction coefficient. | 49 |
| 3.4 The quantity $\bar{s}d$ for scattering in a large-grained particle assemblage as a function of relative refractive index of the grains. | 53 |
| 3.5 Extinction efficiency for a porous small-grained particle assemblage as a function of the parameter p . | 56 |
| 3.6 Absorption spectra of olivine at high temperatures. | 62 |
| 3.7 Mean extinction coefficient in olivine as a | |

| | |
|--|------------|
| function of temperature. | Page 64 |
| 3.8 Radiative thermal conductivity in olivine as a function of temperature and pressure. | 66 |
| 4.1 Geometry of medium for idealized thermal conductivity experiment. | 72 |
| 4.2 Schematic diagram of experimental apparatus. | 81 |
| 4.3 Detail of furnace tube. | 86 |
| 4.4 Detector electronic circuitry. | 90 |
| 4.5 Detector sensitivity and lens transmission as functions of wavelength. | 93 |
| 4.6 Example of recorder output, idealized. | 95 |
| 5.1 Illustration of the physical process of the experiment. | 98 |
| 5.2 Spectral extinction coefficient of a hypothetical material for use in comparison of definitions of mean extinction coefficient. | 104 |
| 5.3 Example of method of obtaining solutions for photon mean free path, $1/\bar{\epsilon}$, and lattice thermal diffusivity, κ_L . | 118 |
| 6.1 Photon mean free path in sintered aluminum oxide, Al_2O_3 . | 123 |
| 6.2 Total and radiative thermal conductivities in sintered aluminum oxide, Al_2O_3 . | 125 |
| 6.3 Photon mean free path in sintered forsterite, $Fo=Mg_2SiO_4$. | 129 |
| 6.4 Total and radiative thermal conductivities | |

| | Page |
|--|------|
| in sintered forsterite, $\text{Fo}=\text{Mg}_2\text{SiO}_4$. | 131 |
| 6.5 Photon mean free path in olivine single crystal, $\text{Fo}_{86}\text{Fa}_{14}$. | 135 |
| 6.6 Total and radiative thermal conductivities in olivine single crystal, $\text{Fo}_{86}\text{Fa}_{14}$. | 137 |
| 6.7 Photon mean free path in olivine single crystal, $\text{Fo}_{92}\text{Fa}_8$. | 141 |
| 6.8 Total and radiative thermal conductivities in olivine single crystal $\text{Fo}_{92}\text{Fa}_8$. | 143 |
| 6.9 Photon mean free path in twin sisters dunite, $\text{Fo}_{95}\text{Fa}_5$. | 147 |
| 6.10 Total and radiative thermal conductivities in twin sisters dunite, $\text{Fo}_{95}\text{Fa}_5$. | 149 |
| 6.11 Photon mean free path in enstatite, $\text{En}_{90}\text{Fs}_{10}$. | 153 |
| 6.12 Total and radiative thermal conductivities in enstatite $\text{En}_{90}\text{Fs}_{10}$. | 155 |
| 6.13 Summary of photon mean free path as a function of temperature in olivines, including hypothetical mantle material. | 161 |
| 6.14 Summary of lattice thermal conductivity as a function of temperature in olivines, including hypothetical mantle material. | 163 |
| 6.15 Total and radiative conductivities of hypothetical mantle material as functions of temperature. | 166 |

Page

| | |
|---|-----|
| 7.1 Thermal conductivity in the upper mantle. | 172 |
| 7.2 Temperature in the upper mantle. | 174 |
| 7.3 Temperature in the moon. | 177 |
| 7.4 Thermal conductivity in the moon. | 179 |
| 7.5 Temperature field of a downgoing slab at t = 9.45 m.y. | 182 |

LIST OF TABLES

| | Page |
|--|------|
| 2.1 Parameters used in calculation of lattice thermal conductivity in the mantle. | 33 |
| 6.1 Description of sample, aluminum oxide Al_2O_3 , sintered. | 120 |
| 6.2 Results for aluminum oxide Al_2O_3 , sintered, range of good solutions at 90% confidence interval. | 121 |
| 6.3 Description of sample, forsterite $\text{Fo}=\text{Mg}_2\text{SiO}_4$, sintered. | 126 |
| 6.4 Results for forsterite $\text{Fo}=\text{Mg}_2\text{SiO}_4$, sintered, range of good solutions at 90% confidence interval. | 127 |
| 6.5 Description of sample, olivine $\text{Fo}_{86}\text{Fa}_{14}$, single crystal. | 132 |
| 6.6 Results for olivine $\text{Fo}_{86}\text{Fa}_{14}$, single crystal, range of good solutions at 90% confidence interval. | 133 |
| 6.7 Description of sample, olivine $\text{Fo}_{92}\text{Fa}_8$, single crystal. | 138 |
| 6.8 Results for olivine $\text{Fo}_{92}\text{Fa}_8$, single crystal, range of good solutions at 90% confidence interval. | 139 |
| 6.9 Description of sample, dunite, twin sisters, $\text{Fo}_{95}\text{Fa}_5$. | 144 |

Page

| | | |
|------|--|-----|
| 6.10 | Results for dunite, twin sisters $\text{Fo}_{95}\text{Fa}_5$, range of good solutions at 90% confidence interval. | 145 |
| 6.11 | Description of sample, enstatite $\text{En}_{90}\text{Fs}_{10}$, single crystal. | 150 |
| 6.12 | Results for enstatite $\text{En}_{90}\text{Fs}_{10}$, single crystal, range of good solutions at 90% confidence interval. | 151 |
| 7.1 | Properties of models used in upper mantle temperature calculations. | 169 |

INTRODUCTION

An evolving planetary interior is a giant heat engine. A fundamental aspect of that engine is the total effect of the three modes of internal heat transport: conduction, radiation, and convection. This work is a contribution to the understanding of two of those modes, conduction and radiation, in solid earth materials and in the earth's mantle. A new experimental technique is described which facilitates the separation of the effects of conduction and radiation in partially transparent solids at high temperatures.

A precise knowledge of the magnitude of the parameters of conductive and radiative heat transport is more important in some calculations than in others. One calculation sensitive to these parameters is that of the temperature in the upper mantle (to about 600 km), where changes in thermal transport may affect the formation of a partial melt or phase change. Another is the temperature field of a downgoing slab (in plate tectonics), as considered by Minear and Toksöz [1970] and Toksöz, Minear, and Julian [1971], where the heating rate in and near to the slab is important to the prediction of geophysical effects. Calculations less sensitive to the parameters of conductive and radiative heat transport are often those involving the entire thermal history of a planet [MacDonald, 1959, 1963; Lubimova, 1967; Kopal,

1964; Lee, 1968]. In these large-scale calculations, other considerations, such as initial conditions, the existence and extent of convective motion, chemical reactions, and the distribution of sources of heat, are likely to be more important.

The experimental results obtained in this work are used to study temperatures in the earth's upper mantle, the moon, and the downgoing slab. But, the primary purpose of this investigation is to contribute to the general understanding of heat transport in earth materials, for any application.

1. MECHANISMS OF HEAT TRANSPORT IN SOLIDS

Consider the time dependent heat flow equation for solids without convective motion or internal sources of heat (which can be added later):

$$\rho C_p \frac{\partial T}{\partial t} = - \nabla \cdot Q \quad (1.1)$$

where ρ is the density, C_p is the specific heat at constant pressure, and Q is the net flux of heat at a point in the solid. For the case of simultaneous conduction and radiation of heat, Q may be separated into two parts as

$$Q = -K \nabla T + Q_R \quad (1.2)$$

where K is the usual thermal conductivity and Q_R is the unspecified (for now) radiative heat flux. K is, in general, the sum effect of several conductive mechanisms and Q_R is a complicated function of the geometric and radiative properties of the medium. Suppose for the moment that Q_R can be expressed in a manner analogous to normal conduction as

$$Q_R = -K_R \nabla T \quad (1.3)$$

where K_R is the "radiative conductivity". Then, if the conductivities are weak functions of position compared to temperature, equation (1.1) becomes the normal heat flow equation,

$$\rho C_p \frac{\partial T}{\partial t} = (K + K_R) \nabla^2 T \quad (1.4)$$

but with an effective conductivity $(K + K_R)$ [Clark, 1957]. The assumptions leading to this extremely simplified view of radiative heat transfer will be discussed later. It is sufficient here to note that equation (1.4) (with the addition, if necessary of sources and convection), is valid for the study of the earth's interior. However, it is generally not applicable to the reduction of data from high temperature laboratory experiments which use either small samples or time dependent boundary conditions.

If, as in equation (1.4) a conductivity can be associated with each mechanism of heat transport, then classical kinetic theory provides a simple method of evaluating that conductivity. For general reference, see Kittel [1966]. Each mechanism is considered to consist of a cloud of particles which move, collide, and carry heat such that

$$K = \frac{1}{3} C_v V L \quad (1.5)$$

where C_v is the local specific heat per unit volume (at constant volume), V is a characteristic particle speed, and L is the mean free path between collisions. The major assumptions implicit in this method are that each particle is in thermodynamic equilibrium with respect to its immediate surroundings and that the mean free path is much smaller than the external dimensions of the medium. The kinetic formula, equation (1.5), then provides a convenient method of comparison of conductivity mechanisms. But in order to use this theory to evaluate the thermal conductivities in earth materials, all of the mechanisms that are possibly important must be identified.

The types of heat-carrying quasi-particles may be divided into two groups according to the nature of their excitation energy: those which have a continuum of excited states immediately above the ground state and those which have a distinct energy gap between the ground and first excited state [Krumhansl, 1959; Whitmore, 1960]. Because increased particle excitation is produced mainly by increase of temperature, the continuum particles may be important at any temperature while the energy gap particles are important primarily

at high temperatures. Major representatives of continuum particles are phonons (quantized lattice vibrations) and photons (quantized electromagnetic radiation). Important examples of energy gap particles are free carriers (electrons, holes, and electron-hole pairs) and excitons (bound electron-hole pairs).

If numerous and mobile, energy gap particles can be major contributors to thermal conduction. It is not surprising that their influence upon heat conduction in the earth has been the subject of considerable discussion and some speculation. See, for example, Lawson and Jamieson [1958] and Lubimova [1960, 1967]. The contribution of free carriers may be estimated by the Wiedemann-Franz law or an appropriate modification thereof. See the text by Smith [1961] for a good discussion. The electrical conductivity in the mantle does not appear to exceed roughly 1 to 10 $\text{ohm}^{-1}\text{cm}^{-1}$ [Madden and Swift, 1969]. It is several orders of magnitude less in the moon [Sonett et al., 1971]. The associated thermal conductivity is almost certainly negligible.

Evaluation of the exciton contribution is a somewhat more difficult problem. The main questions are whether or not excitons exist at all in the insulating oxides and silicates, and if they do, what their excitation energies are. Any expression for the exciton thermal conductivity contains, by the kinetic

formula, a term proportional to the number of excitons which depends upon $e^{-E/kT}$, where E is the excitation energy. This exponential dominates the temperature dependence. If E is of the order of 1 ev, exciton thermal conductivity could be important in the earth, but if E is of the order of 10 ev this form of conductivity is almost certainly negligible. Shankland, [1968] has shown that the first important exciton energy in the forsterite lattice is at least 8 ev. Any excitons of lower energy would probably have insufficient mobility to contribute significantly to thermal conductivity. Exciton conductivity in olivines thus seems unlikely. Discussions in the ceramic and semi-conductor literature [Joffe, 1956; Whitmore, 1960; Lee and Kingery, 1960] lead to similar conclusions. In particular, Vishnevskii and Skripak [1969] show that Al_2O_3 (corundum) seems to show even less evidence for excitonic thermal transport than believed earlier [Jamieson and Lawson, 1958]. In view of the insufficient evidence for this mechanism in any of the materials of interest here, we consider it no further. A similar conclusion is reached by Clark [1969]. Thus, no energy gap particles are likely to be important in the earth's mantle as carriers of heat. Only the two continuum mechanisms, lattice vibrations and radiation, remain important. Thus the total thermal conductivity is the sum of K_L

and K_R only, and K , in equation (1.4), can be replaced by K_L .

Before continuing with more detailed discussions of lattice and radiative thermal conductivity, it may be useful to indicate their most important differences in light of the kinetic formula. First, the length of the mean free paths for the two mechanisms is vastly different in earth materials: angstroms for phonons and millimeters or more for photons. It follows that violation of the assumption of large sample size compared to mean free path is, when reducing laboratory data, most likely to occur for radiation. Second, the speed of radiation (light) is clearly much greater than the speed of phonons (approximately the speed of sound). The specific heat of the photon gas must therefore be much less than that of the phonon gas, or else radiative heat transport would always dominate. Indeed this is the case. Only at an impossibly high temperature could a solid absorb more energy in the form of internal equilibrium radiation than in lattice vibrations. In fact, the photon specific heat is small enough that, although radiative heat transport can be theoretically important at any temperature, it is in actuality a high temperature phenomenon.

2. LATTICE THERMAL CONDUCTIVITY

Under standard conditions of temperature and pressure, lattice thermal conductivity may be correlated rather well with crystal structure [Spitzer, 1970]. The most important generalization is that increasing structural complexity leads to lower conductivity. Horai [1971] and Horai and Simmons [1969] present considerable data which support this and other related generalizations for rock-forming minerals. However, a more quantitative description is required to estimate temperature and pressure effects. To this end, equation (1.5) may be used to obtain an expression for the lattice thermal conductivity. Ziman [1960] reviews the derivation of an expression for K_L . Only a brief outline is given here in order to indicate the method.

The specific heat of the lattice is assumed to have its classical value for materials at or above the Debye temperature;

$$C_v = 3Nk \quad (2.1)$$

where N is the number of atoms per unit volume. The characteristic particle speed of phonons is the speed of sound, because the phonons which contribute most to the thermal transport are those which are at the lower end of the acoustic branches of the phonon spectrum. The

velocity V is thus given by

$$\frac{3}{V^3} = \frac{1}{V_p^3} + \frac{2}{V_s^3} \quad (2.2)$$

where V_p and V_s are, respectively, the longitudinal and transverse sound velocities. The last parameter required in the kinetic formula, the phonon mean free path, L , needs more discussion. But first, a simple procedure indicates the values expected for L . If equations (2.1) and (2.2) for C_v and V are substituted in equation (1.5), then the expected mean free path can be evaluated from the expression obtained, $L = 3K_v/C_v V$, by using thermal conductivity and velocity data. For earth materials Horai [1971], finds a variation of L from one to several tens of lattice spacings. A correct theoretical expression must give results of this magnitude.

Phonon Mean Free Path

Two mechanisms of phonon scattering are important in large grained crystals. They are collisions with (1) other phonons and (2) imperfections. Each of these may be associated with a mean free path such that

$$\frac{1}{L} = \frac{1}{L_1} + \frac{1}{L_2} \quad (2.3)$$

The smallest of L_1 or L_2 will thus dominate.

L_1 , the mean free path due to phonon-phonon interactions, is probably best described by the Umklapp three-phonon scattering process, which gives the result,

$$L_1 = \frac{\rho v^2 a}{Nk\gamma^2 T} \quad (2.4)$$

where ρ is the density, a the lattice constant and γ the Gruneisen constant. Now, suppose for the moment that L_1 is much smaller than L_2 . Then by equation (2.3), $L=L_1$ and the lattice thermal conductivity can be found by substitution in equation (1.5):

$$K_L = \frac{\rho v^2 a}{\gamma^2 T} \quad (2.5)$$

Alternate forms of equation (2.5) may be found by substitution of several equalities or approximations, involving for example, the Debye temperature, the volume coefficient of expansion, or the melting temperature from the Lindemann formula.

The possible dominance of a four-phonon scattering process, considered by Pomeranchuk [1941], leads to a $T^{-5/4}$ instead of T^{-1} dependence, but the resulting difference in conductivity is not really significant with respect to the uncertainties in experimental data. Under one condition, however, the Umklapp three-phonon

model for L_1 almost certainly breaks down: That is, if L_1 as calculated from equation (2.4) is smaller than the lattice spacing, a . This would occur at very high temperatures, where equation (2.4) allows L_1 to decrease without bound. However, this cannot be, for a discrete elastic model should not allow scattering to occur more often than once per atom. It thus seems reasonable to place an absolute lower limit of L_1 of

$$L_{1\min} = \bar{a}$$

where \bar{a} is the mean interatomic spacing. The resulting expression for the minimum K_L is

$$K_{L\min} = NkV\bar{a} = kV\left(\frac{\rho}{M}\right)^{\frac{2}{3}} \quad (2.6)$$

where \bar{M} is the mean atomic weight. The validity of the concept of a lower limit on lattice conductivity is supported by the general observations of Spitzer [1970]. In a glassy material, where general disorder always limits the free path, equation (2.6) should apply even at room temperature.

Joffe [1959] proposes a mechanism of conductivity by quantum hops of energy from one atom to another. In this case K_L has no minimum since the hopping frequency can be as small as one might desire. This model, however, is without experimental support.

The mean free path associated with imperfection scattering, L_2 , should be relatively independent of temperature at high temperatures. For scattering by substitutional impurities,

$$L_2 = \frac{a}{S(N_i/N)} \quad (2.7)$$

where S is the dimensionless scattering cross section (equal to the actual cross section expressed in units of lattice spacing) and N_i/N is the relative concentration of impurities [Joffe, 1956, 1960]. Because S is about unity, L_2 is about equal to the spacing between impurities, or probably several times the lattice constant.

If both L_1 and L_2 are included, then the general lattice conductivity expression becomes

$$K_L = NkVa \left[\frac{Nk\gamma^2 T}{eV^2} + S(N_i/N) \right]^{-1} \quad (2.8)$$

Effect of Temperature and Pressure

Equation (2.8) contains many implicit approximations and seldom gives numerically accurate values. A more reliable approach for the purpose of extrapolation is to assume that the functional dependence is correct, to write the expression in terms of arbitrary constants, and to fit a curve to experimental data by adjusting the

constants.

If we assume, first, only variation with temperature, then equation (2.8) can be rewritten as

$$K_L = \frac{1}{A + BT} \quad (2.9)$$

where A and B are constants. In a like manner, the minimum K_L becomes

$$K_{Lmin} = \text{constant} \quad (2.10)$$

It should be possible to fit a curve of the form of equation (2.9) to any data in a range of temperature where only lattice conductivity is important. In Figure 2.1, such a curve has been fitted to the data of Birch and Clark [1940] for dunite (of olivine composition $\text{Fo}_{92}\text{Fa}_8$). By observing equation (2.9), the prediction can be made that forsterite of composition Mg_2SiO_4 should theoretically have a higher lattice conductivity, corresponding to $A=0$ (if the iron acts as a substitutional scattering center). This prediction is confirmed by the experimental data of this investigation, shown also in Figure 2.1. Note that the theoretical lower limit should be reached at about 1200 °K. Clark [1969] calculates the values of the constants A and B for several other materials of geophysical interest. However, he uses data at temperatures

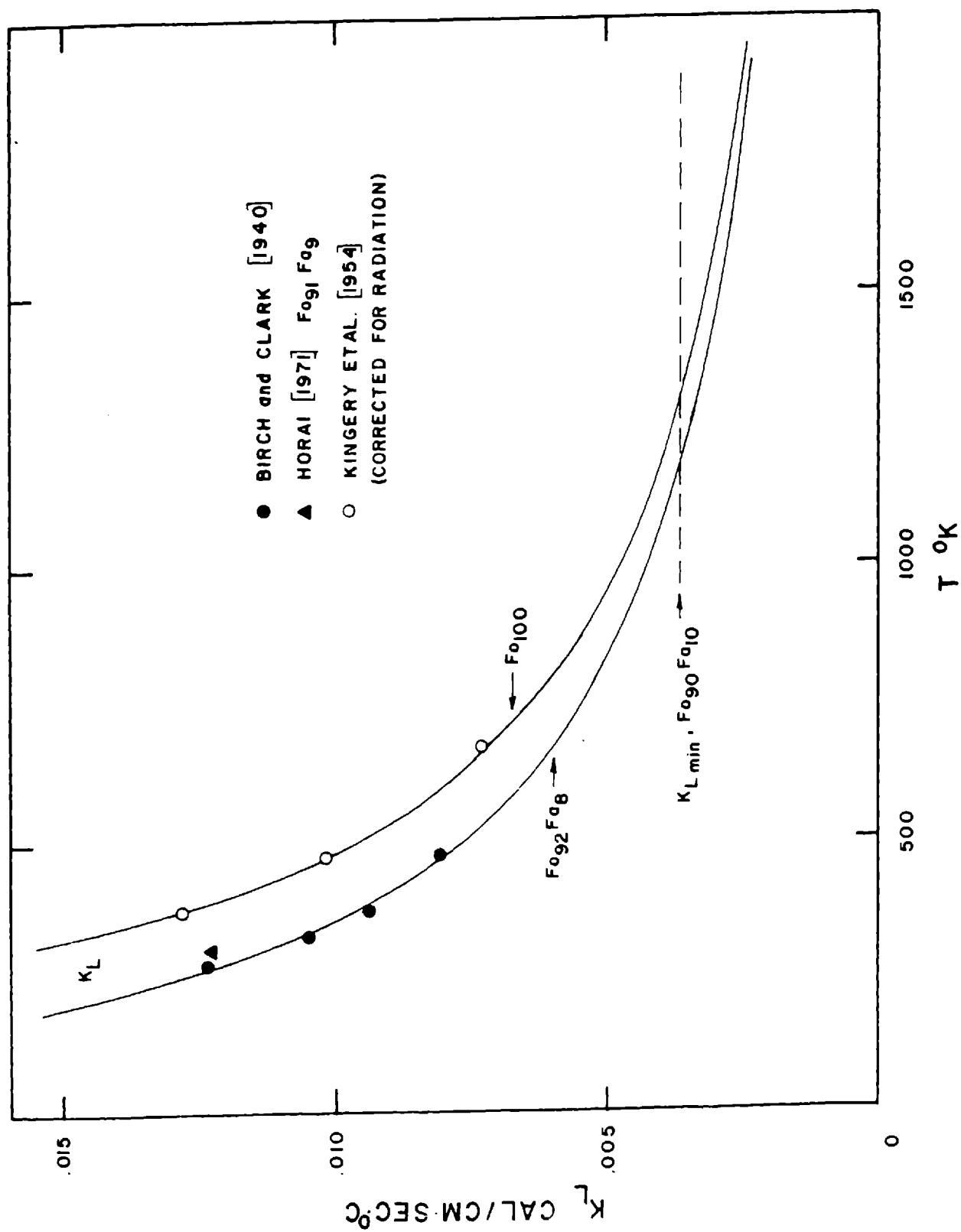
Figure 2.1 Lattice thermal conductivity of olivine as a function of temperature.

The curve fitted to the data of Birch and Clark [1940] is $K_L = 1/(26 + .21T)$.

The curve for forsterite, $For = Mg_2SiO_4$, is $K_L = 1/.21T$, and the data points are the values measured by Kingery et al.

[1954] minus the radiative conductivity measured in this investigation. (See Figure 6.4.) The lower limit,

$K_{Lmin} = .0037$, is calculated from equation (2.6) for $For_{90}Fa_{10}$ with $\bar{M} = 21$, $\rho = 3.33 \text{ g/cm}^3$, and $V = 5.35 \text{ km/sec}$.



where radiation is often important, and his values of A and B may not be the true values for lattice conductivity.

If we consider both temperature and pressure variations, then the expressions for lattice conductivity are

$$K_L = K_{L_0} \left(\frac{V}{V_0} \right)^3 \left(\frac{\rho_0}{\rho} \right)^2 \left(\frac{\rho}{\rho_0} \right)^{\frac{2}{3}} \left(\frac{A + BT_0}{A + BT} \right) \quad (2.11)$$

and

$$K_{L_{min}} = K_{L_{min_0}} \left(\frac{V}{V_0} \right) \left(\frac{\rho}{\rho_0} \right)^{\frac{2}{3}} \quad (2.12)$$

where the zero subscripts denote initial values. Fujisawa et al. [1968] verify the kinetic formula approach for predicting both pressure and temperature variations of lattice thermal conductivity by measuring the conductivities of forsterite and sodium chloride up to 1100 °K and 50 kb. Hughes and Sawin [1967] measure the conductivity of dunite to 500 °K and 18 kb but the scatter in their data make uncertain a further verification of the kinetic formula.

Lattice Conductivity in the Mantle

Zharkov [1958] and Lubimova [1967] calculate values of K_L for the earth's interior using expressions similar to (2.11). (Lubimova uses a $T^{-5/4}$ expression.) MacDonald [1959] simply assumes that K_L is constant in the mantle, which is surprisingly adequate because of the tendency for the effects of pressure and temperature to cancel each other.

We can eliminate the Gruneisen constant from equation (2.11) by using an estimate of the volume-dependence of γ for earth materials discussed by Wang [1970]. The estimate may be written as $(\frac{\gamma_0}{\gamma}) = (\frac{\rho}{\rho_0})^n$ where n has a value between one and two. If $n = 7/3$ is chosen, equation (2.11) becomes

$$K_L = K_{L0} \left(\frac{V_0 \rho}{V \rho_0} \right)^3 \left(\frac{A + B T_0}{A + B T} \right) \quad (2.13)$$

An illustration of possible results for K_L in the mantle is given in Figure 2.2. In computing these results, we use the parameter values given in Table 2.1. The use of these particular values is meant only as an example to demonstrate results for K_L . The significant features appear to be the dominance of the $1/T$ dependence throughout the upper 80 km or so, and the subsequent dominance of the pressure-dependence in the remaining depths. Note that K_{Lmin} may be attained throughout much of the upper mantle. We suggest that a sufficient approximation to K_L in the mantle is to set $K_L = K_{Lmin}$ except immediately below the crust, where only the temperature-dependence need be considered.

Although the discussion above should apply to both phases involved in a polymorphic phase transition

Figure 2.2 Example of a calculation of lattice thermal conductivity as a function of depth in the mantle. The equations for the curves are

$$\text{olivine} \quad K_L = .011 \left(\frac{V_p}{V_o p_o} \right)^3 \left(\frac{95}{32 + .21T} \right)$$

$$\text{spinel} \quad K_L = .018 \left(\frac{V_p}{V_o p_o} \right)^3 \left(\frac{95}{32 + .21T} \right)$$

$$\text{both} \quad K_{Lmin} = .00031 V_p^{\frac{2}{3}}$$

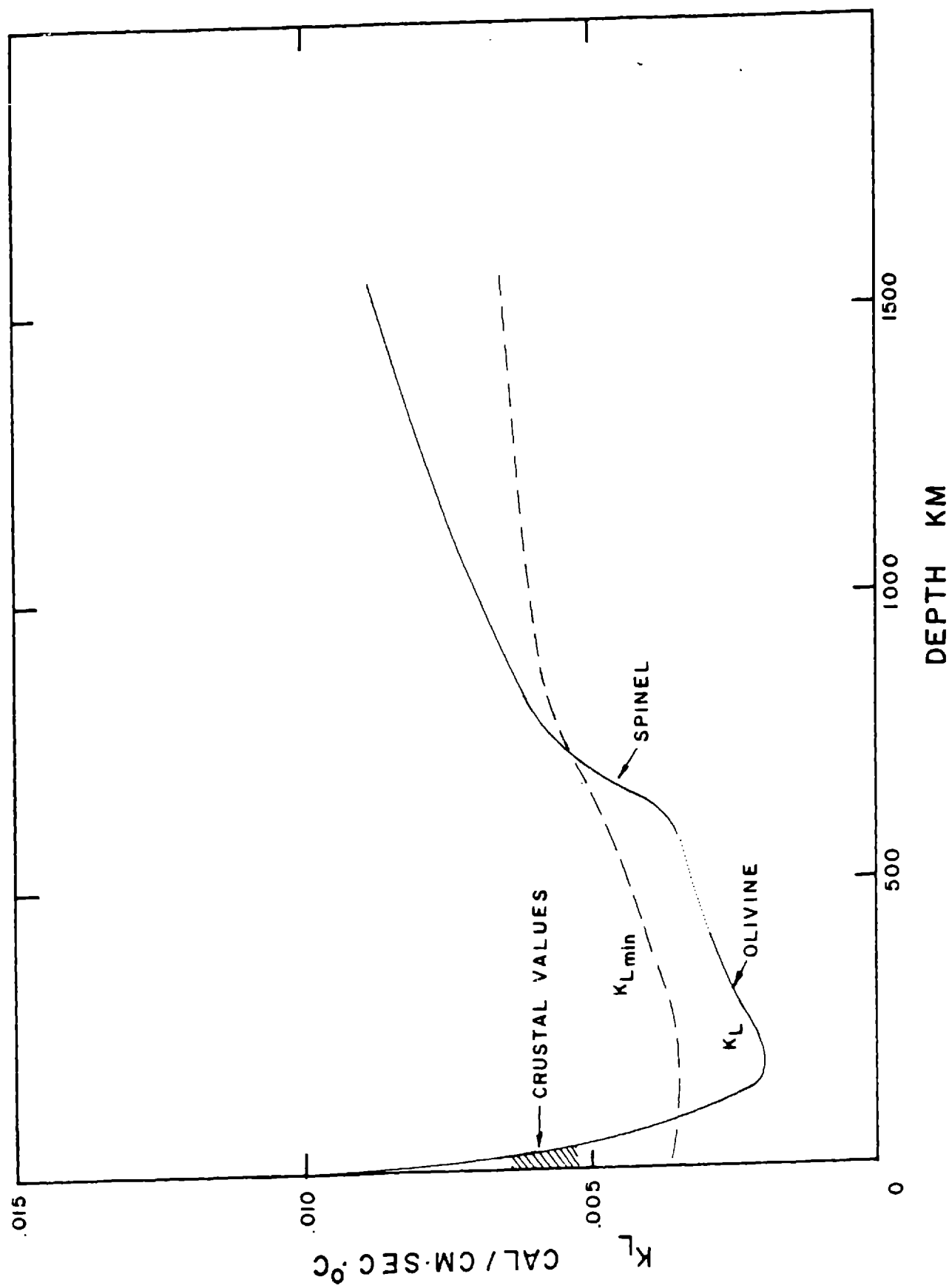


Table 2.1 Parameters used in calculation of lattice thermal conductivity in the mantle.

| Depth km | Temperature ^a °K | Density g/cm ³ | Mean velocity km/sec |
|----------|-----------------------------|---------------------------|----------------------|
| 0 | 300 | 3.33 | 5.35 |
| 60 | 1070 | 3.4 | 5.2 |
| 100 | 1400 | 3.5 | 5.0 |
| 200 | 1980 | 3.5 | 4.8 |
| 400 | 2600 | 3.75 | 5.6 |
| 600 | 2980 | 4.0 | 6.1 |
| 800 | 3260 | 4.4 | 6.9 |
| 1000 | 3460 | 4.6 | 7.1 |
| 1500 | 3800 | 4.8 | 7.5 |

| | v_o^b | ρ_o^b | K_{Lo} cal/cm sec °C |
|---------|---------|------------|------------------------|
| Olivine | 5.35 | 3.33 | .011 |
| Spinel | 6.01 | 3.68 | .018 ^c |

^aMacDonald [1959], Model 19.

^bChung[1971], olivine composition $Fe_{90}Fa_{10}$.

^cestimated from data of Fujisawa et al. [1968].

(if the new values of the zero subscripted constants are known) an interesting effect might arise in the midst of such a transition. Zhuze, et al. [1969] show evidence for the existence of a strong minimum in thermal conductivity in the vicinity of a phase transition, which they attribute to the greatly disturbed short-range order of the lattice. However, this effect is likely to be small in the earth if the lower limit on K_L has already been approached for both phases.

3. RADIATIVE THERMAL CONDUCTIVITY

The kinetic formula, equation (1.5), may be applied to the case of photons as follows:

$$C_v = \frac{16 \sigma T^3}{c} n^3 \quad (3.1)$$

$$v = \frac{c}{n}$$

$$L = \frac{1}{\epsilon}$$

where c is the speed of light in a vacuum, n is the refractive index of the medium and σ is the Stefan-Boltzmann constant. (See Fukao [1969] for a more explicit discussion of the application of the kinetic formula to radiative transfer.) The extinction coefficient ϵ , sometimes called the opacity, is defined as the sum of an absorption coefficient, α , and scattering coefficient, s , such that the attenuation of I , the intensity of radiation in the medium, is given by

$$I = I_0 e^{-\epsilon x} \quad (3.2)$$

Substitution of equation (3.1) in equation (1.5) gives

$$K_R = \frac{16}{3} \frac{\sigma n^2 T^3}{\epsilon} \quad (3.3)$$

Radiation Heat Flux in a Solid

Unfortunately, when equation (3.3) is derived in this manner, no indications of its limits of applicability are obvious other than the fact that L must be smaller than the medium dimensions. A useful alternate approach is to find the exact form of the radiative heat flux Q_R , which appears in equation (1.2) as a part of the total heat flux, and then to examine the conditions under which a "radiative conductivity" of the form (3.3) may be used such that $Q_R = -K_R \nabla T$.

Clark [1957] first used this approach in the earth sciences. Additional references to the early literature are given by Lee and Kingery [1960]. Sparrow and Cess [1966] derive a rather general expression for Q_R in their radiation heat transfer text. We will follow their derivation below.

Consider a radiation emitting, absorbing, and scattering region of thickness D bounded by two parallel planes. Assume local radiation balance. The extinction coefficient is defined as before, except that it (and all other properties) are wavelength-dependent. (All wavelength-dependent quantities are

called "spectral", such as the "spectral absorption coefficient.") For simplicity, only one dimensional flux (in the x-direction) is considered. Define an "optical coordinate" τ_λ such that $\tau_\lambda = \epsilon_\lambda x$ and $\tau_{0\lambda} = \epsilon_\lambda D$. Let $I_\lambda(x, \theta)$ be the local intensity of radiation as a function of wavelength, position, and angle, as shown in Figure 3.1. The wavelength dependent radiation heat flux is then given by

$$Q_{R\lambda}(\tau_\lambda) = \int_{4\pi} I_\lambda(\tau_\lambda, \theta) \cos \theta \, d\omega \quad (3.4)$$

where the integration is over the entire solid angle.

Two differential equations are now formulated: one describing the augmentation or attenuation of I_λ in the positive direction as a result of absorption, scattering, and emission within a volume element; and the other describing the same effects in the negative direction. Scattering is assumed to be coherent (no wavelength change) and isotropic (equal probability of scattering direction). The two differential equations are solved and substituted in equation (3.4) to give

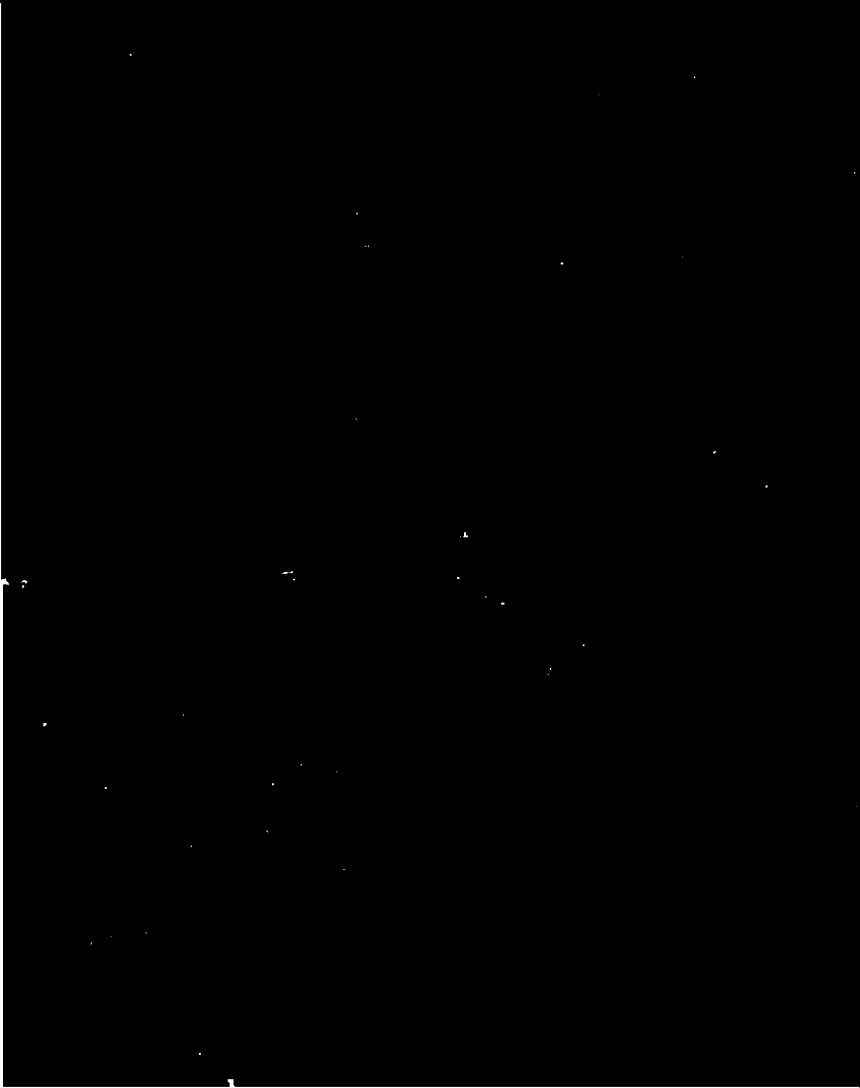
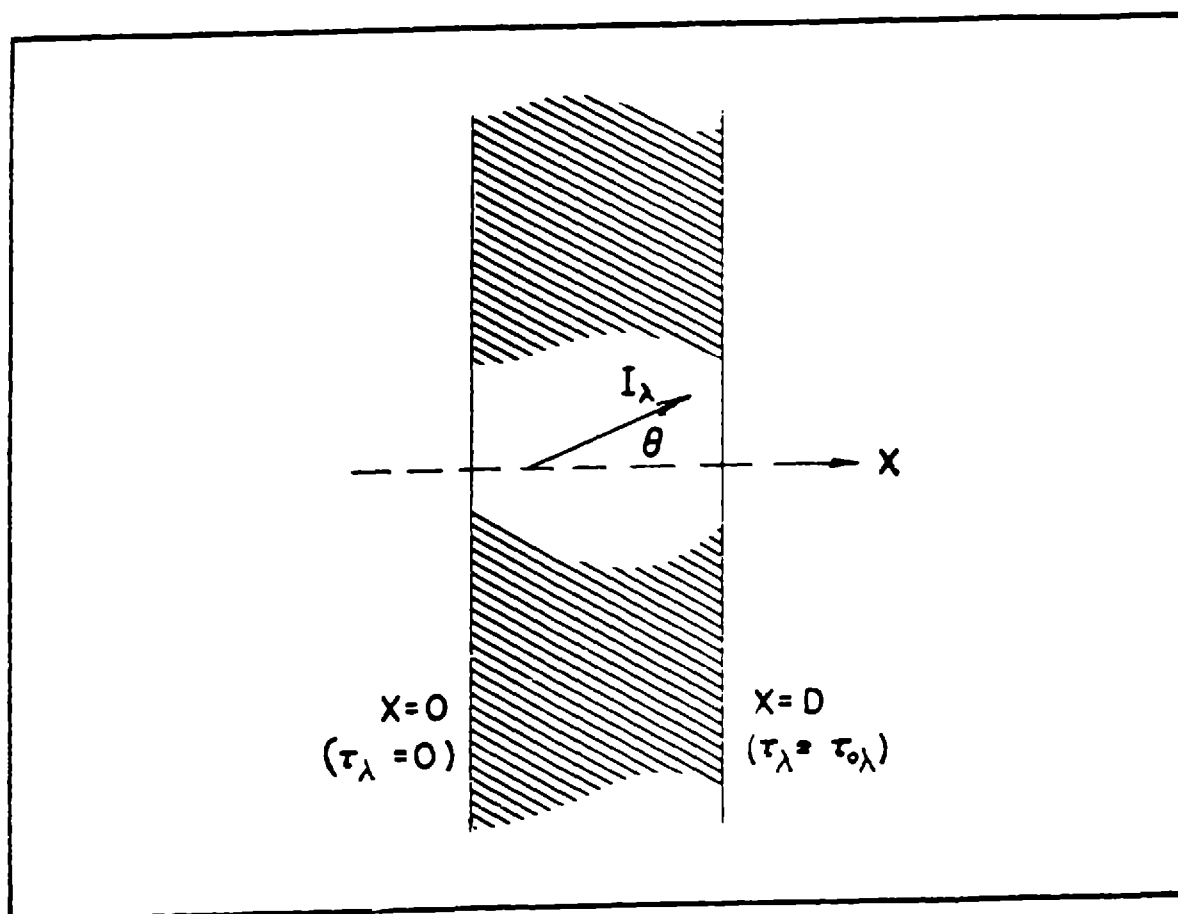


Figure 3.1 Geo
lation of rad



$$\begin{aligned}
Q_{\lambda}(\tau_{\lambda}) = & 2 \int_0^{\tau_{\lambda}} \left[\frac{\alpha_{\lambda}}{\epsilon_{\lambda}} e_{b\lambda}(x') + \frac{S_{\lambda}}{4\epsilon_{\lambda}} G_{\lambda}(x') \right] E_2(\tau_{\lambda}-x') dx' \\
& - 2 \int_{\tau_{\lambda}}^{\tau_{0\lambda}} \left[\frac{\alpha_{\lambda}}{\epsilon_{\lambda}} e_{b\lambda}(x') + \frac{S_{\lambda}}{4\epsilon_{\lambda}} G_{\lambda}(x') \right] E_2(x'-\tau_{\lambda}) dx' \\
& + 2 B_{0\lambda} E_3(\tau_{\lambda}) - 2 B_{D\lambda} E_3(\tau_{0\lambda}-\tau_{\lambda})
\end{aligned}
\tag{3.5}$$

where $e_{b\lambda}$ is the spectral black-body emissive power in the medium and x' is a dummy variable. G_{λ} is the total incident energy per unit area within the medium given by

$$G_{\lambda}(\tau_{\lambda}) = 2\pi \int_0^{\pi} I_{\lambda}(\tau_{\lambda}, \theta) \sin \theta d\theta$$

and the E_n 's are the (well tabulated) exponential integral functions. $B_{0\lambda}$ and $B_{D\lambda}$ are the diffuse spectral "radiosities" of the surfaces 0 and D. (The assumption of diffuse surfaces is used for simplicity of expression in equation (3.5) only; it is not necessary.)

Only one of the assumptions underlying equation (3.5) is inaccurate, namely, that of isotropic scattering. The general case for the aggregate materials of interest in the earth sciences is not isotropic scattering. (See Pitt and Tozer [1970b] .) The consequences of this fact will be discussed in a later section. It is worth mentioning here that no severe

problems arise. Otherwise, equation (3.5) is quite generally valid, even if convection is included in the heat flow equation, provided that the flow velocities are much less than the speed of light (!).

The total Q_R is found by integrating Q_R over all wavelengths,

$$Q_R(\tau) = \int_0^{\infty} Q_{R\lambda}(\tau_\lambda) d\lambda \quad (3.6)$$

If Q_R is then substituted in the heat flow equation, a non-linear integro-differential equation results which is extremely difficult to solve, even approximately, except in certain special cases.

One of these special cases is that of an optically thick medium--that is, when D is large compared to the length $1/\epsilon_\lambda$. (Departures from thermal equilibrium also have to be small and smooth such that they are expandable in a Taylor's series.) Equation (3.5) may then be simplified as follows: First, assume far removal from the boundaries such that the surface radiosity terms may be dropped; then, define

$$F_\lambda(\tau_\lambda) = \frac{\alpha_\lambda}{\epsilon_\lambda} e_{b\lambda}(\tau_\lambda) + \frac{S_\lambda}{4\epsilon_\lambda} G_\lambda(\tau_\lambda)$$

and expand F_λ in a Taylor's series about $x' = \tau_\lambda$,

which gives

$$F_{\lambda}(x') = F_{\lambda}(\tau_{\lambda}) + \frac{dF_{\lambda}}{d\tau_{\lambda}} (x' - \tau_{\lambda}) + \frac{1}{2} \frac{d^2 F_{\lambda}}{d\tau_{\lambda}^2} (x' - \tau_{\lambda})^2 + \dots$$

Substitute this into equation (3.5), to yield

$$\begin{aligned} Q_{R_{\lambda}}(\tau_{\lambda}) = & 2 F_{\lambda}(\tau_{\lambda}) \left[\int_0^{\tau_{\lambda}} E_2(z) dz - \int_0^{\tau_{0\lambda} - \tau_{\lambda}} E_2(z') dz' \right] \\ & - 2 \frac{dF_{\lambda}(\tau_{\lambda})}{d\tau_{\lambda}} \left[\int_0^{\tau_{\lambda}} z E_2(z) dz + \int_0^{\tau_{0\lambda} - \tau_{\lambda}} z' E_2(z') dz' \right] \\ & + \dots \end{aligned}$$

where $z = \tau_{\lambda} - x'$ and $z' = x' - \tau_{\lambda}$.

Now, if we are far from the boundaries of the medium, the conditions $\tau_{\lambda} \rightarrow \infty$ and $\tau_{0\lambda} - \tau_{\lambda} \rightarrow \infty$ apply, and the expression for $Q_{R_{\lambda}}$ becomes

$$Q_{R_{\lambda}} = - 4 \frac{dF_{\lambda}}{d\tau_{\lambda}} \int_0^{\infty} z E_2(z) dz = - \frac{4}{3} \frac{dF_{\lambda}}{d\tau_{\lambda}} \quad (3.7)$$

A similar procedure for G_{λ} gives

$$G_{\lambda} = 4 e b_{\lambda}(\tau_{\lambda})$$

Putting G_λ and the definition of F_λ into equation (3.7) yields

$$\begin{aligned} Q_{R\lambda} &= -\frac{4}{3} \frac{de_{b\lambda}}{d\tau_\lambda} \\ &= -\frac{4}{3\epsilon_\lambda} \frac{de_{b\lambda}}{dx} \end{aligned} \quad (3.8)$$

This equation concludes the outline of Sparrow and Cess's presentation.

Now, let

$$\frac{de_{b\lambda}}{dx} = \frac{de_{b\lambda}}{dT} \frac{dT}{dx}$$

where only temperature is assumed to be a function of position in the medium. (This assumption need be true only over the length $1/\epsilon_\lambda$.) Integration of equation (3.8) over all wavelengths as illustrated by equation (3.6) gives the total radiation heat flux:

$$Q_R = -\frac{4}{3} \frac{dT}{dx} \int_0^\infty \frac{1}{\epsilon_\lambda} \frac{de_{b\lambda}}{dT} d\lambda \quad (3.9)$$

Expression of equation (3.9) in the form

$$Q_R = -K_R \frac{dT}{dx}$$

yields

$$K_R = \frac{4}{3} \int_0^\infty \frac{1}{\epsilon_\lambda} \frac{de_{b\lambda}}{dT} d\lambda \quad (3.10)$$

which is the desired result of a "radiative conductivity."

A further simplification puts equation (3.10) in the simple form of equation (3.3). The Rosseland mean extinction coefficient, $\bar{\epsilon}$, is defined by

$$\frac{1}{\bar{\epsilon}} = \frac{\int_0^{\infty} \frac{1}{\epsilon_{\lambda}} \frac{d\epsilon_{\lambda}}{dT} d\lambda}{\int_0^{\infty} \frac{d\epsilon_{\lambda}}{dT} d\lambda} \quad (3.11)$$

[Sparrow and Cess, 1966, p. 215]. Substitute equation (3.11) in (3.10) to give

$$K_R = \frac{4}{3\bar{\epsilon}} \frac{d}{dT} \int_0^{\infty} \epsilon_{\lambda} d\lambda$$

Furthermore, if the refractive index is only a weak function of wavelength (and temperature) near to the maximum of $\frac{d\epsilon}{dT}$, then

$$\frac{d}{dT} \int_0^{\infty} \epsilon_{\lambda} d\lambda = \frac{d}{dT} (n^2 \sigma T^4) = 4n^2 \sigma T^3$$

so that

$$K_R = \frac{16}{3} \frac{\sigma n^2 T^3}{\bar{\epsilon}} \quad (3.12)$$

which is identical to equation (3.3) with $\bar{\epsilon}$ replacing ϵ .

For an optically thick medium, the most important unknown quantity in radiative transfer is the mean

extinction coefficient, which is the spectral coefficient averaged and weighted with respect to the temperature derivative of the spectral black body emissive power. However, the temperature derivative of black body emission has a strong maximum very near to the maximum of the black body function itself, so, in essence, the most important contribution to the value of $\bar{\epsilon}$ probably results from those wavelengths near the peak of $e_{b\lambda}$ (unless the medium is extremely transparent elsewhere). This observation means that, even if ϵ_{λ} were not a function of temperature (which is not the case) $\bar{\epsilon}$ would still, in general, be a function of temperature. Figure 3.2 demonstrates this relation:

$e_{b\lambda}$ is plotted at several temperatures for comparison with the wavelength dependent absorption coefficient for olivine at room temperature. Note that as temperature increases, $e_{b\lambda}$ moves into the more transparent regions. Thus $\bar{\epsilon}$ would decrease. The most important wavelength interval for radiative transfer at mantle temperatures is 0.5 to 4 microns.

To indicate the values of the mean extinction coefficient that are important, K_R is plotted in Figure 3.3 for several hypothetical values of $\bar{\epsilon}$. The previous result for lattice conductivity in forsterite is shown for comparison. A value of $\bar{\epsilon}$ less than about 20 cm^{-1} (corresponding to a photon mean free path

Figure 3.2 Black body emission at various temperatures compared to typical absorption spectrum of olivine [White and Keester, 1966].

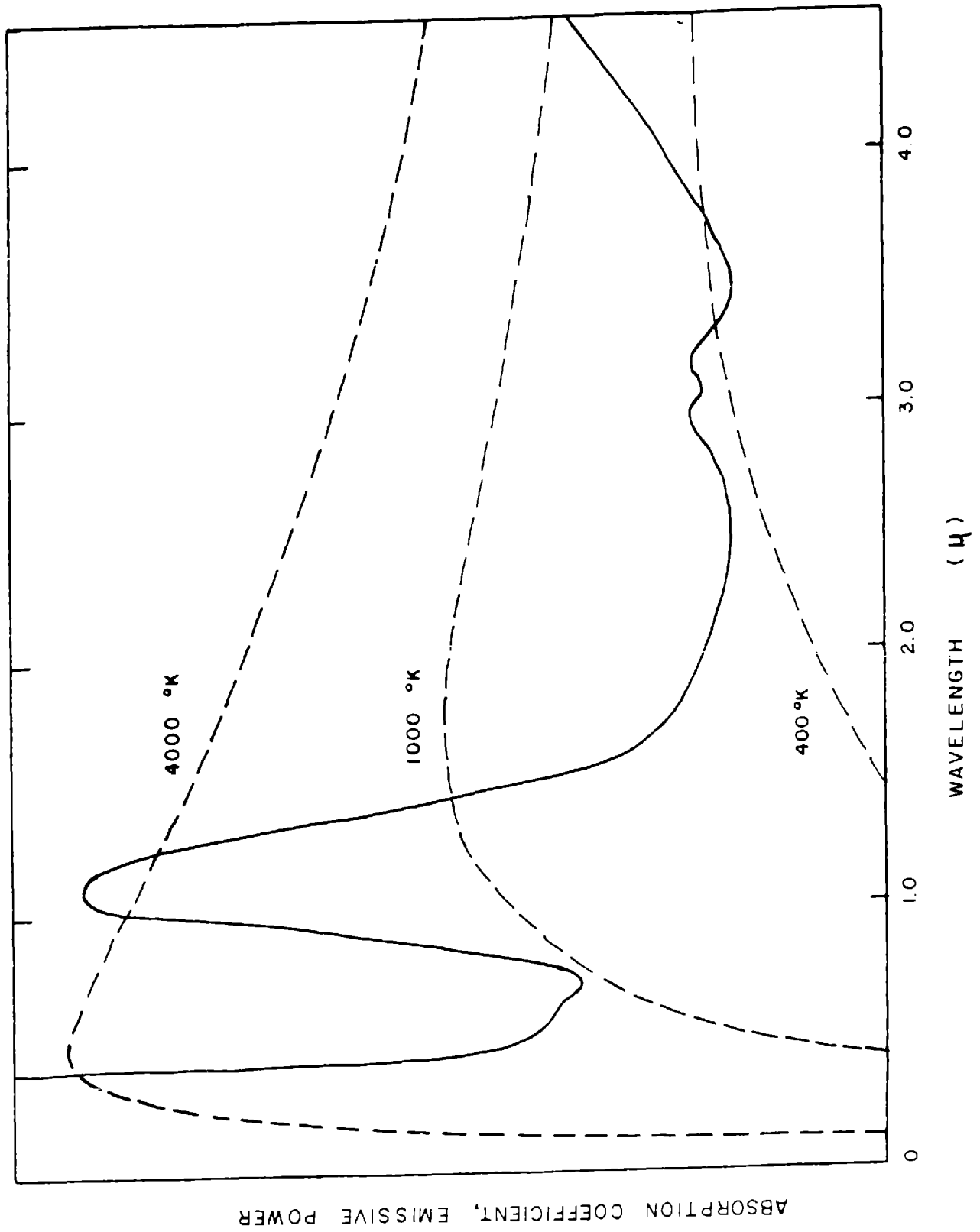
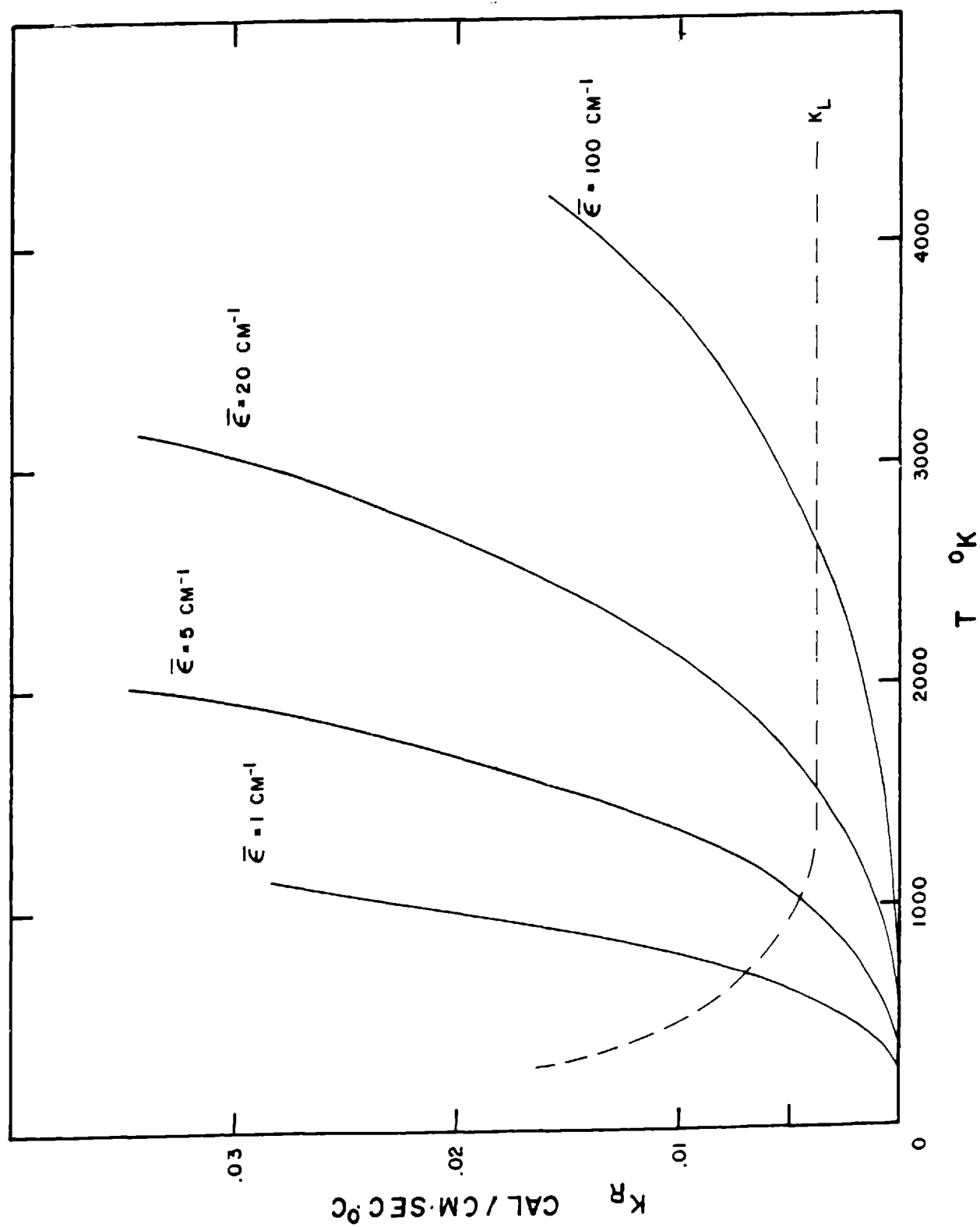


Figure 3.3 Radiative thermal conductivity
as a function of temperature for several
values of mean extinction coefficient.



greater than .05 cm) would cause K_R to dominate at temperatures above 1500 °K.

A somewhat detailed discussion of the contributions of scattering and absorption to the extinction coefficient is given below, but, due to the complicated nature of these phenomena in crystalline solids, we do not attempt to describe the general case. Instead, the discussion is limited to a brief description applied to the common silicates and oxides--either in their pure state or containing iron as an example of a transition metal impurity.

Scattering

Two general types of scattering media are of interest. The first is a rather large grained assemblage of particles of two or more slightly different refractive indices. The second is a material of very small, uniform grain size with a great many intergranular voids. The size of the voids may be comparable to the radiation wavelength. The major difference between the two is that in the first the laws of geometric optics apply to the scattering process, while in the second, they do not. Only in the second is the scattering strongly wavelength-dependent.

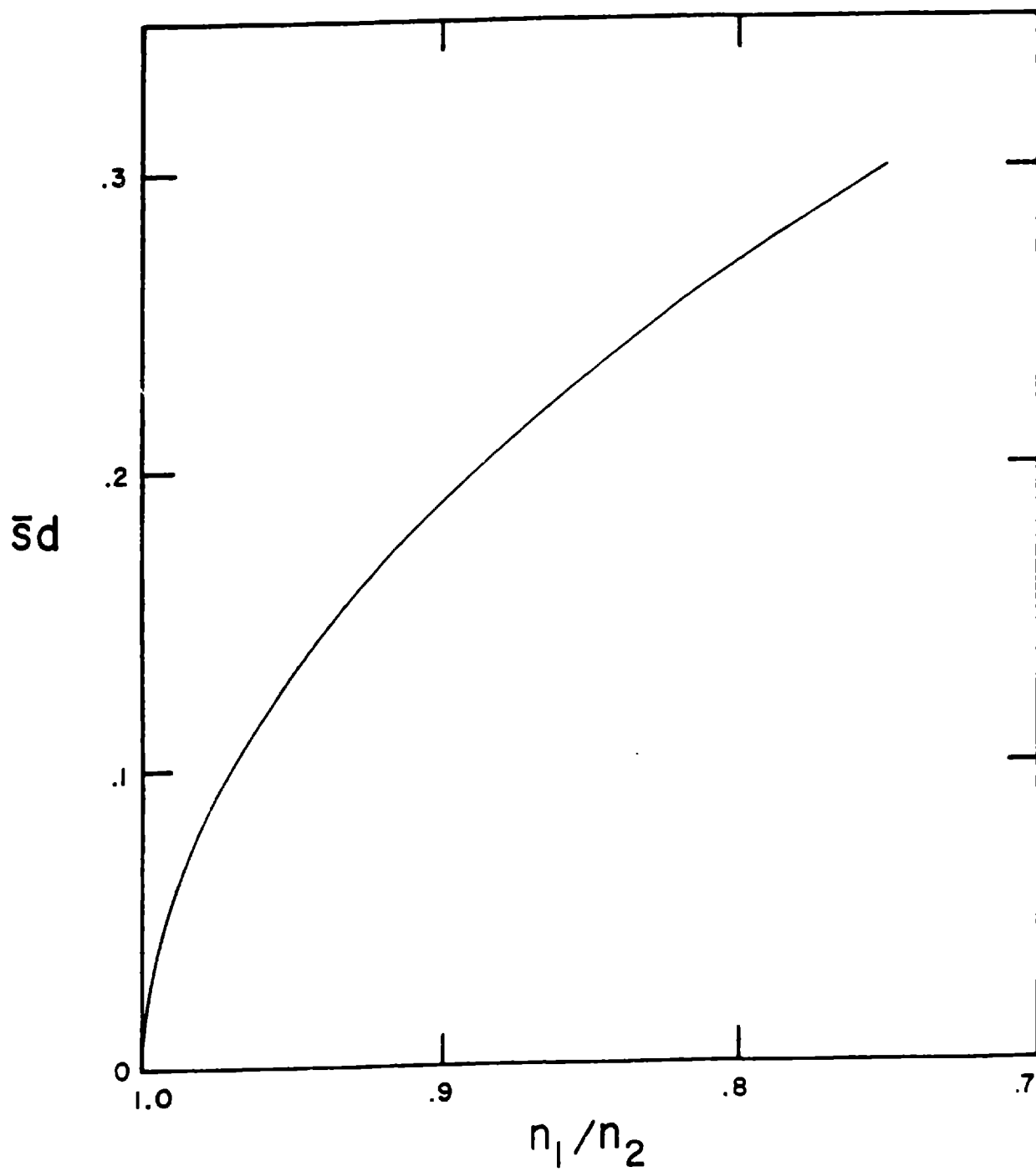
A large-grained (several millimeters) assemblage is possibly typical of the earth's interior. Aronson

et al. [1967 a,b] consider such assemblages without the (previously mentioned) restrictive assumption of isotropic scattering. They find, particularly for the larger grain sizes, that the form of the equation for the mean extinction coefficient is essentially unchanged from its isotropic form, provided that \bar{s} is considered to be the backscattering, and not total scattering, coefficient. They consider scattering caused at grain interfaces by the mechanisms of refraction and reflection for the case of two different refractive indices. If the difference between the indices is small ($1 \geq n_1/n_2 > \frac{1}{2}$) then the refraction term dominates. Furthermore, if the difference is very small ($1 \geq n_1/n_2 > \frac{3}{4}$), as is probably the case in earth materials, Aronson's result reduces to

$$\bar{s} = \frac{4}{3\pi d} \left[2 \left(1 - n_1/n_2 \right) \right]^{\frac{1}{2}} \quad (3.13)$$

where d is the average distance between interfaces. This function is plotted in Figure 3.4. For example, if $n_1/n_2 = 0.9$ and $d = 0.1$ cm, then $\bar{s} = 2$ cm⁻¹. This result indicates that, if the mean grain size in the mantle is 1 mm or larger, then 2 cm⁻¹ is a rough upper limit to the size of the scattering coefficient. In the next section, the absorption coefficient, $\bar{\alpha}$, will be shown to be generally larger than 2 cm⁻¹, which indicates

Figure 3.4 The quantity $\bar{S}d$ for scattering
in a large-grained particle assemblage
as a function of relative refractive
index of the grains [Aronson et al.,
1967a] .



that scattering is of secondary importance in the mantle.

Some laboratory samples are extremely small-grained materials, and the tiny pores, rather than the grain interfaces, act as scattering centers. The grains, in fact, are only a passive matrix in which the pores are located. Van de Hulst [1957] demonstrates the application of Mie scattering theory to the case of spherical, randomly distributed scattering centers. Lee and Kingery [1960] successfully apply this theory to several ceramic materials. The wavelength-dependent scattering coefficient is given by

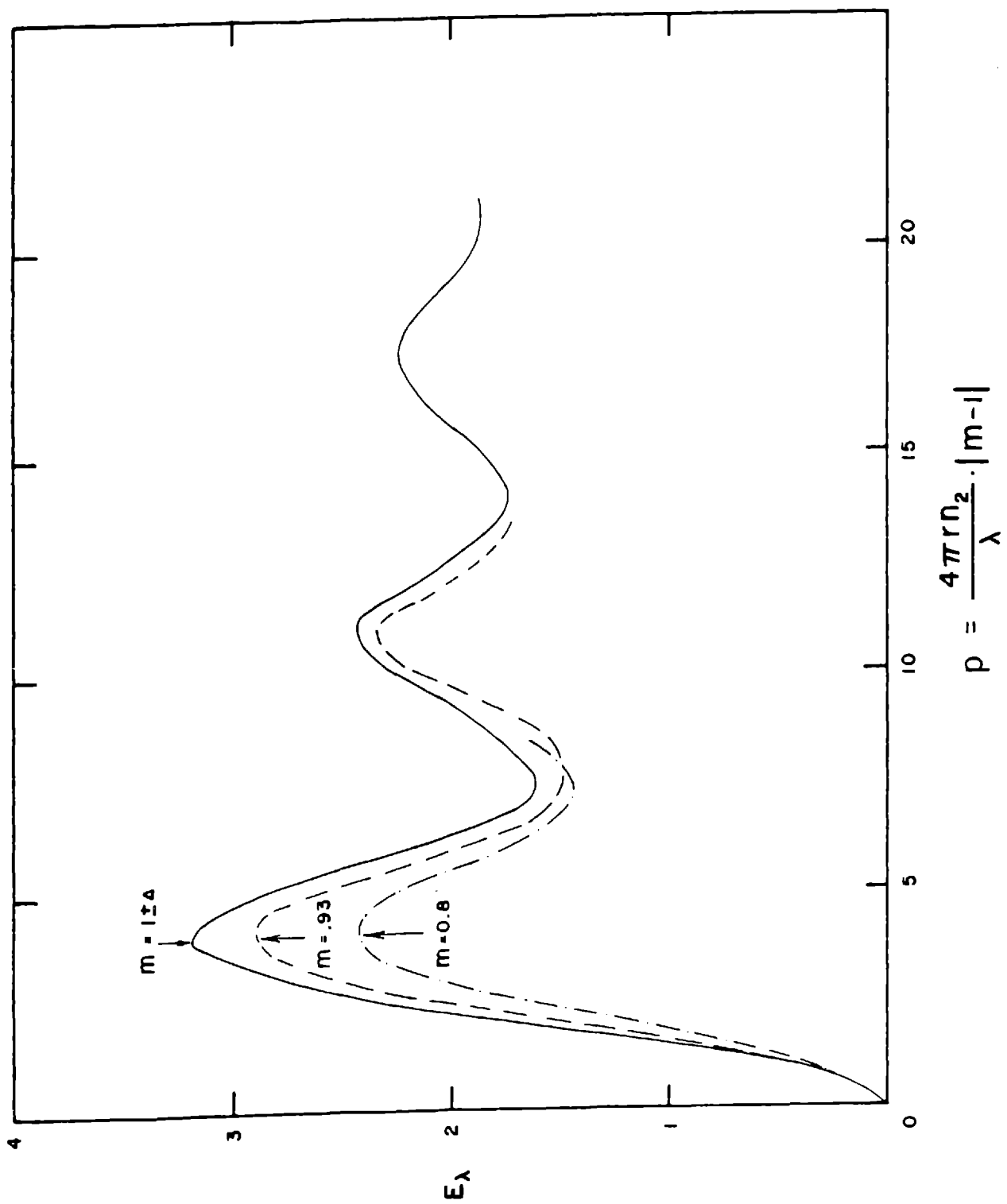
$$S_{\lambda} = \frac{3}{4} \frac{V_{por}}{r} E_{\lambda} \quad (3.14)$$

where V_{por} is the volume fraction porosity, r is the pore radius, and E_{λ} is the wavelength-dependent extinction efficiency. The extinction efficiency is most easily described as a function of p , where

$$p = \frac{4\pi r n_2}{\lambda} \left| \frac{n_1}{n_2} - 1 \right| \quad \text{where } n_1 \text{ and } n_2$$

are the refractive indices of pore and matrix. Extinction curves are shown in Figure 3.5 for several values of relative refractive index $m = n_1/n_2$. Note that if $p > 2$ then $E_{\lambda} \approx 2$. For example, if $n_1 = 1$ and $n_2 = 1.5$, then p is greater than 2 if $r/\lambda \gtrsim 1/3$, which is probably often (but not always) true for sintered ceramics. In

Figure 3.5 Extinction efficiency for a
porous small-grained particle assemblage
as a function of the parameter p
[Van de Hulst, 1957].



this case, the scattering is independent of wavelength and

$$\bar{S} = \frac{3}{2} \frac{V_{por}}{r} \quad (3.15)$$

For example, if $V_{por} = 0.01$ and $r = 3 \times 10^{-4}$ cm, then $\bar{S} = 50 \text{ cm}^{-1}$, a rather large value. This example shows that scattering can be the dominant extinction mechanism in a material containing a large number of pores.

Absorption

The physical nature of the absorption spectra of silicates has been reviewed in articles by Clark [1969], Shankland [1970], and Burns [1970]. Their general observations, outlined below, apply also to insulating oxides. The main features of the absorption spectra are the strong absorptions in the near infrared and visible-ultraviolet--separated by a relatively non-absorbing region from about 0.5 to 3 microns. (See Figure 3.2.) The non-absorbing region, or "pass band", may contain absorptions due to the presence of iron or other transition metal impurities. The strength of these pass band absorptions are critical to the limitation of radiation transfer.

The strong absorptions in the near infrared begin at about 3-5 microns and extend to longer wavelengths.

They are due to the vibrations of the lattice itself and are expected to increase in intensity and shift to shorter wavelengths as temperature and pressure increase. However, at all but the lowest temperatures, the majority of the radiant energy is at even shorter wavelengths. Changes in the lattice infrared absorptions are thus not critical to the value of the mean absorption coefficient.

The strong absorptions at the short wavelength end of the spectrum in the visible blue or ultraviolet begin at $\frac{1}{2}$ micron and continue to shorter wavelengths, corresponding to energies of about 3-8 ev. There are two types: The first (lowest energy) is due to charge transfer--the result of electron exchange between impurities such as iron and the neighboring crystal ions; and the second is due to processes more intrinsic to the lattice electronic structure, including exciton and band gap absorptions. The long wavelength edges of these absorptions are generally observed to move to longer wavelengths with increasing temperature and pressure, although Pitt and Tozer [1970a] observe the opposite pressure effect in some materials. At all but the very highest temperatures, most of the radiant energy is at longer wavelengths than these absorptions, so again, the effect on mean absorption coefficient is small, except perhaps in the deep mantle.

Pure end-member silicates and oxides are quite transparent in the range between these two groups of strong absorptions, having values of $\bar{\alpha}$ probably much less than 1 cm^{-1} . If such a high degree of purity existed in earth materials, the radiative conductivity would be very large indeed, exceeding the lattice conductivity by several orders of magnitude. Clearly, any impurity-caused absorptions in the pass band are of critical importance to the magnitude of radiative heat transfer.

The commonest absorptions in the pass band involve the d and f level electrons in transition metal impurities, and are best explained by crystal field theory. Ferrous iron (Fe^{2+}), is the most important of these impurities. It has absorption bands in the olivine lattice which center at about 1.1 micron, but are not very sharp. There are similar bands in most other silicate and oxide lattices. But, even accounting for the presence of these absorptions, the extrapolation of room temperature spectral data for olivine would still result in an $\bar{\alpha}$ of less than 1 cm^{-1} at high temperatures [Fukao et al. 1968]. Apparently, then, the temperature and pressure behavior of crystal field transitions controls the magnitude of radiative energy transfer in the earth.

Effect of Temperature and Pressure

The crystal field absorptions broaden and increase with temperature above 500 °K [Fukao et al. 1968; Aronson et al. 1968]. As a result, the mean absorption coefficient increases with temperature almost rapidly enough to offset the increase of radiative conductivity. The present investigation extends the observed increase of mean absorption coefficient to 1900 °K. Figures 3.6 and 3.7 illustrate the temperature-dependences of spectral absorption in olivine.

Although the absorption bands shift with pressure to shorter wavelengths, which causes a decrease in

$\bar{\epsilon}$, the pressure shift (about 0.1 μ extrapolated to 150 kb) is not as important in geophysical applications as the thermal broadening [Shankland, 1970]. Pitt and Tozer [1970b] calculate K_R in olivine from the data of Fukao et al. [1968] and include pressure corrections. Their results are shown in Figure 3.8. By comparison with the values of lattice conductivity given in Figures 2.1 and 2.2, it is apparent that K_R and K_L might be of comparable magnitude in the mantle.

The above discussion should apply, at least qualitatively, to the spinel side of the olivine-spinel phase transition though the iron crystal field

Figure 3.6 Absorption spectra of olivine
at high temperatures [Fukao et al., 1968].

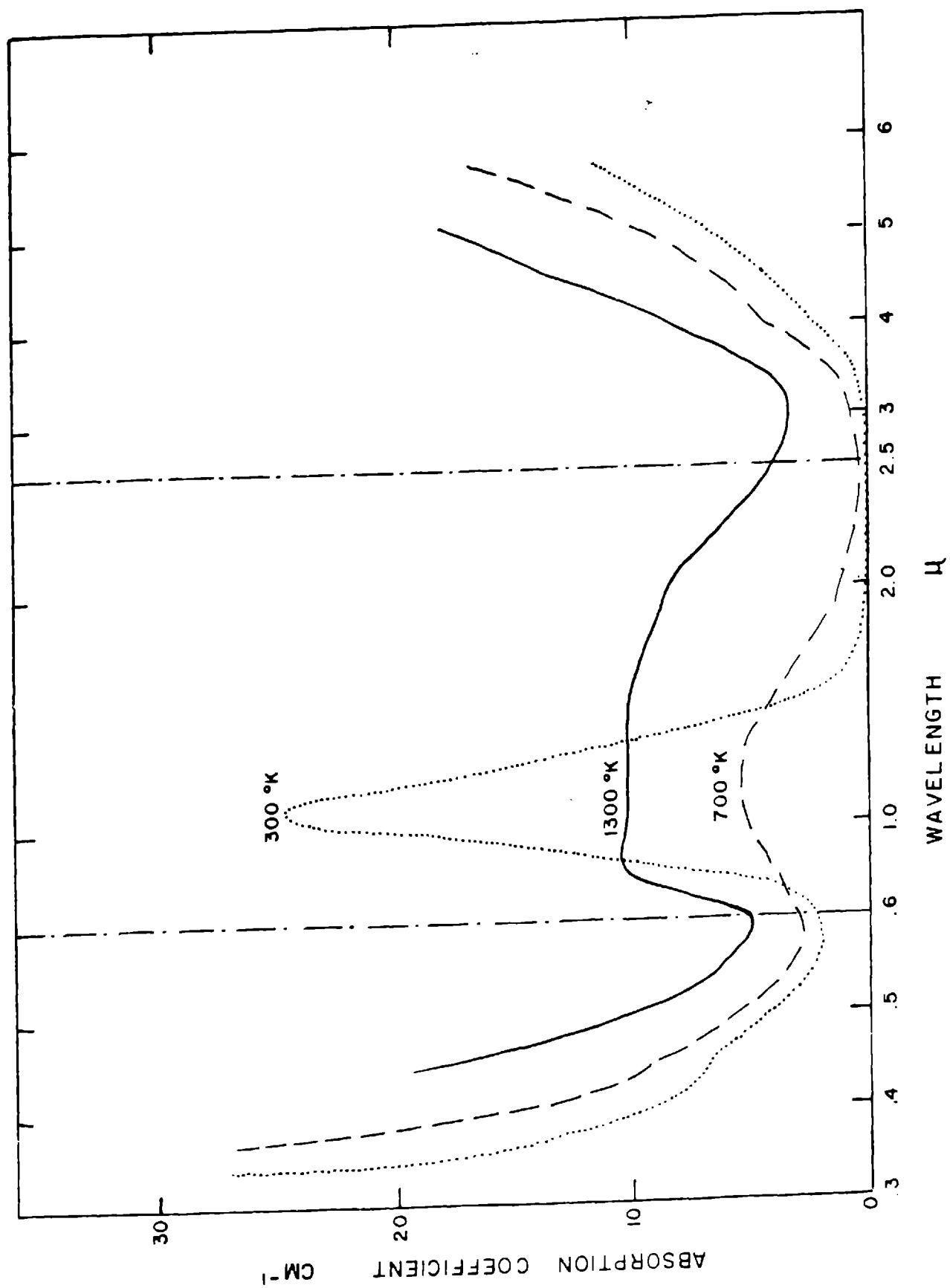


Figure 3.7 Mean extinction coefficient
in olivine as a function of temperature
[Fukao et al., 1968; Aronson et al.,
1968].

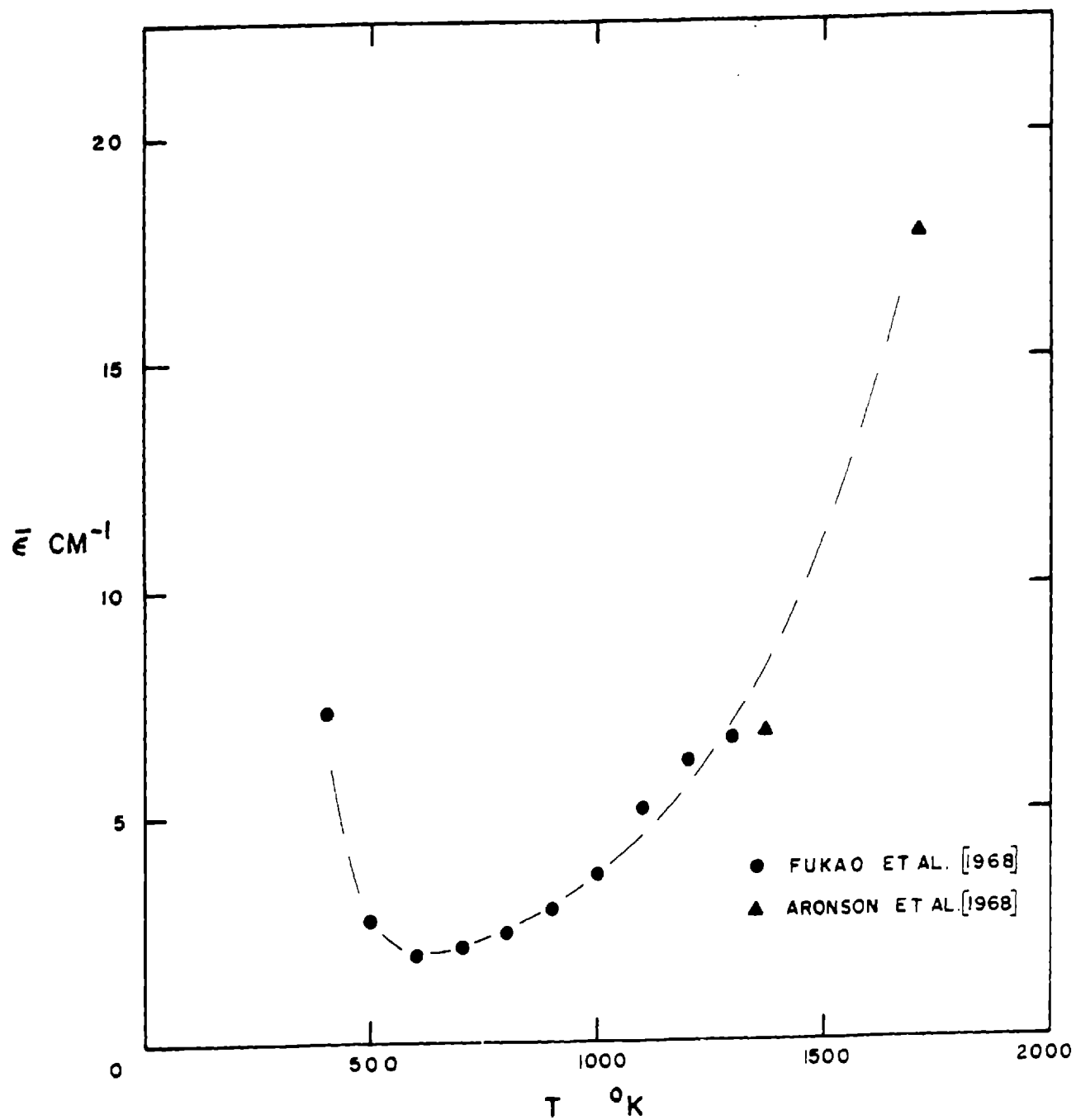
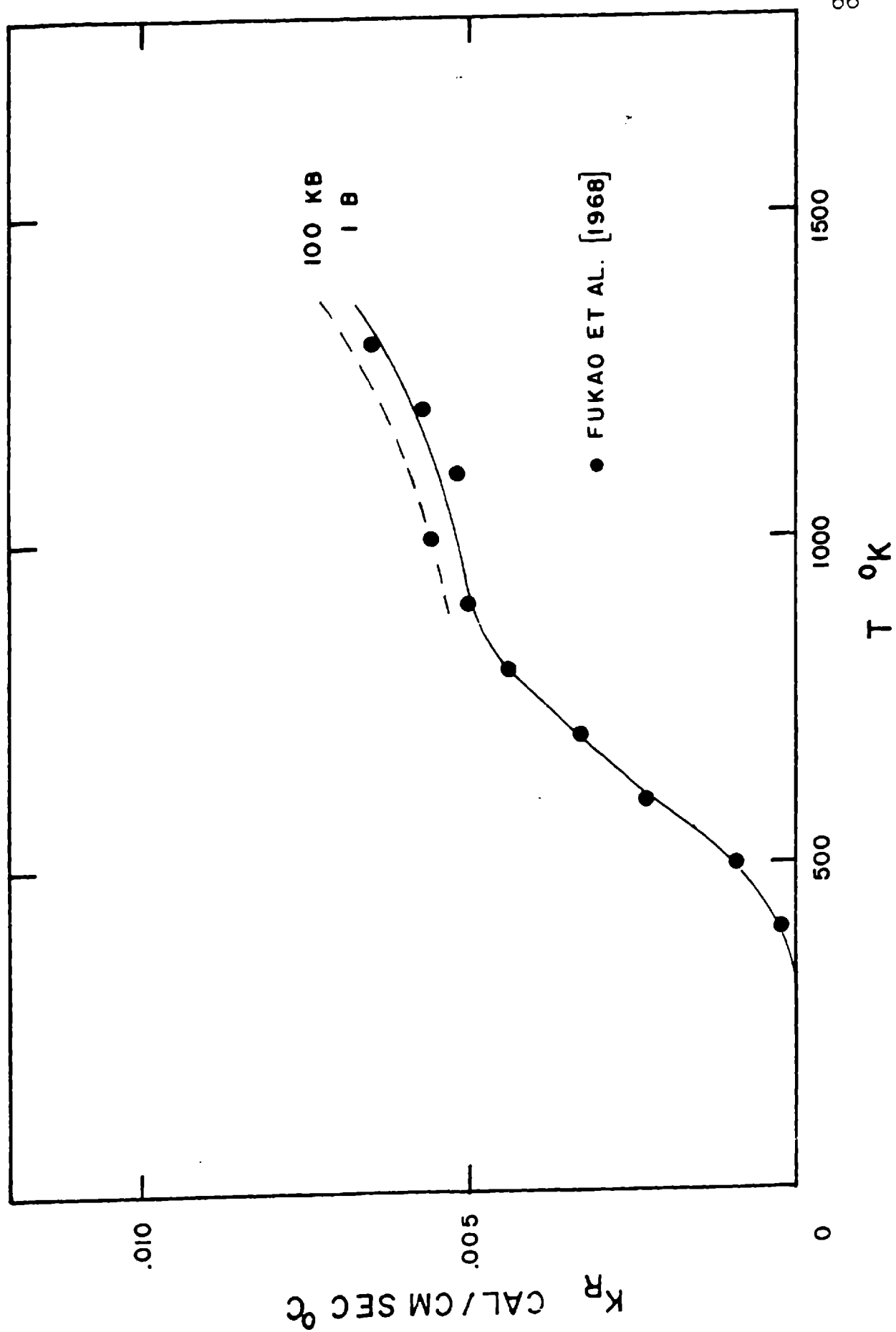


Figure 3.8 Radiative thermal conductivity
in olivine as a function of temperature
and pressure [Pitt and Tozer, 1970b].



absorptions might occur at longer wavelengths and block more of the radiation. Reed and Vay [1969] demonstrate the Fe^{2+} absorptions in the $\text{MgO} \cdot 3.5\text{Al}_2\text{O}_3$ spinel structure. The question arises, though, as to what happens to the material which is in the midst of a polymorphic transition. Burns [1970] argues that the absorption should increase strongly, due to the general increase in disorder within the crystal. On the other hand, the situation in which the iron has a tendency to accumulate in only one of the polymorphic structures is conceivable. Then the material would become a mix of relatively opaque and transparent grains, which might actually have a decreased absorption, and an increased radiative thermal conductivity.

4. EXPERIMENTAL METHOD

General Remarks

The discussion in the previous chapters indicates that the heat transfer within a small laboratory sample is governed by the interrelated effects of lattice conduction, radiation, and sample geometry. To fully understand these effects, it would be desirable to have a method of thermal conductivity measurement which clearly separates conduction and radiation, particularly at high temperatures where radiation is most likely important. The new method described here is in a general sense an extension of the Ångström method (see Carlslaw and Jaeger [1959]) to the case of internally radiating media, but with the purpose of not only correcting for radiation, but actually measuring both K_L and K_R . Before describing the new method, some general remarks are in order.

Perhaps the simplest method of separating approximately the conductive and radiative contributions is first to measure the total conductivity as a function of temperature; and second, to use the experimental values near room temperature (where K_R is small and $K \approx K_L$) to establish a T^{-1} curve for the lattice conductivity. K_R at higher temperatures is then found by subtraction. Lee and Kingery [1960] apply this technique to ceramics and

Kanamori et al. [1968] to rock-forming minerals. Accuracy of values obtained by this technique is poor due to the difficulties of extrapolating a curve over a large range and the approximate nature of the T^{-1} law.

The best method in principle is to devise a technique of measuring accurately the total conductivity as a function of temperature and then to spectroscopically measure the infrared absorption coefficient on the same sample under exactly the same conditions. A value for K_R may then be calculated from equation (3.12) and K_L found by subtraction. See Lee and Kingery [1960] for an example of this technique. Several difficulties arise: An accurate total conductivity experiment is difficult to devise when radiative effects are important. It is inconvenient to use the same sample for both thermal and spectroscopic measurements because of the different requirements for each apparatus, and identical conditions are hard to duplicate, even with the same sample. Furthermore, quantitative spectroscopic measurements in the near infrared are not at all easy. Sample surfaces must be carefully prepared and small absolute magnitudes of radiation must be accurately measured. Complications also arise from the fact that the integral for $\bar{\epsilon}$, equation (3.11), is most sensitive to the smallest values of ϵ_λ , which are the most difficult to determine accurately. Certainly, spectroscopic measurements of

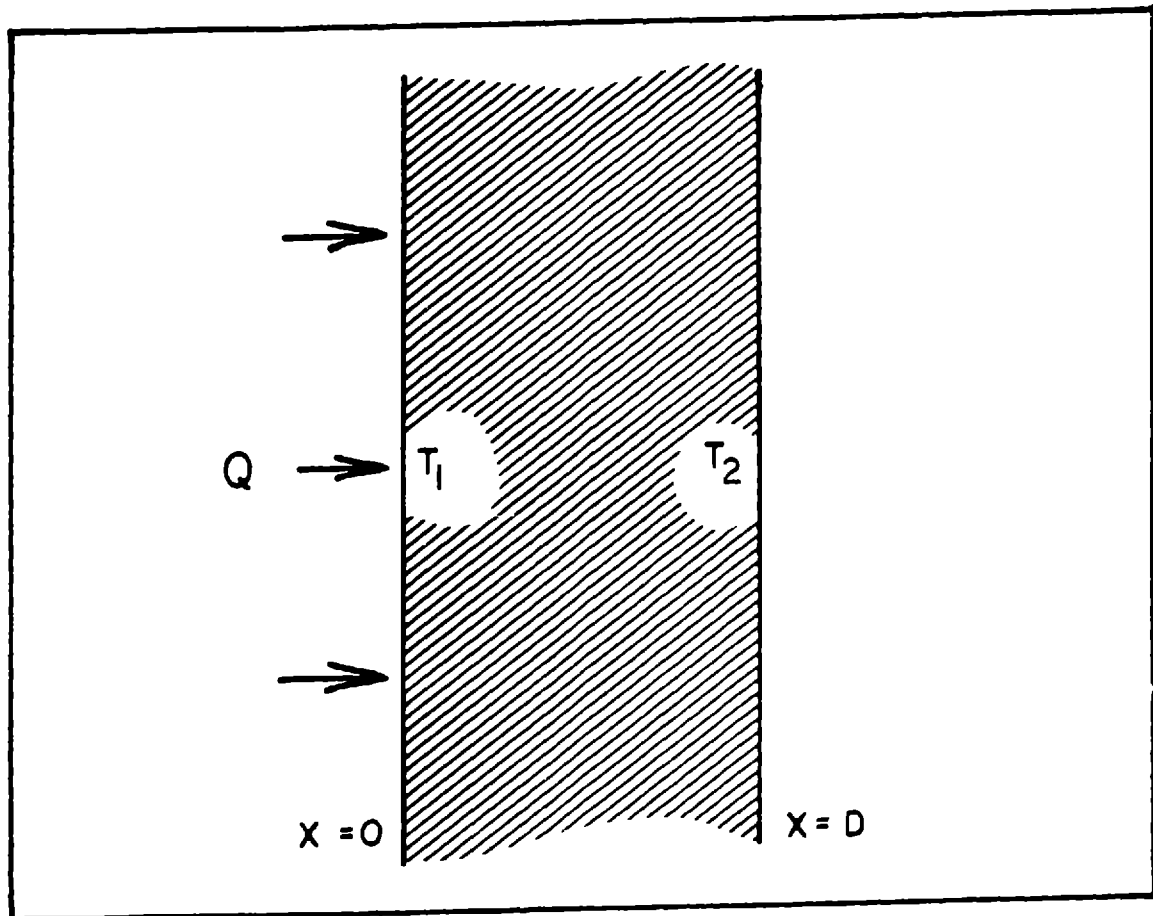
extinction coefficients have value, particularly for the understanding of the physical nature of the mechanisms, but, they are difficult, and a simpler way of measuring K_R would be desirable.

To illustrate the problems involved in thermal conductivity measurement where radiation effects are important, we consider the simple, idealized experiment, shown in Figure 4.1. The medium is a slab of thickness D with a lattice thermal conductivity K_L and a wavelength independent extinction coefficient ϵ . Suppose that a constant heat flux, Q , through the sample is maintained by heaters of known characteristics at $x=0$ and $x=D$ and the thermal gradient in the sample is kept small. Two thermocouples measure the temperatures T_1 and T_2 near the surfaces. One way to find the total thermal conductivity is to assume that $Q = -K \frac{\Delta T}{\Delta x}$ everywhere, such that K is given by

$$K = \frac{QD}{T_1 - T_2} \quad (4.1)$$

Equation (4.1) gives the true total conductivity only if the medium is optically thick ($\epsilon D \gg 1$). Otherwise, some of the heat originating at and near $x=0$ will be radiated directly to the surface $x=D$, thereby being lost to the internal heat transfer process. The temperature difference ($T_1 - T_2$) becomes smaller, and the apparent conductivity is larger than the optically thick conductivity.

Figure 4.1 Geometry of medium for idealized thermal conductivity experiment.



There is, however, another way of looking at the same experiment. Suppose that the temperature difference ($T_1 - T_2$) is held constant by varying the heat flux Q . Then, only if the sample is optically thick are the results the same as before. If the sample is not optically thick the results may differ in several ways depending on the actual method of measurement. Imagine that the amount of heat transmitted directly from $x=0$ to $x=D$ by radiation can be determined and subtracted from the total heat flux to give the internal heat flux, Q_I . Then Q_I , which is smaller than the total Q , is used to calculate K from equation (4.1) and the apparent conductivity of the medium is found to be smaller than the optically thick conductivity. Thus two views of the same experiment have given conflicting results.

In general, the sample may be thought to have a lattice conductivity, an internal radiative conductivity, and a transmission radiative conductivity. ("Conductivity" is not strictly defined here.) In the optically thick case, the transmission conductivity is zero, and the internal radiative conductivity is equal to K_R as given by equation (3.12). The first version of the idealized experiment measures the sum of the internal and transmission radiative conductivities, which may be larger than K_R , while the second version measures only the internal component, which is less than K_R . The value of

the internal component as a function of sample size is discussed by Fukao [1969]. He calls the variation the "size effect" after the similar effect on lattice conductivity in single crystals at cryogenic temperatures. Engelmann and Schmidt [1966] discuss the effect of larger than negligible thermal gradients.

In neither of the above versions of the idealized experiment can the desired values of K_L and K_R be separated. The problem is further complicated by the fact that the thermocouples may themselves participate in the emission and absorption of radiation, and thus not remain exactly at the temperature of their general surroundings. Some separation of K_L and K_R might be possible by varying the experimental geometry while keeping constant conditions (for example, by using several sample thicknesses). But, the associated difficulties, such as the measurement of small differences in the amplitude of several quantities, make the success of such a technique unlikely.

A good example of the effect of radiation on measurements is the many different values of thermal conductivity of fused silica found in the literature. This material is quite transparent in the near infrared, and the onset of radiation effects appears at temperatures only slightly above room temperature. Accordingly, the results obtained by several investigators are quite

different, particularly at higher temperatures. (See, for example, Kingery [1955]; Wray and Connolly [1959]; Devyamkova et al. [1960]; Sugawara [1967].) Though these investigators have not completely ignored radiative effects, their measurement disagreements seem too often to be attributed to differences in sample purity and not often enough to a careful analysis of radiation effects. Romashin [1969] attacks this problem admirably by measuring the thermal conductivities of both pure, clear fused silica and a ceramic made from the same material, followed by careful analysis of radiation effects. Radiative conductivity is minimized in the ceramic due to scattering, and so the difference between it and the fused material is almost solely attributable to radiation. Romashin's technique is a good one, but it unfortunately involves rather elaborate sample preparation.

Background of the New Technique

The ease and accuracy of many scientific measurements have been improved by the utilization of a time varying, but quasi-steady state technique in which frequency or phase, rather than amplitude, is measured. One such technique is the Ångström method of measuring thermal diffusivity. In this method, a low frequency sinusoidal source of heat is applied to one end of a sample, and the phase of the decaying sinusoidal temperature wave which

passes into the sample is measured at a position x . Mathematical analysis of the technique shows that the phase is essentially a function of the quantity $\left(\frac{\omega}{2\kappa}\right)^{\frac{1}{2}} x$ and surface radiation corrections, where κ is the thermal diffusivity of the medium. Since thermal diffusivity, density, specific heat, and thermal conductivity are related by

$$K = \rho C_p \kappa \quad (4.2)$$

only the values of density and specific heat, which can be obtained elsewhere, are needed to determine the thermal conductivity. This technique has been described and utilized (with correction for surface, but not internal radiation) by Kanamori et al. [1968 , 1969] , for the measurement of thermal diffusivity in rock-forming minerals.

In the Ångström method, the sources and detectors of heat are often electrical heaters and thermocouples attached directly to the sample. Problems associated with heaters and thermocouples at high temperature can be the greatest limitation on the maximum attainable experimental temperature. It would be desirable then, to have a high temperature experiment with a remote heat input and thermal sensor. The advantages of remote input and output were brought to our attention by the "flash method" (a transient method of determining thermal

diffusivity) described by Parker et al. [1961], Deem and Wood [1962], and Shaw and Goldsmith [1966]. In Parker's work, a flash tube supplies a pulsed heat input and in the second two experiments, a lead sulfide infrared radiation detector provides remote temperature measurement.

A quasi-steady state, remote input-output method of thermal diffusivity measurement has been proposed by Cowan [1961] and achieved, for example, by Wheeler [1965] and Serizawa [1969]. A modulated electron beam is used as the heat source. Cowan's mathematical analysis is rather complete but does not include the effects of internal radiation; it strictly applies only to samples which are opaque in the infrared. Nevertheless, his mathematical treatment is in some ways similar to the technique of this investigation, as presented in the next chapter, and the two should produce the same results for opaque samples.

Description of Apparatus

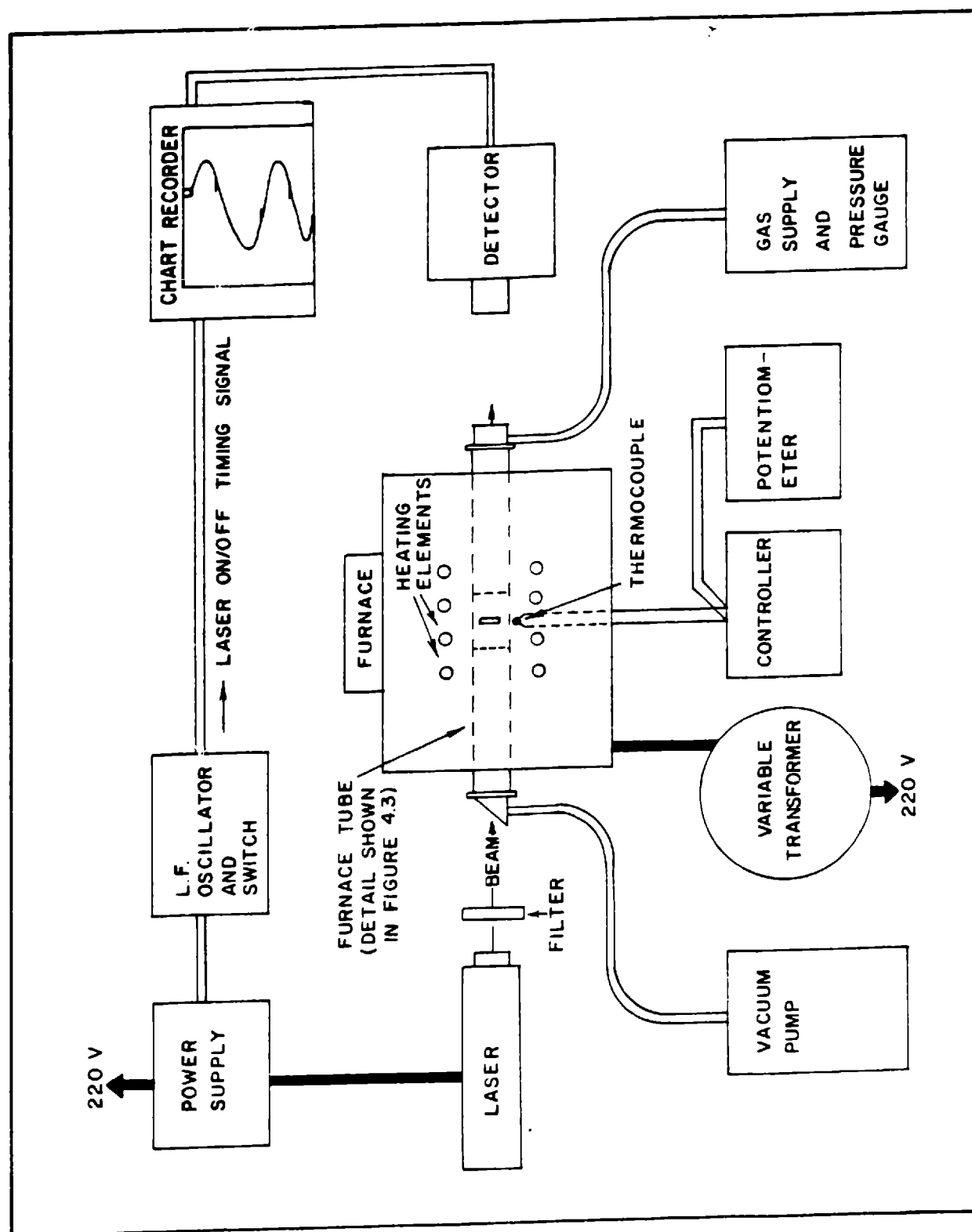
The purpose of this experiment is to calculate the lattice and radiative thermal conductivities that a sample material would have in bulk form (or in situ) from measurements of the phase of a thermal signal in a small sample. The apparatus consists of a laser, which provides an oscillating heat input to the front of a

sample enclosed in a furnace, and an infrared detector, which is focused on the back of the sample and provides the output signal. If the sample is opaque in the infrared, the detector "sees" only the back face of the sample, and the measurement is sensitive only to the thermal diffusivity, as in Cowan's method. But, if the sample is partially transparent (which is more generally the case), the detector "sees into" the sample, and the signal phase lag is less than in the opaque case. The phase of the detector signal with respect to the laser input is in this case a function of both the thermal diffusivity and infrared extinction coefficient of the sample. With a knowledge of the form of that function, and two or more independent measurements of phase, K_L and K_R can be calculated.

The experimental apparatus is shown schematically in Figure 4.2. We discuss, in order, the laser, furnace and sample assembly, and detector-output instrumentation.

A carbon dioxide gas laser capable of continuous operation for long periods was built specifically for this experiment. However, its design and operation are not unusual and similar units are now available commercially. The laser beam has a diameter of 2 cm and a maximum power of 100 watts but is generally operated in the range 10-25 watts. The laser power supply is connected to a low frequency oscillator and switch assembly which turn the beam on and off continually

Figure 4.2 Schematic diagram of experimental apparatus.



with a period of 10 to 30 seconds. Most of the energy which emerges from the laser tube is in the form of a coherent beam with a wavelength of 10.6 microns. However, in the earliest experimental work a small amount of "noise" energy was discovered at shorter wavelengths which was enough to seriously disturb the quality of the output data for the case of a relatively transparent sample. To eliminate this problem, the raw output of the laser is now passed through a band-pass filter with short wave cutoff at about 7 microns. (The filter was supplied by Infrared Industries, Inc., 62 Fourth Ave., Waltham, Massachusetts.) No significant external energy at wavelengths other than 10.6 μ now reaches the sample.

A CO₂ laser has several advantages as the oscillatory heat source for this experiment: It is conveniently placed far from the sample. The 10.6 μ beam is absorbed very strongly by silicates and most of the oxides of interest due to its coincidence with the wavelength of many structural absorption bands. This rapid surface absorption makes the laser act as a source of heat at the surface of the sample--just as if a heater had been glued to it. Furthermore, the radiation detector which provides the output data (to be described below) is not sensitive to radiation at 10.6 μ . So, if some of the laser radiation should leak around the sample, it will not appear as

noise in the output. None of the other candidates for a heat source, e.g. an arc-image furnace or an electron-beam gun, has all of these advantages.

The laser creates mainly a small oscillatory heating of the sample (of the order ± 10 °C at the sample face); the main, constant heating is provided by the large silicon carbide rod element furnace. (The furnace is Model 54233 made by Linberg Hevi-duty, 304 Hart St., Waterton, Wisconsin.) The maximum temperature attainable is 1765 °K for continuous duty and in excess of 1900 °K if short element lifetime (several days) is tolerable. There are eight heating elements, each passing through the body of the furnace perpendicular to the furnace tube. The furnace hot zone is at least 6 inches long (manufacturer's data), while the sample holder (described below) is $2\frac{1}{2}$ inches long, so constant temperature is easily maintained over the entire holder.

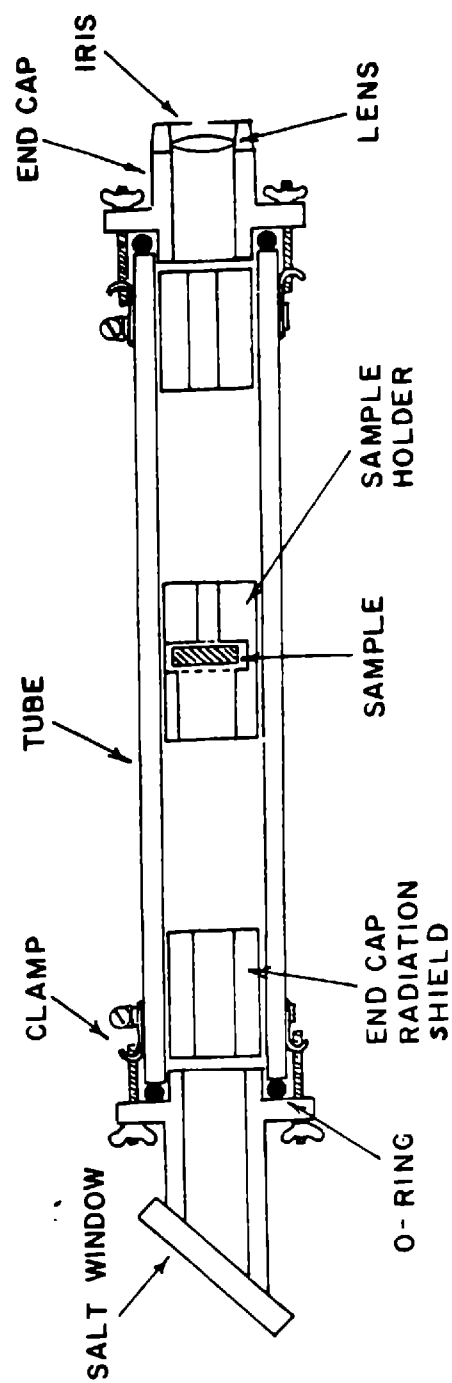
The furnace temperature is controlled by an on-off time-proportioning controller connected to a platinum + $13\frac{1}{2}$ rhodium vs. platinum thermocouple which is mounted just outside the furnace tube. Possible error in determining the sample temperature from having the thermocouple in this position (rather than right at the sample) was checked by melting a gold standard in the actual sample position in the tube without operating the laser. The error in melting temperature is less than 1

percent. The small d.c. heating of the sample produced by the laser during an experimental run is measured by using the detector in a d.c. mode as an optical pyrometer. The reported sample temperatures are the furnace temperature plus this pyrometer correction. The magnitude of the correction is in the range 0 to 50 °C.

During an experimental run, the periodic up and down furnace temperature changes produced by the on-off switching of the controller are intolerable. Smoother temperature control is achieved by turning off the controller entirely and adjusting the furnace current to maintain a constant temperature. The large thermal inertia of the furnace used is an advantage here, since temperature can easily be held within one degree centigrade for an hour--more than enough time for a measurement.

The furnace tube contains the sample holder. (The tube is Number 997 PT 134, manufactured by McDanel Refractory Porcelain Co., Beaver Falls, Pennsylvania.) It is 30 inches long with an outside diameter of 2 inches. The details are shown in Figure 4.3. The tube is made of pure, low porosity alumina; is gas-tight, and does not soften below at least 1900 °K. An o-ring sealed aluminum end cap is mounted at the laser end of the tube. The end cap is machined to accept a sodium chloride optical window which is mounted at the Brewster angle with respect to the laser beam such that

Figure 4.3 Detail of furnace tube (not
to scale).



nearly 100% of the beam is transmitted to the sample. This end-cap also contains a vacuum pump outlet fitting which connects to a standard roughing pump capable of evacuating the tube (if it were sealed) to 0.1 torr.

A similar end cap is mounted at the detector end of the furnace tube. On this cap we mount an infrared-transmitting fused silica lens of 20 cm focal length which focuses the radiation emitted by the sample onto the detector. (The lens is made of "Infrasil" and ground and polished by A.D. Jones Optical Works, 64 Cambridge St., Burlington, Mass.) An iris diaphragm placed over the lens allows variation of the magnitude of radiation striking the detector. The iris diameter adjusts from 2 to 18 mm, and the radiation magnitude may be changed by a factor of 80. This end cap also contains gas inlet and pressure gauge fittings. The experimental gas is a dry nitrogen-5% hydrogen, commercially prepared mixture. (Argon was first used, but it caused irreversible changes in sample color after high temperature runs--probably due to the presence of water in the gas.) The gas pressure in the tube, as measured by a thermistor gauge near the inlet, is maintained in the range 1 to 5 torr during an experiment, which corresponds to a measured gas flow rate of approximately 1 to 5 liters/minute.

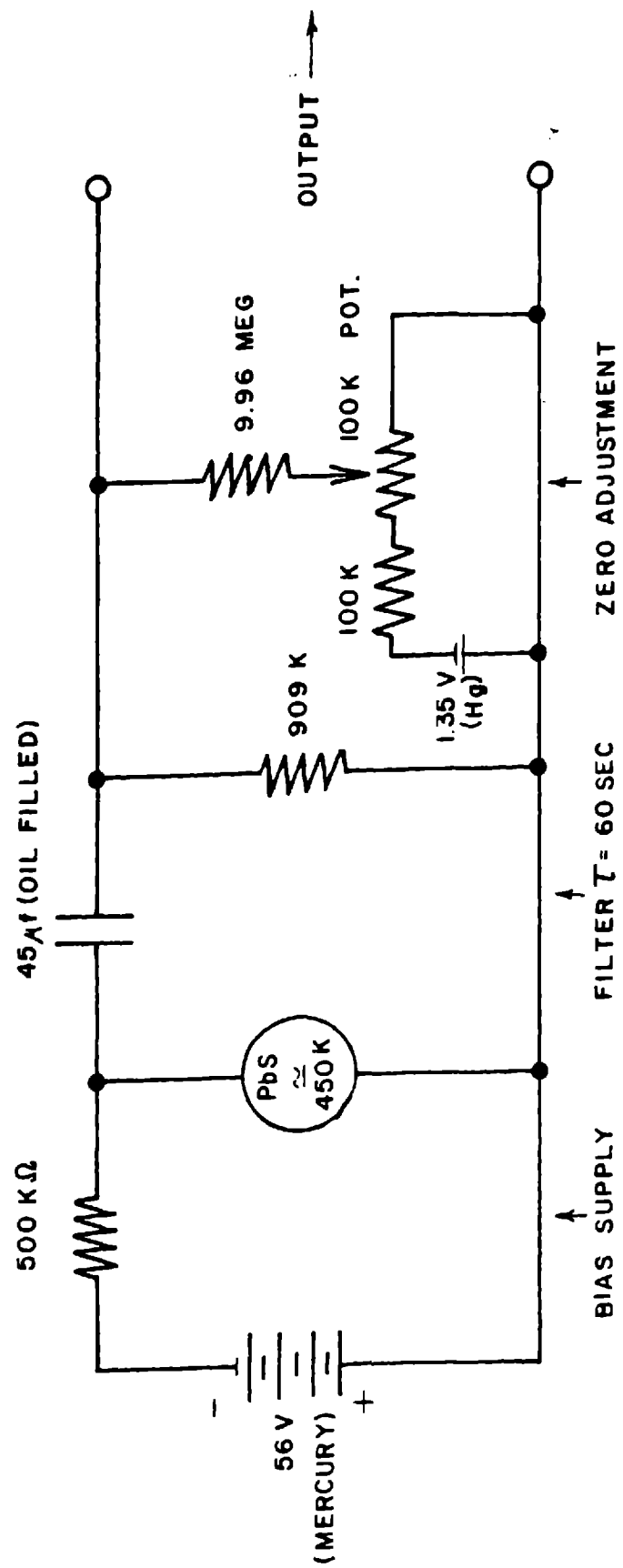
In order to maintain the vacuum integrity and spectral

characteristics of the salt window and silica lens, the temperature of the end caps must be kept well below the maximum temperature of the furnace. To keep the end caps cool, we locate, near each end cap and within the tube, a cylindrical piece of standard fire brick which has a longitudinal hole just large enough to allow radiation to pass in or out of the furnace but not strike the end cap.

The sample holder is made of pure alumina, high porosity (for low thermal conductivity) fire brick. It is cylindrical and sized to just slide into the furnace tube. A transverse slot at its center is just wide enough to hold the disk-shaped sample. The laser side of the sample holder has a longitudinal hole about 2 cm in diameter to pass the laser beam, and the detector side of the holder has a smaller longitudinal hole (about $\frac{1}{2}$ cm in diameter) which allows radiation to reach the lens and detector from only the center of the sample).

A PbS infrared detector is used. (The detector manufacturer is Santa Barbara Research Center, 75 Coromar Dr., Goleta, California.) Its area is 1 mm^2 and it has a dark resistance of 450 k ohm. It is mounted and enclosed in a foam insulated box to prevent temperature fluctuations but is not cooled below room temperature. The detector's mercury battery voltage source and high pass filter, shown in Figure 4.4,

Figure 4.4 Detector electronic circuitry.



are also enclosed in the detector box. The time constant of the filter with recorder attached is approximately 60 seconds, which is always greater than the laser switching period, so it effectively blocks only the d.c. bias voltage of the detector. The data are corrected for the phase characteristics of this filter. The a.c. signal amplitude at the recorder input is from 10^{-5} to 10^{-2} volts.

The spectral characteristics of the detector and silica lens are shown in Figure 4.5. Note that the transmission of the lens is essentially constant over the entire sensitive range of the detector; thus the lens will not affect the spectral characteristics of the detected radiation. The output of the detector, generally a distorted sine wave, is plotted on a strip chart recorder. In addition, a pip (obtained from the laser switching oscillator) is inserted into the record to mark the laser turn-on and turn-off times. The desired phase lag is measured by comparing the position of the signal zero crossings with the pips, as shown in Figure 4.6.

Figure 4.5 Detector sensitivity and lens transmission as functions of wavelength. Detector data is from manufacturer (Santa Barbara Research Center) and lens data is from Wolfe [1965] for "Infrasil" (made by Engelhard).

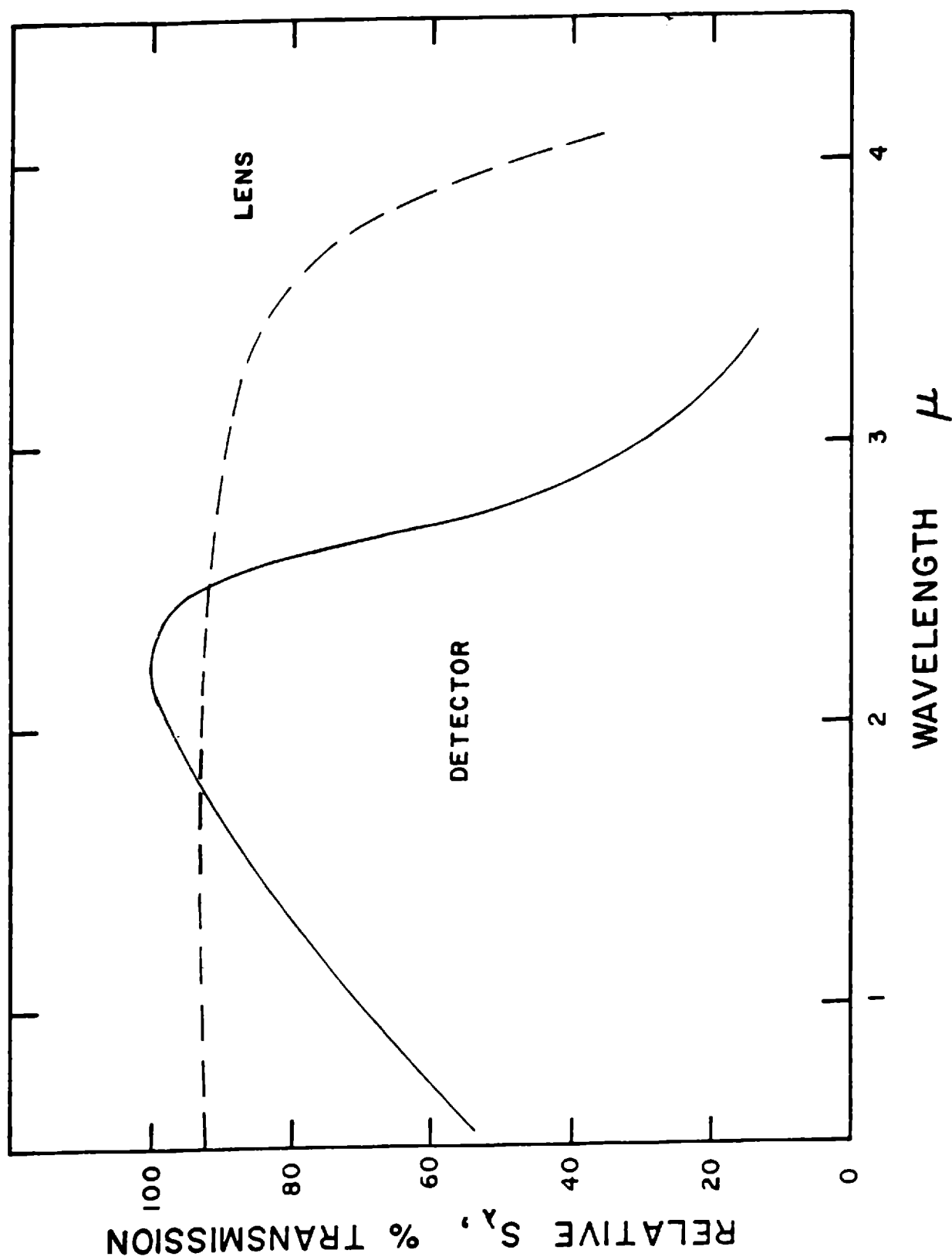
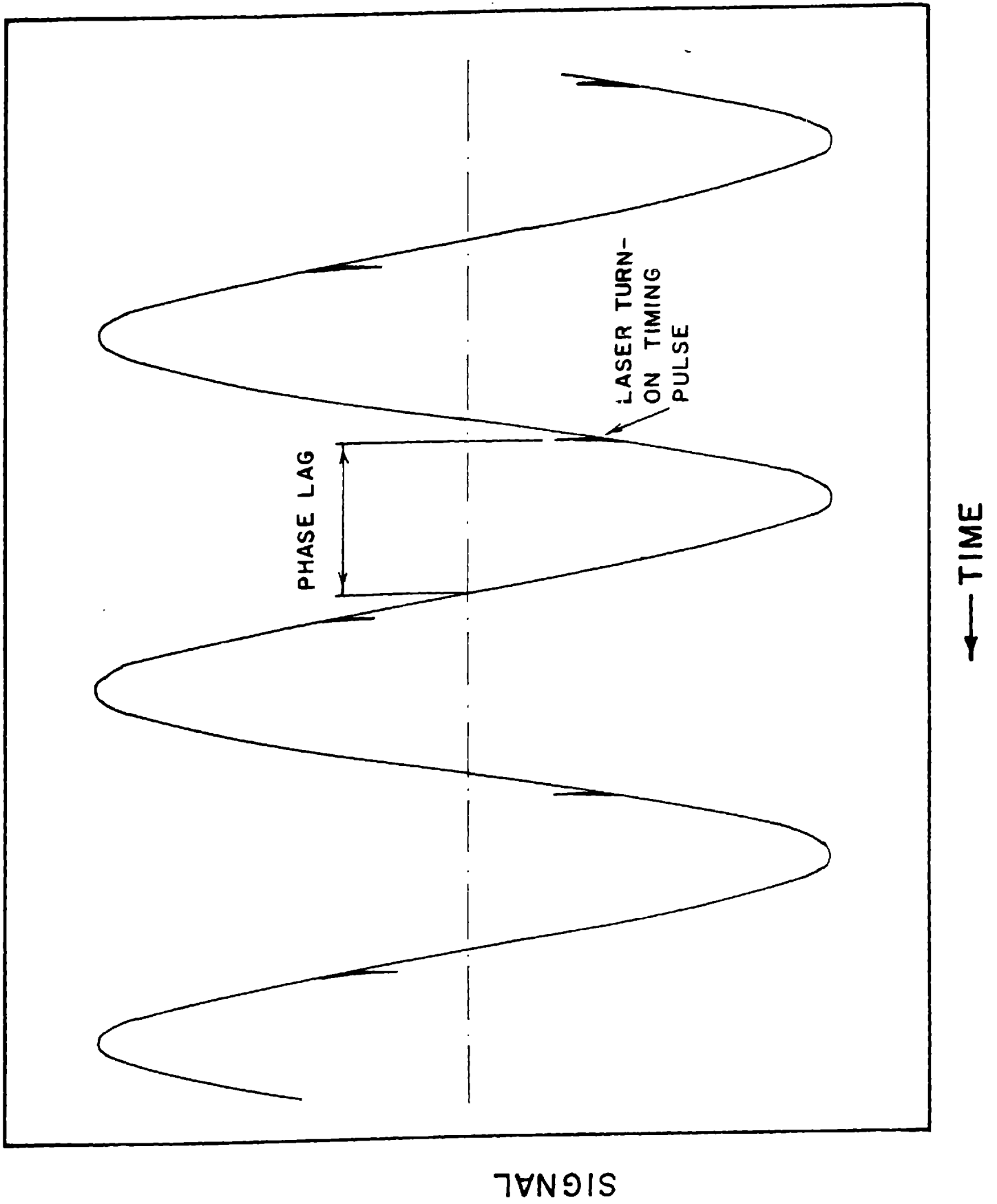


Figure 4.6 Example of recorder output, idealized. Actual output is similar, but with the addition of some noise and drift, particularly at high experimental temperatures. If sample is extremely transparent, phase lag = $\pi/2$. (Time increases to the left.)

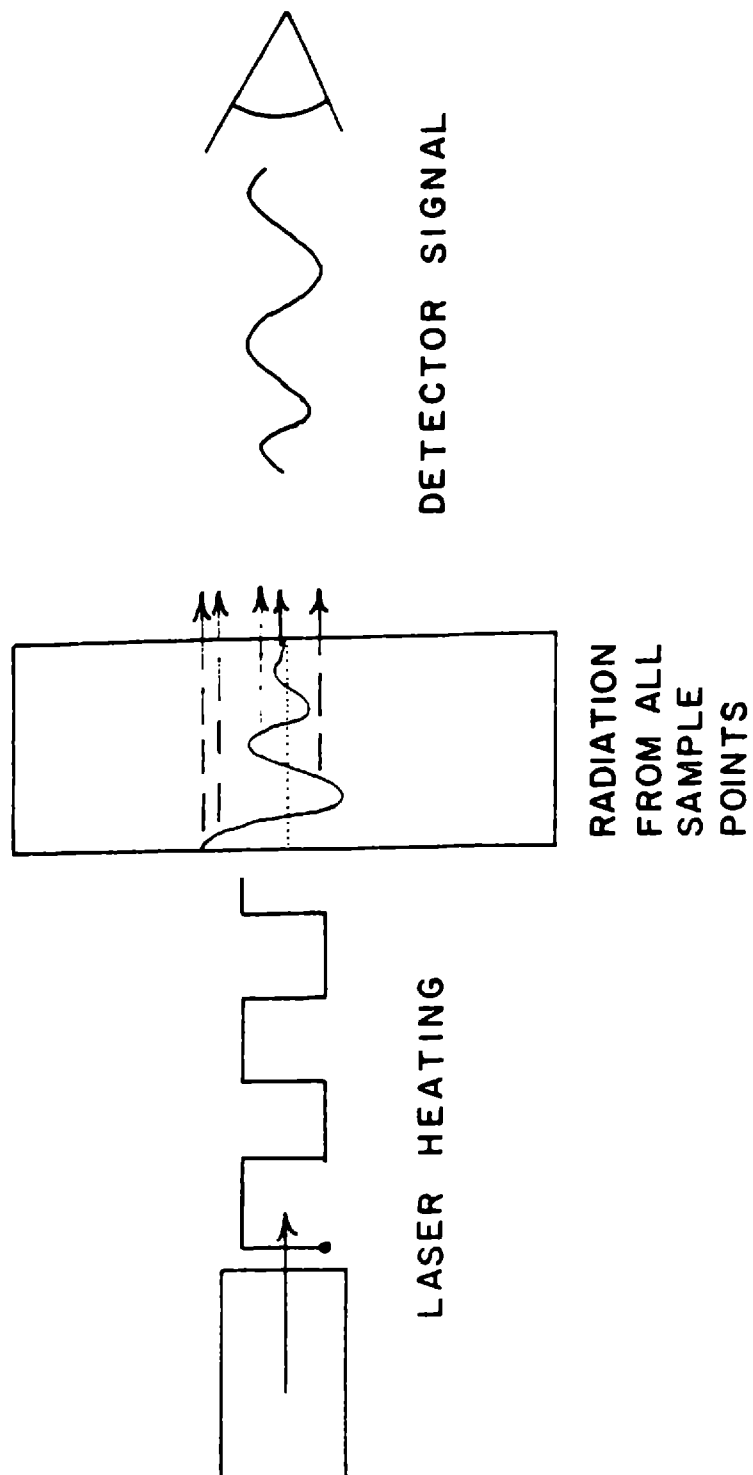


5. MATHEMATICAL ANALYSIS

The mathematical analysis of the experiment is broken down into three parts, to be discussed in the following order: (1) The radiation received at the detector which produces the signal output is functionally related to the sample temperature; (2) The temperature wave produced by the laser in the sample is found as a function of position and time; (3) The phase of the output signal is related to the lattice thermal diffusivity, $\kappa_L = K_L / \rho C_P$, and the mean extinction coefficient, $\bar{\epsilon} = 16\sigma h^2 T^3 / 3K_R$, from which K_L and K_R are calculated. The physical process to be mathematically described is illustrated in Figure 5.1.

In the entire analysis, only one-dimensional variations (in the x-direction) are considered. The assumption of one-dimensionality is valid if the diameter of the disk-shaped sample is much larger than its thickness, and if the laser radiation is nearly uniform over the sample surface. Furthermore, the radiation detector must be on the axis of the center of the sample and far from the surface. The condition most likely to be violated here is that of large sample diameter. However, Pridmore-Brown [1970] calculated the magnitude of error due to two-dimensional effects on the measurement of thermal diffusivity of disks and rods. By his criteria, this error in the present experiment is at

Figure 5.1 Illustration of the physical
process of the experiment.



most about 4%, but generally much less.

In the following analysis, terms are sometimes replaced by their approximations or dropped completely. Some of these actions are necessary to obtain the result, while others are done solely to simplify the expressions without incurring great loss of accuracy. For more complete mathematical expressions, see the Appendix.

Radiation at the Detector

Each point in the sample radiates energy in proportion to its spectral black body emissive power $e_{b\lambda}(x,t)$, but, this radiation is exponentially attenuated on its way to the surface such that the time dependent radiation per unit area leaving the sample (which is the sum of the radiation from all points) is given by

$$R_{\lambda}(t) = \int_0^D e_{b\lambda}(x,t) e^{-\epsilon_{\lambda}(D-x)} dx \quad (5.1)$$

where ϵ_{λ} is the spectral extinction coefficient of the sample, as defined earlier. The total signal at the detector, aside from geometric constants, is equation (5.1) multiplied by the detector spectral sensitivity \mathcal{S}_{λ} and integrated over all wavelengths:

$$R(t) = \int_0^{\infty} g_{\lambda} R_{\lambda}(t) d\lambda \quad (5.2)$$

Substitution of equation (5.1) into (5.2) gives

$$R(t) = \int_0^{\infty} g_{\lambda} \int_0^D e b_{\lambda}(x, t) e^{-\epsilon_{\lambda}(D-x)} dx d\lambda \quad (5.3)$$

We now define a wavelength independent mean extinction coefficient $\bar{\epsilon}$ which replaces ϵ_{λ} in equation (5.3). This definition of $\bar{\epsilon}$ is the key simplification of this analysis. It is given by the equation

$$e^{-\bar{\epsilon}(D-x)} = \frac{\int_0^{\infty} g_{\lambda} e b_{\lambda}(x, t) e^{-\epsilon_{\lambda}(D-x)} d\lambda}{\int_0^{\infty} g_{\lambda} e b_{\lambda}(x, t) d\lambda} \quad (5.4)$$

The wavelength integral in equation (5.3) may now be performed to give, aside from constants of proportionality,

$$R(t) = \int_0^D T^* e^{-\bar{\epsilon}(D-x)} dx \quad (5.5)$$

where T is the temperature in the sample. (In the rest of this analysis, constants of proportionality are often dropped where they do not affect the phase of the result.) Let the temperature in the sample be given by

$$T = T_0 + T(x, t)$$

where T_0 is the constant background temperature produced by the furnace and the d.c. component of laser heating. $T(x, t)$ is the time-varying temperature produced by the laser. Since, by adjustment of the laser power, $T(x, t)$ may be kept small compared to T_0 , the fourth power of the sample temperature may be expanded in a power series as

$$T^4 = T_0^4 + 4T_0^3 T(x, t) + \dots$$

Substitution of the first time-varying term of this expansion into equation (5.5) gives, aside from constants,

$$R(t) = \int_0^D T(x, t) e^{-\bar{\epsilon}(D-x)} dx \quad (5.6)$$

Equation (5.6) is the basis of the experimental method. If the temperature $T(x, t)$ can be found as a function of lattice thermal diffusivity, mean extinction coefficient, and laser switching frequency, then a measurement of the phase of the detector signal, $R(t)$, at two frequencies can be used to calculate κ_L and $\bar{\epsilon}$.

Much of the validity of the remaining analysis depends upon whether or not $\bar{\epsilon}$, as defined by equation (5.4) and used to find equation (5.6), is similar to

$\bar{\epsilon}$ defined earlier by equation (3.11). Note that only the earlier definition of $\bar{\epsilon}$ is strictly valid for calculating K_R . To show that the two forms are always equivalent is impossible, but it is possible to show that they are quite close over the range of conditions of this experiment. In fact, simple measurement error generally overshadows error caused by the differences in the two definitions of mean extinction coefficient.

For example, consider a material with the idealized spectral extinction coefficient at 2000 °K given in Figure 5.2. The true mean extinction coefficient calculated from equation (3.11) for this material is

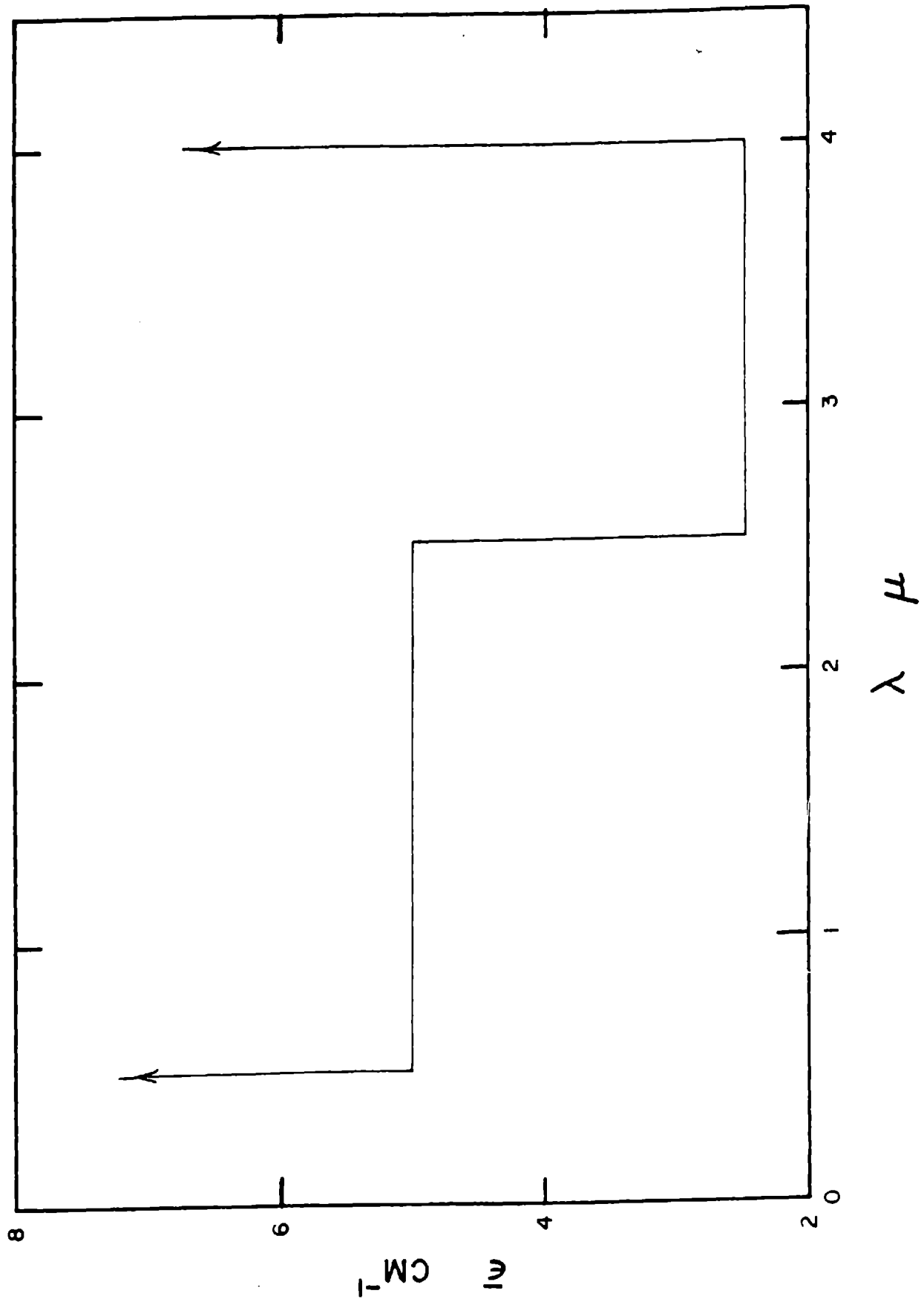
$$\bar{\epsilon} \cong 4.6$$

This is, of course, the correct value to use in calculating K_R . To compute the corresponding $\bar{\epsilon}$ from equation (5.4), note that for all but the most transparent of materials, most of the radiation received at the detector arises near the back of the sample, where the quantity $(D-x)$ is a fairly small number. Assume, for simplicity, that $(D-x)=0.1$ cm. The resulting mean extinction coefficient is

$$\bar{\epsilon} \cong 4.8$$

which is within 5% of the first value. This result is only a weak function of the value of $(D-x)$. Thus, for the stated conditions, at least, the two definitions of $\bar{\epsilon}$ are sufficiently equivalent for our purposes.

Figure 5.2 Spectral extinction coefficient
of a hypothetical material for use in
comparison of definitions of mean
extinction coefficient.



The values of $\bar{\epsilon}$ resulting from the two definitions of $\bar{\epsilon}$ are similar because both are heavily weighted near the peak of ϵ_{λ} , and because the quantity $e^{-\epsilon_{\lambda}(D-x)}$ which occurs in equation (5.4) and the quantity $1/\epsilon_{\lambda}$ which occurs in equation (3.11) depend similarly on ϵ_{λ} . In fact, the difference in values is caused almost entirely by the non-uniformity of the detector spectral sensitivity \mathcal{S}_{λ} ; the new $\bar{\epsilon}$ might be considered to be the original $\bar{\epsilon}$ weighted by \mathcal{S}_{λ} . It follows (for a PbS detector), that whenever the wavelengths important to $\bar{\epsilon}$ are less than about 3μ , satisfactory results are expected from the experiment. For olivine, this corresponds to temperatures greater than about 800 °K. It would be desirable in a future experiment to use a detector with a more uniform \mathcal{S}_{λ} over the wavelengths of interest (e.g. a thermocouple detector).

Temperature in the Sample

The time variation of the heat flux generated by the laser at the sample face $x=0$ is that of a square wave. In anticipation of the fact that the higher frequency components of the temperature wave in the sample decay very rapidly as they pass into the sample, we consider only the fundamental sinusoidal component of the flux, given, aside from constants, by

$$F = F_0 \sin \omega t = -i F_0 e^{i\omega t} \quad (5.7)$$

where F_0 is the laser beam power density, and ω is the laser switching frequency. Assume then, that the temperature wave produced in the sample is a sum of decaying waves in the positive and negative x-directions such that

$$T(x,t) = U e^{-\beta x} e^{i(\omega t + \delta)} + W e^{\beta x} e^{i(\omega t + \psi)} \quad (5.8)$$

Expressions for U, W, δ , and ψ (which are real numbers) will now be found from the boundary conditions at $x=0$ and $x=D$, and an expression for the propagation coefficient β (which is a complex number) will be found from the general heat flow equation including radiation.

In equation (5.8) the U -wave may be thought of as a primary wave generated at $x=0$ and the W -wave as a reflection caused by the boundary at $x=D$. The W -wave then decays as it moves back through the sample and is much smaller than the U -wave when it gets to $x=0$. For this reason, we assume that the U -wave only, need be considered in using the boundary conditions at $x=0$, whereas both waves should be considered at $x=D$.

Boundary conditions which involve radiation to and

from a surface are highly non-linear and can seldom be specified exactly [Carslaw and Jaeger, 1959]. We approximate the boundary condition as follows: the laser input flux balances the sum of the heat conduction into, and radiation away from, the sample, such that

$$F = -K_{eff} \left. \frac{dT}{dx} \right|_{x=0} + q_R \Big|_{x=0} \quad (5.9)$$

where K_{eff} is the "effective thermal conductivity" of the sample and q_R is the heat radiated away from the surface. The effective thermal conductivity is the sum of the lattice conductivity and a rough approximation to the internal radiative conductivity of the sample:

$$K_{eff} = K_L + \frac{4\sigma n^2 T_0^3 D}{1 + \frac{3}{4} \bar{\epsilon} D} \quad (5.10)$$

(Note that if $\bar{\epsilon} D \gg 1$, then $K_{eff} = K = K_L + K_R$).

The heat radiated from the surface is given by

$$q_R \Big|_{x=0} = 2 \int_0^{\bar{\epsilon} D} e^{b(x', t)} E_2(x') dx'$$

where the exponential integral function, E_2 , may be approximated [Sparrow and Cess, 1966] as

$$E_2(x') = \frac{3}{4} e^{-\frac{3}{2} x'}$$

so that, if small temperature variations are assumed, the expression for q_r becomes

$$q_r|_{x=0} = 6\bar{\epsilon}\sigma T_0^3 \int_0^D U e^{-\beta x} e^{i(\omega t + \delta)} e^{-\frac{3}{2}\bar{\epsilon}x} dx \quad (5.11)$$

Substitution of equations (5.7), (5.10), (5.11), and the derivative of (5.8) into equation (5.9) gives

$$-iF_0 = U e^{i\delta} H$$

where

$$H = \beta k_{eff} + \frac{6\bar{\epsilon}\sigma T_0^3}{\beta + \frac{3}{2}\bar{\epsilon}} \left[1 - e^{-(\beta + \frac{3}{2}\bar{\epsilon})D} \right] \quad (5.12)$$

Equation (5.12), expanded into its real and imaginary parts and solved for δ and U gives

$$\delta = \tan^{-1} (-H_r / -H_i)$$

and

$$U = \frac{-F_0}{H_r \sin \delta + H_i \cos \delta}$$

$$(5.13)$$

where H_r and H_i are the real and imaginary parts of H .

The boundary condition at $x=D$, from which V and ψ are found, is similar, except that there is no laser flux:

$$0 = K_{eff} \left. \frac{dT}{dx} \right|_{x=D} + q_r \Big|_{x=D}$$

where both the U and W -waves must now be considered.

Following a procedure similar to the above gives

$$\begin{aligned} 0 = K_{eff} & \left[\beta U e^{-\beta D} e^{i\delta} - \beta W e^{\beta D} e^{i\psi} \right] \\ & + 6\bar{\epsilon}\sigma T_0^3 \left[\frac{U e^{i\delta}}{\beta - \frac{3}{2}\bar{\epsilon}} (e^{-\frac{3}{2}\bar{\epsilon}D} - e^{-\beta D}) \right. \\ & \quad \left. - \frac{W e^{i\psi}}{\beta + \frac{3}{2}\bar{\epsilon}} (e^{-\frac{3}{2}\bar{\epsilon}D} - e^{\beta D}) \right] \end{aligned} \quad (5.14)$$

W and ψ are found by substituting equation (5.13) into (5.14) and solving the result. At this point, U, W, δ , and ψ have all been found in terms of experimental knowns and $\beta, \bar{\epsilon}$, and $K_L = K_L \rho C_P$.

To find β , consider the general equation of heat flow (including radiation) which results from the substitution of the wavelength integral of equation (3.5) into equations (1.1) and (1.2):

$$\begin{aligned} \rho C_P \frac{dT}{dt} = K_L \frac{d^2 T}{dx^2} - 4\bar{\epsilon}\sigma n^2 T^4 \\ + 2\bar{\epsilon}^2 \sigma n^2 \int_0^D T^4(x') E_1(\bar{\epsilon}|x-x'|) dx' \end{aligned} \quad (5.15)$$

There is no general solution to this equation, but

there are conditions under which a solution of the form

$$T = T_0 U e^{-\beta x} e^{i(\omega t + \delta)} \quad (5.16)$$

is successful. Approximate T^4 , as before, by

$$T^4 = T_0^4 + 4T_0^3 U e^{-\beta x} e^{i(\omega t + \delta)}$$

and substitute it into equation (5.15) to give

$$e^{-\beta x} (1 - P \left(\frac{\beta}{\bar{\epsilon}} \right)^2 + iq) = \frac{1}{2} \bar{\epsilon} \int_0^D e^{-\beta x'} \bar{\epsilon}_1(\bar{\epsilon} |x-x'|) dx' \quad (5.17)$$

where $P = \frac{K_L \bar{\epsilon}}{16 \sigma n^2 T_0^3}$

and $q = \frac{\rho C_p \omega}{16 \sigma n^2 T_0^3 \bar{\epsilon}}$.

Now change variables to $z = \bar{\epsilon}(x-x')$ if $(x-x') > 0$

and $z = \bar{\epsilon}(x'-x)$ if $(x-x') < 0$

Equation (5.17) becomes, with $\frac{\beta}{\bar{\epsilon}} = h$,

$$1 - Ph^2 + iq = \frac{1}{2} \left[\int_0^{\bar{\epsilon}x} e^{h^2 z} \bar{\epsilon}_1(z) dz + \int_0^{\bar{\epsilon}(D-x)} e^{-h^2 z} \bar{\epsilon}_1(z) dz \right] \quad (5.18)$$

To find the value of β , equation (5.18) must be solved for h .

First, consider an optically thick medium ($\epsilon D \gg 1$) with the additional condition $h < 1$. The integrals on the right hand side of equation (5.18) may then be evaluated as in Kourganoff [1963] to give

$$(\text{Integrals}) = 2 \left(1 + \frac{1}{3} h^2 + \frac{1}{5} h^4 + \dots \right) \quad (5.19)$$

The fact that this is the only case for which the integrals may be evaluated exactly implies that it is also the only case in which a temperature wave of the form (5.16) is a strictly valid solution to equation (5.15). However, the integrals may be approximated for other conditions to extend the range of usefulness of the solution (5.16).

Consider the case $h < 1$, but do not otherwise restrict the value of ϵ . Assume that most of the contribution to the integrals of equation (5.18) arises when $x = \frac{1}{2}D$. This assumption is chosen because the internal radiation should have its maximum effect at $x = \frac{1}{2}D$, the sample center. If this value of x is used to evaluate the integrals, they become

$$(\text{Integrals}) = 2 \left(1 + C_1 + C_2 h^2 + C_3 h^4 + \dots \right) \quad (5.20)$$

where

$$C_1 = -E_2 \left(\frac{\bar{E}D}{2} \right)$$

$$C_2 = \frac{1}{3} - \frac{\bar{E}D}{4} e^{-\frac{\bar{E}D}{2}} - E_4 \left(\frac{\bar{E}D}{2} \right)$$

$$C_3 = \frac{1}{5} - \frac{\bar{E}D}{48} e^{-\frac{\bar{E}D}{2}} \left[\left(\frac{\bar{E}D}{2} \right)^2 + \bar{E}D + 6 \right] - E_6 \left(\frac{\bar{E}D}{2} \right)$$

Note that equation (5.20) reduces exactly to (5.19) for $\bar{E}D \gg 1$. This fact justifies to some extent the assumption of $x = \frac{1}{2}D$ used in approximating the integrals.

Now, consider the opposite case, $h \gg 1$. The integrals are now equal to zero. Equation (5.20) gives approximately the correct result if the series in powers of h is truncated at the fourth term. There is no theoretical justification for this truncation. It appears as though an assumption sufficient for our purposes is that equation (5.20) is valid for all h , if the above mentioned series truncation is used. This assumption is completely unsupported for $h \cong 1$. In the actual experiment, it is possible to avoid most of the problems in evaluating h by adjustment of the laser switching frequency to maintain the condition $h < 1$. (Note that $h \ll 1$ is not required.)

When equation (5.20), with truncation of the series, is substituted in equation (5.18), the equation for h becomes

$$-ph^2 + iq = C_1 + C_2 h^2 + C_3 h^4 \quad (5.21)$$

or, written in terms of β ,

$$-p\beta^2 + iq\bar{E}^2 = C_1 \bar{E}^2 + C_2 \beta^2 + \frac{C_3 \beta^4}{\bar{E}^2}$$

which is a fourth order complex algebraic equation in β . But, it is only a second order equation in β^2 , and can be easily solved for β_r and β_i , the real and imaginary parts of β .

What does equation (5.21) for h (or β) mean? If the medium is optically thick, the equation reduces to

$$-ph^2 + iq = \frac{1}{3} h^2$$

and the solution for β is

$$\beta = (1+i) \left[\frac{\rho C_p \omega}{2(K_L + K_R)} \right]^{\frac{1}{2}}$$

This solution is that expected in the ⁰Angström method for no surface radiation, or in Cowan's method. If the medium is optically thin, however, the equation reduces to

$$-ph^2 + iq = -1$$

and the solution for β is

$$\beta = (1+i) \left[\frac{\rho C_p \omega}{2 K_L} \right]^{\frac{1}{2}}$$

which is, again, as expected, since radiation does not participate in the conduction process within an optically thin medium. Note that only for the optically thick or thin cases does $\beta_r = \beta_i$.

As a final comment in this section, we discuss the

concept of optical thickness as it applies to a non-steady problem. From the form of the heat equation with radiation, it appears that for the oscillatory but quasi-steady state case the parameter $h^{-1} = \bar{\epsilon}/\beta$ must be considered along with the dimensionless optical thickness, $\bar{\epsilon}D$. Only if both these parameters are large does the optically thick solution for temperature and radiation apply. An example of the implications of h^{-1} can be found in the following rough analysis of the Ångström method. Generally, the sample used is one or more thermal wavelengths long. Assume, for simplicity, that it is exactly one wavelength long. Then, $\beta \cong \frac{2\pi}{D}$ and $\kappa' < \bar{\epsilon}D$. Thus, the Ångström method sample is "less optically thick" than a sample of the same size but used in a steady state experiment. If this effect is not taken into account, the accuracy of results obtained by the Ångström method at high temperatures for internally radiating media is suspect.

Phase of the Output Signal

The final step of the analysis is to find the phase of the output signal as a function of κ_L and $\bar{\epsilon}$. This is accomplished by the substitution of equation (5.8) for the sample temperature into the output signal equation (5.6). The result is

$$R(t) = U e^{i(\omega t + \delta)} \int_0^D e^{-\beta x} e^{-\bar{E}(D-x)} dx \quad 115$$

$$+ W e^{i(\omega t + \psi)} \int_0^D e^{\beta x} e^{-\bar{E}(D-x)} dx \quad (5.22)$$

If the integrals in equation (5.22) are evaluated, we find

$$R(t) = \frac{U e^{i(\omega t + \delta)}}{(\bar{E} - \beta)} \left[e^{-\beta D} - e^{-\bar{E} D} \right] \quad (5.23)$$

$$+ \frac{W e^{i(\omega t + \psi)}}{(\bar{E} + \beta)} \left[e^{\beta D} - e^{-\bar{E} D} \right]$$

Equation (5.23) can be written in the form

$$R(t) = R_0 e^{i(\omega t + \phi)} \quad (5.24)$$

where ϕ is the phase of the output signal and R_0 is time-independent. The equation for ϕ which results from substitution of equation (5.24) into (5.23) is

$$R_0 e^{i\phi} = \frac{U e^{i\delta}}{(\bar{E} - \beta)} \left[e^{-\beta D} - e^{-\bar{E} D} \right] \quad (5.25)$$

$$+ \frac{W e^{i\psi}}{(\bar{E} + \beta)} \left[e^{\beta D} - e^{-\bar{E} D} \right]$$

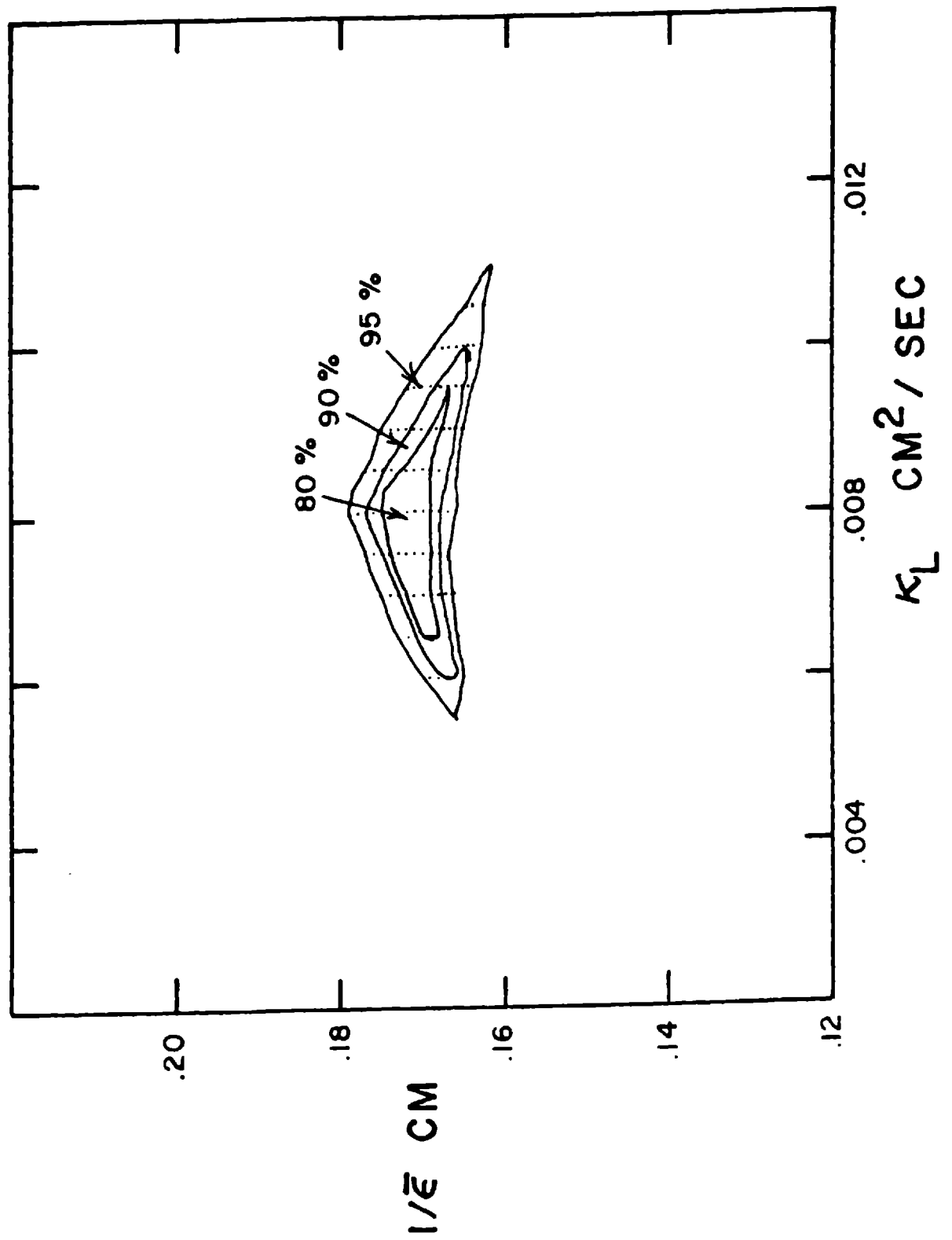
where U , W , δ , ψ , and β have been found in the previous sections as functions of K_L , \bar{E} , ω , and

experimental knowns. Thus, equation (5.25) is the desired equation for ϕ as a function of κ_L and $\bar{\epsilon}$. All experimental results are based on this equation.

Method of Data Reduction

In general, two measurements of ϕ (each at a different frequency) are sufficient to determine κ_L and $\bar{\epsilon}$. Each measurement is obtained by averaging the phase of at least five waveforms, and calculating a confidence interval based on a normal distribution of random error. To this confidence interval, we add ± 0.01 radians to allow for systematic error. Equation (5.25) cannot be directly inverted to find solutions for κ_L and $\bar{\epsilon}$ from measurements of ϕ . Instead, it is evaluated in the forward direction (by computer) to find the range of all possible pairs of κ_L and $\bar{\epsilon}$ which give theoretical phase values within the stated confidence intervals of the measured phase values. The κ_L and $\bar{\epsilon}$ pairs thus obtained are called "good solutions." For example, in Figure 5.3 we show the range of good solutions for aluminum oxide (at 1200 °K) with 80%, 90%, and 95% confidence intervals. For the remaining results, a 90% confidence interval is chosen.

Figure 5.3 Example of method of obtaining solutions for photon mean free path, $1/\bar{\epsilon}$, and lattice thermal diffusivity, κ_L . Shown are the ranges of good solutions for sintered aluminum oxide at 1200 °K for 80%, 90% and 95% confidence intervals.



6. RESULTS

Complete experimental results are presented below for the following materials:

- (1) sintered aluminum oxide, Al_2O_3
- (2) sintered forsterite, $\text{Fo}=\text{Mg}_2\text{SiO}_4$
- (3) single crystal olivine, $\text{Fo}_{86}\text{Fa}_{14}$
- (4) single crystal olivine, $\text{Fo}_{92}\text{Fa}_8$
- (5) twin sisters dunite, $\text{Fo}_{95}\text{Fa}_5$
- (6) single crystal enstatite, $\text{En}_{90}\text{Fs}_{10}$

For each material, one table describes the sample, and a second table lists the ranges of good solutions for lattice thermal diffusivity, κ_L , and inverse mean extinction coefficient, $1/\bar{\epsilon}$ (or photon mean free path), as functions of temperature. Two figures show the corresponding values of photon mean free path and total and radiative thermal conductivities as functions of temperature.

Table 6.1 Description of sample, aluminum oxide
 Al_2O_3 , sintered.

| Property | Value | Comment |
|--|--|---|
| Density | 3.95 g/cm ³ | picnometer |
| Refractive index | 1.76 | estimate from composition |
| Grain size | 20 μ | thin section |
| Void size | < 1 μ | |
| Composition | Al ₂ O ₃ 99 wt.% SiO ₂ 1 " | } manufacturer's data (Norton Co., Worcester, Mass.) |
| Thickness | 0.645 cm | |
| Mean diameter | 2 cm | trapezoidally shaped |
| Appearance | | |
| before heating | cream to white colored, smooth | |
| after heating | same, but slightly whiter | |
| Specific heat ^a | <u>.255 + .0335 x 10⁻³T - .007/(T x 10⁻³)² cal/g^oC</u> | |
| ^a expression from [Goranson, 1942]. | | |

Table 6.2 Results for aluminum oxide Al_2O_3 , sintered, range of good solutions at 90% confidence interval.

| Temperature $^{\circ}\text{K}$ | κ_L cm^2/sec | $1/\bar{\epsilon}$ cm | K cal/cm sec $^{\circ}\text{C}$ |
|--------------------------------|-------------------------------------|-----------------------|---------------------------------|
| 530 | .050 -.062 | .001-.135 | .0478-.0600 |
| 634 | .033 -.045 | .096-.196 | .0340-.0450 |
| 717 | .026 -.028 | .174-.196 | .0279-.0299 |
| 813 | .020 -.025 | .142-.186 | .0234-.0286 |
| 1007 | .0075-.0100 | .174-.186 | .0121-.0150 |
| 1203 | .0060-.0100 | .166-.177 | .0130-.0175 |
| 1390 | .0050-.0060 | .142-.147 | .0140-.0153 |
| 1589 | .0005-.0035 | .126-.138 | .0115-.0161 |
| 1924 | .0005-.0105 | .001-.069 | .0100-.0135 |
| 1591 ^a | .0010-.0035 | .121-.127 | .0117-.149 |
| 734 ^a | .030 | .184 | .0328 |
| 550 ^a | .052 | .017 | .0503 |

^a descending temperature points to check reproducibility.

Figure 6.1 Photon mean free path in sintered aluminum oxide, Al_2O_3 . Open circles are points measured at descending temperature. The lowest curved line is obtained by Lee and Kingery [1960] for a material of $V_{\text{por}} = 0.25\%$ and $r = 0.7 \mu$. The upper curve is for a material with the same characteristics except $V_{\text{por}} = 1.0\%$, which is the approximate porosity of our material.

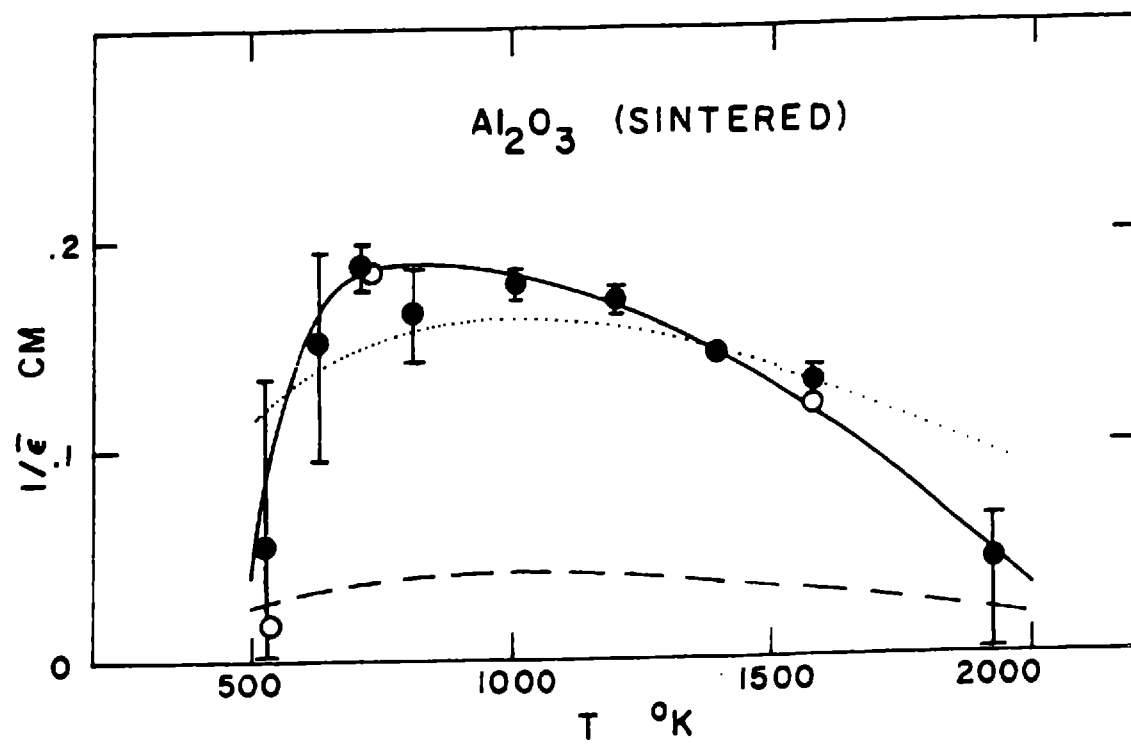


Figure 6.2 Total and radiative thermal conductivities in sintered aluminum oxide, Al_2O_3 . Open circles are points measured at descending temperature and the x's are data of Lee and Kingery [1960].

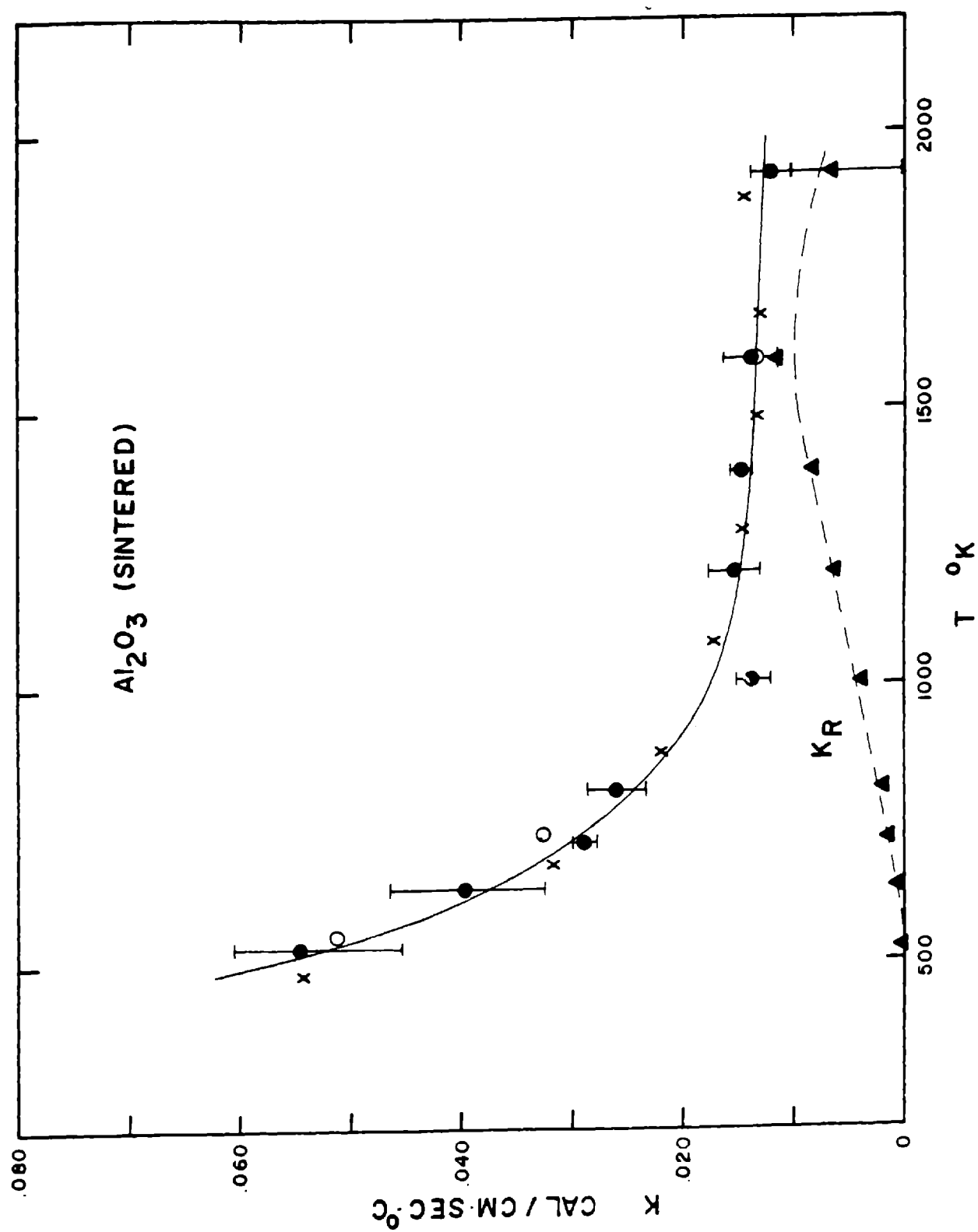


Table 6.3 Description of sample, forsterite
 $\text{Fo}=\text{Mg}_2\text{SiO}_4$, sintered.

| Property | Value | Comment |
|----------------------------|---|--|
| Density | 3.05 g/cm ³ | picnometer |
| Refractive index | 1.66 | estimate from composition |
| Grain size | 5 μ | thin section |
| Void size | $\leq 1 \mu$ | |
| Composition | olivine | } x-ray (manufacturer: American Lava Co.) |
| | structure 99% | |
| Thickness | 0.297 cm | |
| Mean diameter | 1 cm | rectangular |
| Appearance | | |
| before heating | cream colored, smooth | |
| after heating | same, possibly slightly increased grain size | |
| Specific heat ^a | $.255 + .047 \times 10^{-3}T - .006/(T \times 10^{-3})^2$ cal/g°C | |

^a as given by [Orr, 1953].

Table 6.4 Results for forsterite $\text{Fo}=\text{Mg}_2\text{SiO}_4$, sintered, range of good solutions at 90% confidence interval.

| Temperature $^{\circ}\text{K}$ | κ_L cm^2/sec | $1/\bar{\epsilon}$ cm | K cal/cm sec $^{\circ}\text{C}$ |
|--------------------------------|-------------------------------------|-----------------------|---------------------------------|
| 543 | .0098-.0136 | .206-.218 | .0084-.0114 |
| 632 | .0074-.0100 | .202-.214 | .0071-.0092 |
| 812 | .0058-.0076 | .178-.186 | .0068-.0085 |
| 1006 | .0037-.0049 | .142-.150 | .0061-.0074 |
| 1204 | .0013-.0021 | .109-.114 | .0048-.0058 |
| 1392 | .0015-.0055 | .029-.067 | .049-.069 |
| 1582 | .0003-.0042 | .025-.055 | .045-.061 |

Figure 6.3 Photon mean free path in
sintered forsterite, $\text{Fo}=\text{Mg}_2\text{SiO}_4$.

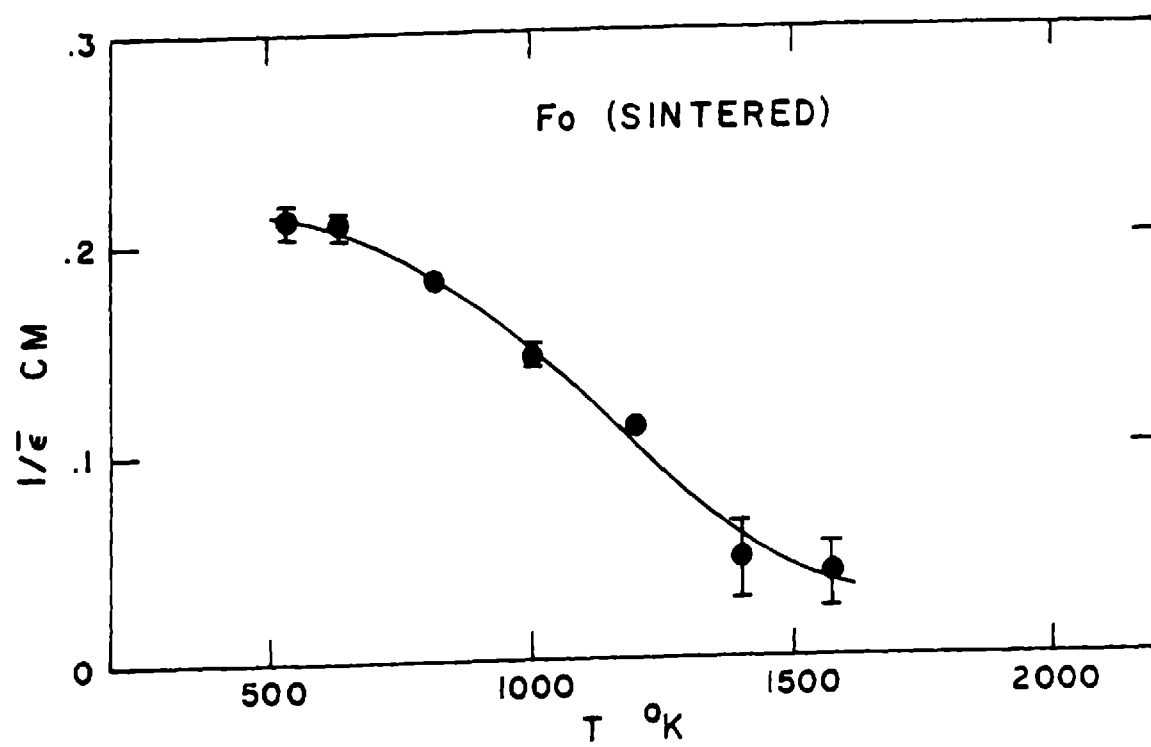


Figure 6.4 Total and radiative thermal
conductivities in sintered forsterite,
 $\text{Fo}=\text{Mg}_2\text{SiO}_4$. The x's are data of Kingery
et al. [1954].

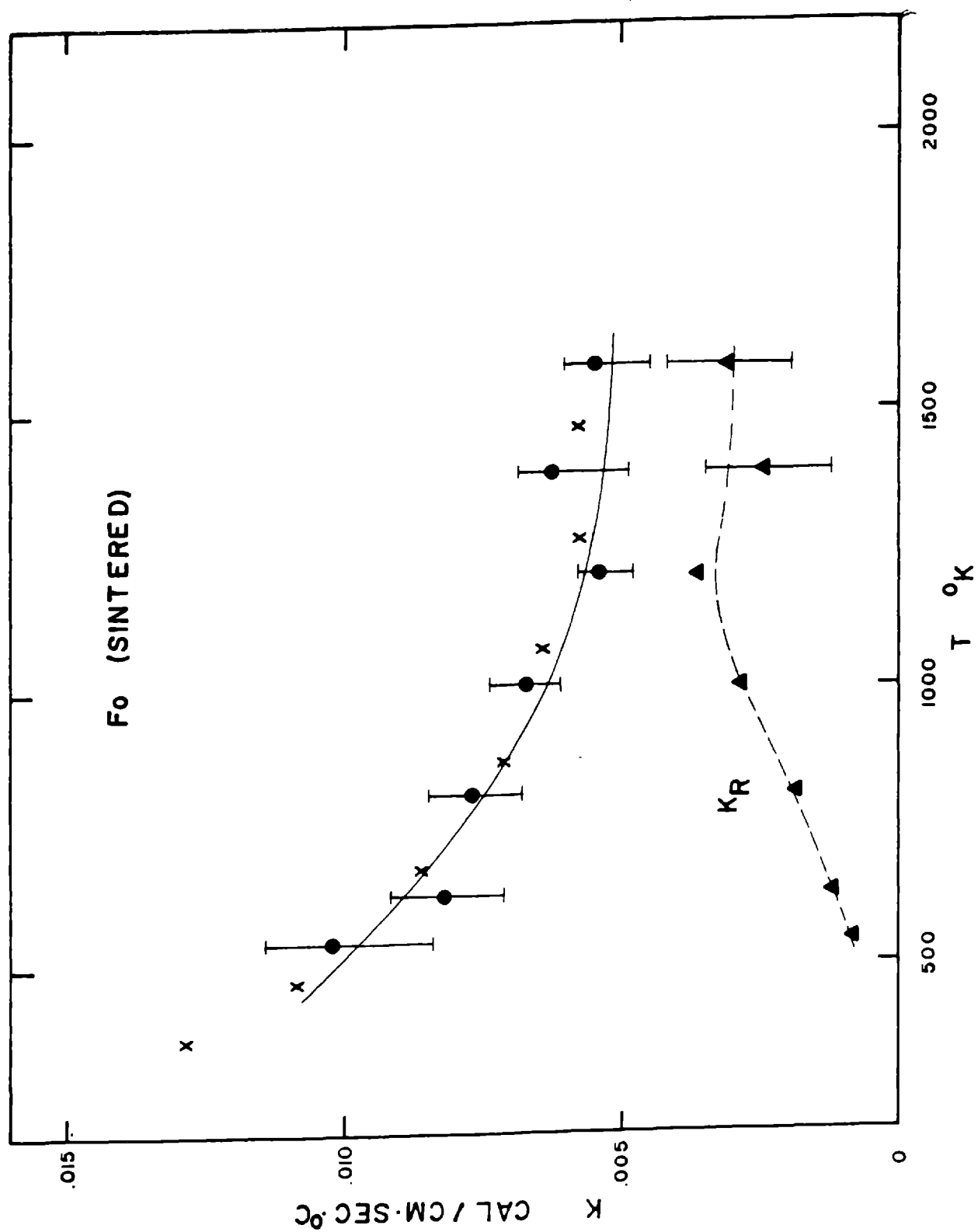


Table 6.5 Description of sample, olivine
 $\text{Fo}_{86}\text{Fa}_{14}$, single crystal.

| Property | Value | Comment |
|------------------|--------------------------------|---------------------------|
| Density | 3.39 g/cm ³ | picnometer |
| Refractive index | 1.68 | estimate from composition |
| Composition | $\text{Fo}_{86}\text{Fa}_{14}$ | estimate from density |
| Thickness | 0.620 cm | |
| Mean diameter | 1 cm | irregular circle |
| Orientation | within 10° of {010} | x-ray |

Appearance

before heating medium green, some crystal
 imperfections

after heating slightly darker green, with perhaps
 some brownish-yellow, but no
 drastic change.

Specific heat ^a $.239 + .056 \times 10^{-3}T - .006/(T \times 10^{-3})^2$ cal/g°C

^aas given by [Orr, 1953] .

Table 6.6 Results for olivine $\text{Fo}_{86}\text{Fa}_{14}$, single crystal, range of good solutions at 90% confidence interval.

| Temperature $^{\circ}\text{K}$ | κ_L cm^2/sec | $1/\bar{\epsilon}$ cm | K cal/cm sec $^{\circ}\text{C}$ |
|--------------------------------|-------------------------------------|-----------------------|---------------------------------|
| 565 | .0089 ^c | .62 | .0098 |
| 650 | .0077 ^c | .51 | .0095 |
| 745 | .0067 ^c | .38 | .0092 |
| 835 | .0060 ^c | .32 | .0093 |
| 930 | .0044-.0069 | .232-.262 | .0079-.0108 |
| 1020 | .0040-.0056 | .190-.198 | .0079-.0096 |
| 1205 | .0032-.0041 | .123-.125 | .0076-.0084 |
| 1402 | .0036-.0070 | .043-.077 | .0081-.0098 |
| 1600 | .0020-.0048 | .043-.066 | .0075-.0088 |
| 1208 ^a | .0030-.0043 | .121-.124 | .0073-.0086 |
| 1700 | .0012-.0058 | .033-.067 | .0079-.0099 |
| 1850 | .0001-.0054 | .031-.065 | .0082-.0101 |
| 1205 ^b | .0033-.0046 | .119-.125 | .0076-.0088 |
| 730 ^b | .0068 ^c | .42 | .0093 |

^a cycled temperature point to check reproducibility.

^b descending temperature points to check reproducibility.

^c These values are estimates used to compute $1/\bar{\epsilon}$.

The sample is too transparent for the method to be sensitive to both κ_L and $\bar{\epsilon}$. The error analysis is not meaningful for these points.

Figure 6.5 Photon mean free path in olivine single crystal, $\text{Fo}_{86}\text{Fa}_{14}$. The open circle is a point measured at descending temperature, and the x's are data of Fukao et al. [1968]. Solutions below 900 °K are obtained using assumed values of κ_L . The olivine composition of Fukao's crystal is $\text{Fo}_{88}\text{Fa}_{12}$.

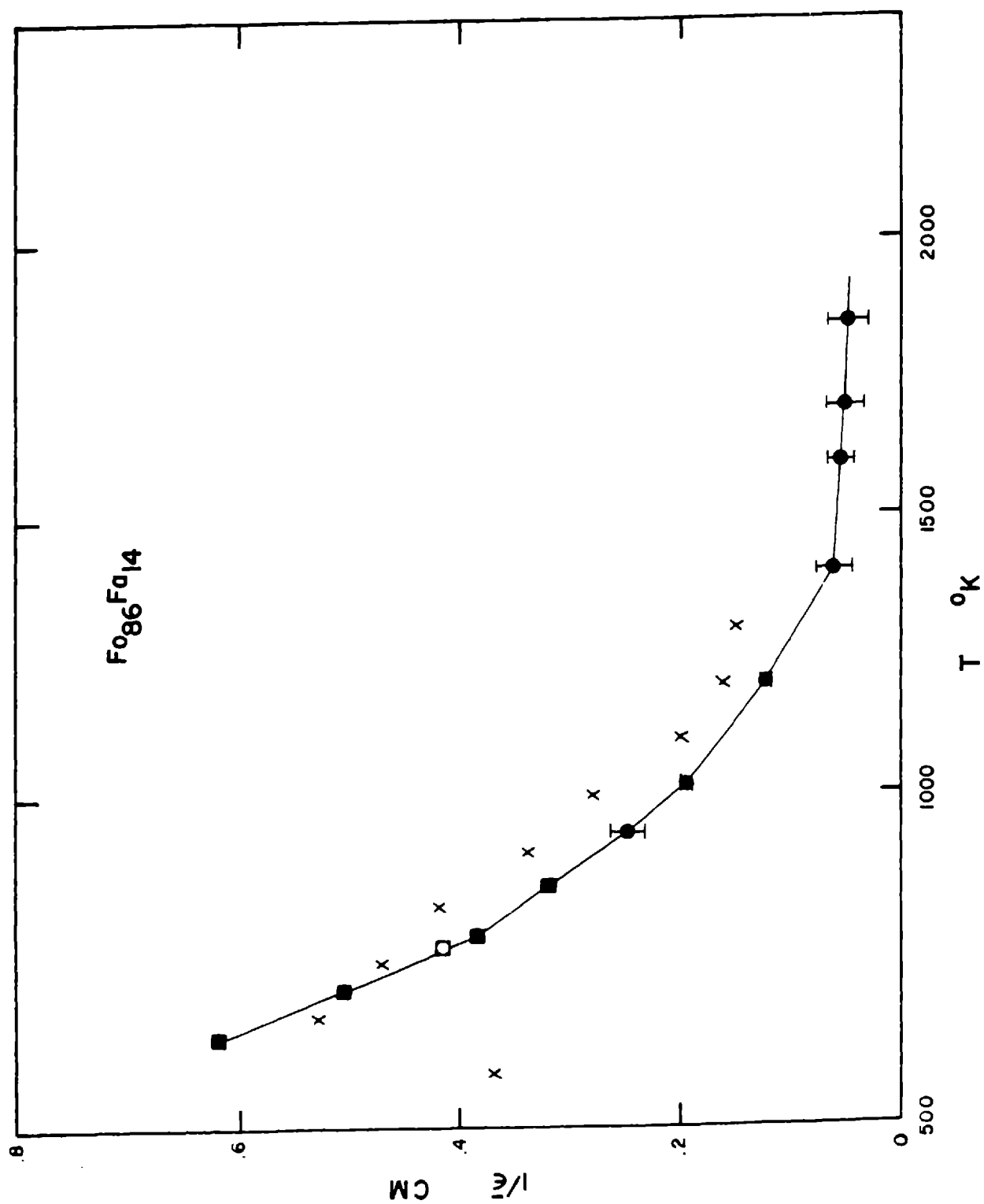


Figure 6.6 Total and radiative thermal conductivities in olivine single crystal, $\text{Fo}_{86}\text{Fa}_{14}$. Open circles are points measured at descending temperature. Solutions below 900 °K are obtained using assumed values of κ_L .

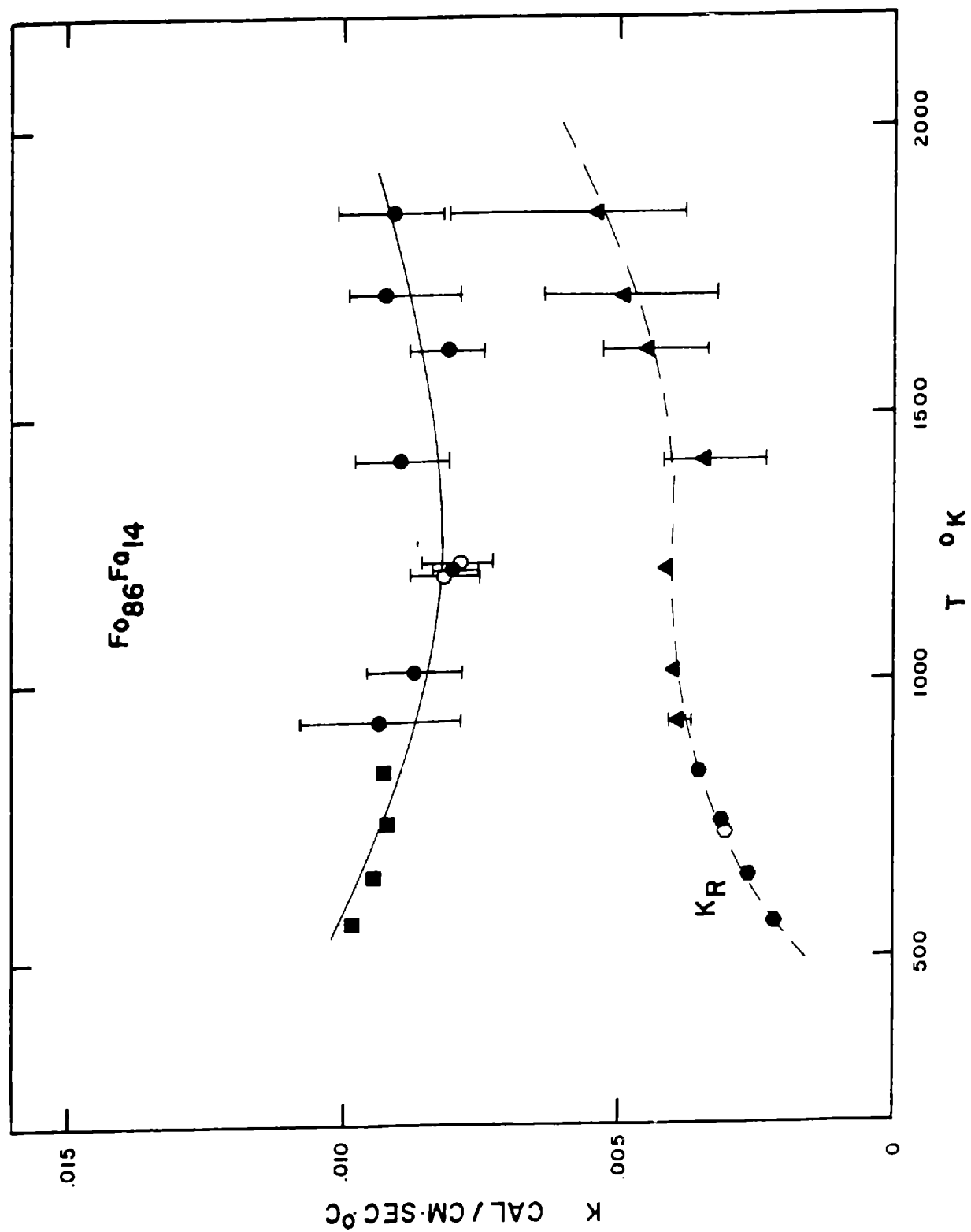


Table 6.7 Description of sample, olivine
 $\text{Fo}_{92}\text{Fa}_8$, single crystal.

| Property | Value | Comment |
|------------------|--|--|
| Density | 3.31 g/cm ³ | Picnometer |
| Refractive index | 1.67 | estimate from composition |
| Composition | SiO_2 41.09 wt% Al_2O_3 .00 FeO 7.92 MgO 49.85 CaO .03 NiO .39 | Microprobe analysis, (Dr. Arch Reid, NASA, MSC, Houston) |
| Thickness | 0.558 cm | |
| Mean Diameter | 1½ - 2 cm | teardrop shaped (cut gem) |
| Orientation | within 10° of {010} | x-ray |
| Appearance | | |
| before heating | light green, very good crystal, some parallel trains of small platy oriented inclusions | |
| after heating | slightly deeper green, but no brown or red, a few surface pits. | |

Specific heat^a $.245 + .052 \times 10^{-3}T - .006/(T \times 10^{-3})^2 \text{ cal/g}^\circ\text{C}$

^aas given by [Orr, 1953].

Table 6.8 Results for olivine $\text{Fo}_{92}\text{Fa}_8$, single crystal, range of good solutions at 90% confidence interval.

| Temperature $^{\circ}\text{K}$ | κ_L cm^2/sec | $1/\bar{\epsilon}$ cm | K cal/cm sec $^{\circ}\text{C}$ |
|--------------------------------|-------------------------------------|-----------------------|---------------------------------|
| 530 | .0132 ^b | 1.5 | .016 |
| 635 | .0110 ^b | .95 | .0144 |
| 735 | .0095 ^b | .62 | .0133 |
| 825 | .0085 ^b | .47 | .0130 |
| 923 | .0076 ^b | .35 | .0125 |
| 1026 | .0068 ^b | .275 | .0123 |
| 1120 | .0048-.0081 | .219-.231 | .0107-.0143 |
| 1215 | .0035-.0053 | .180-.186 | .0098-.0118 |
| 1310 | .0041-.0071 | .136-.148 | .0106-.0132 |
| 1406 | .0033-.0089 | .092-.124 | .0101-.0142 |
| 1503 | .0033-.0068 | .080-.106 | .0105-.0125 |
| 1600 | .0036-.0071 | .051-.1079 | .0101-.0117 |
| 1750 | .0001-.0067 | .039-.085 | .0090-.0114 |
| 1850 | .0001-.0072 | .035-.081 | .0100-.0129 |
| 1900 | .0001-.0052 | .039-.071 | .0090-.0111 |
| 1200 ^a | .0051-.0089 | .190-.200 | .0116-.0153 |

^a descending temperature point to check reproducibility.

^b see note c, Table 6.6.

Figure 6.7 Photon mean free path in olivine single crystal, $\text{Fo}_{92}\text{Fa}_8$. The open circle is a point measured at descending temperature and the x's are data of Fukao et al. [1968]. Solutions below 1100 °K are obtained using assumed values of κ_L . The olivine composition of Fukao's crystal is $\text{Fo}_{88}\text{Fa}_{12}$.

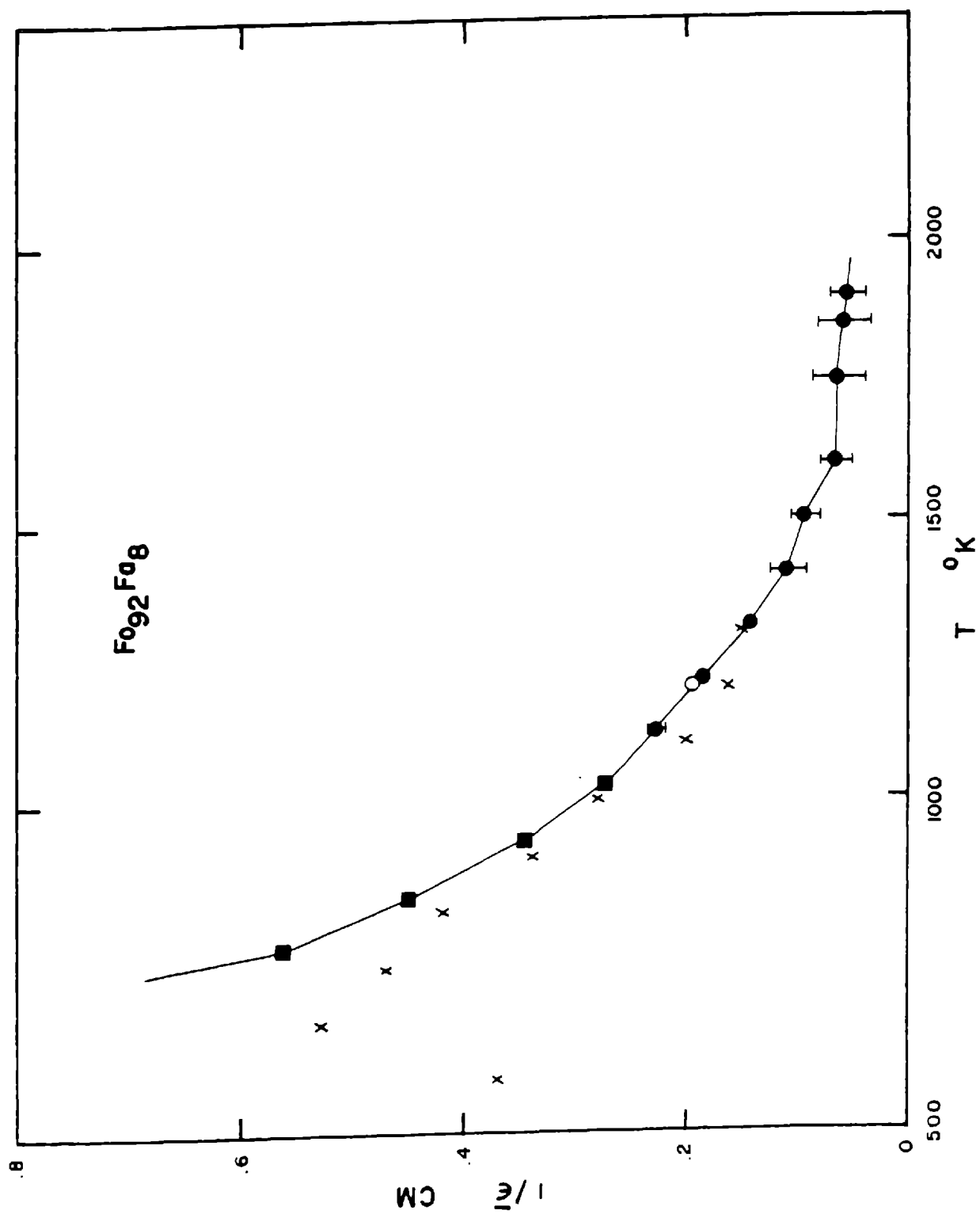


Figure 6.8 Total and radiative thermal conductivities in olivine single crystal $\text{Fo}_{92}\text{Fa}_8$. Open circles are points measured at descending temperature. Solutions below 1100 °K are obtained using assumed values of κ_L .

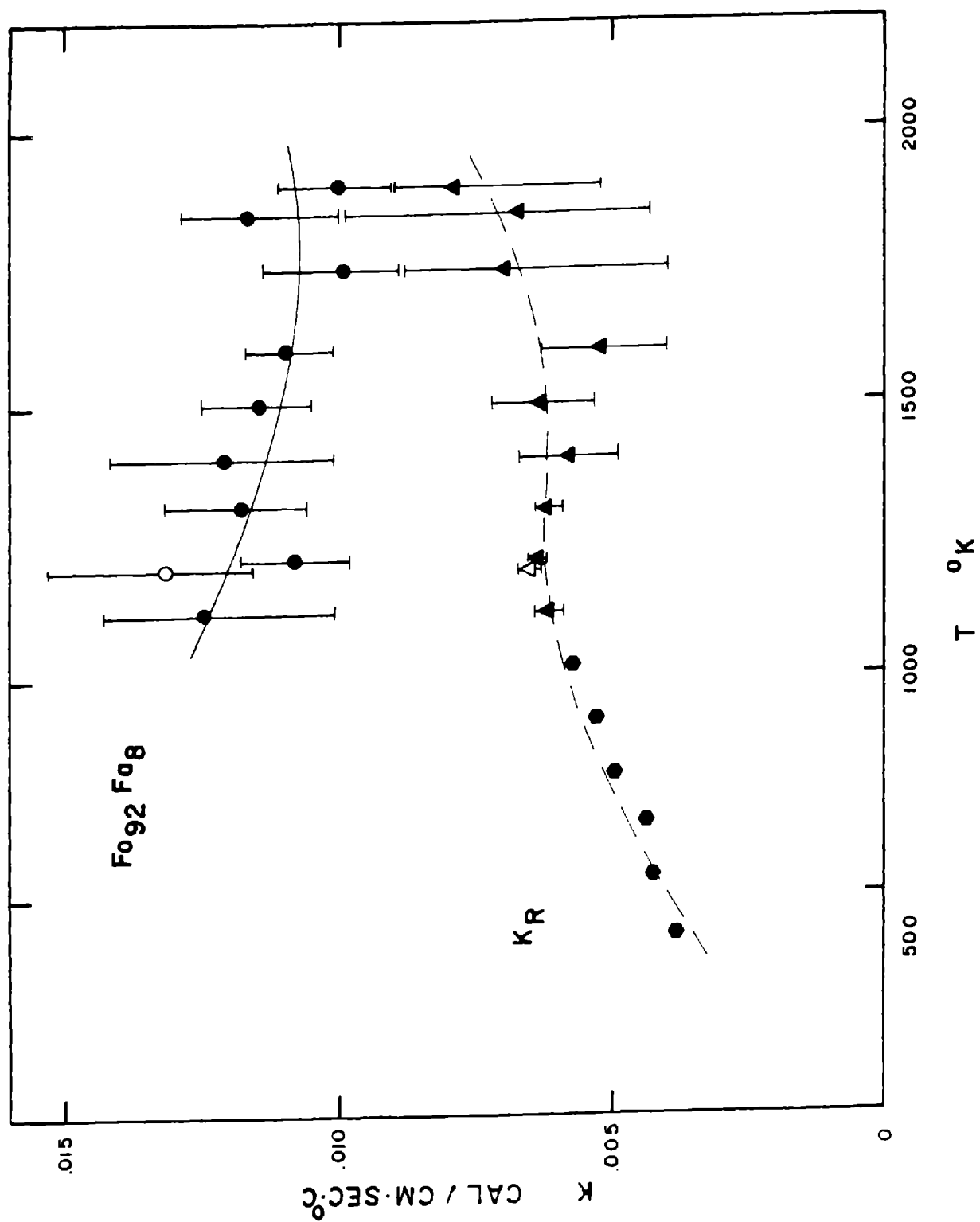


Table 6.9 Description of sample, dunite, twin sisters,
 $\text{Fo}_{95}\text{Fa}_5$.

| Property | Value | Comment |
|---|--|---------------------------|
| Density | 3.25 g/cm ³ | picnometer |
| Refractive index | 1.66 | estimate from composition |
| Grain size | 1-2 mm | |
| Composition | olivine 98.5 vol.% | |
| | ore (chromite?) 1.3 | thin section |
| | serpentine 0.2 | |
| Thickness | 1.030 cm | |
| Diameter | 3½ cm | circular |
| Appearance | | |
| before heating | medium to dark green rock, highly variable grain size. | |
| after heating | <u>all</u> intergranular surfaces reddish colored. entire sample red-brown, but interior of grains still clear | |
| <u>Specific heat^a .250 + .050 x 10⁻³T - .006/(Tx10⁻³)² cal g/°C</u> | | |
| ^a as given by [Orr, 1953]. | | |

Table 6.10 Results for dunite, twin sisters $\text{Fo}_{95}\text{Fa}_5$,
range of good solutions at 90% confidence interval.

| Temperature $^{\circ}\text{K}$ | κ_L cm^2/sec | $1/\bar{\epsilon}$ cm | K cal/cm sec $^{\circ}\text{C}$ |
|--------------------------------|-------------------------------------|-----------------------|---------------------------------|
| 554 | .0091-.0102 | .086-.103 | .0079-.0089 |
| 650 | .0085-.0090 | .075-.088 | .0078-.0083 |
| 747 | .0077-.0079 | .058-.065 | .0074-.0076 |
| 843 | .0068-.0072 | .051-.058 | .0068-.0072 |
| 933 | .0058-.0065 | .041-.061 | .0064-.0068 |
| 1022 | .0053-.0054 | .043 | .0060-.0061 |
| 1200 | .0043-.0046 | .030-.040 | .0054-.0056 |
| 1024a | .0046-.0055 | .029-.047 | .0054-.0059 |

a descending temperature point to check reproducibility.

Figure 6.9 Photon mean free path in twin sisters dunite, $\text{Fo}_{95}\text{Fa}_5$. Dotted line is for a hypothetical material without oxidation effect.

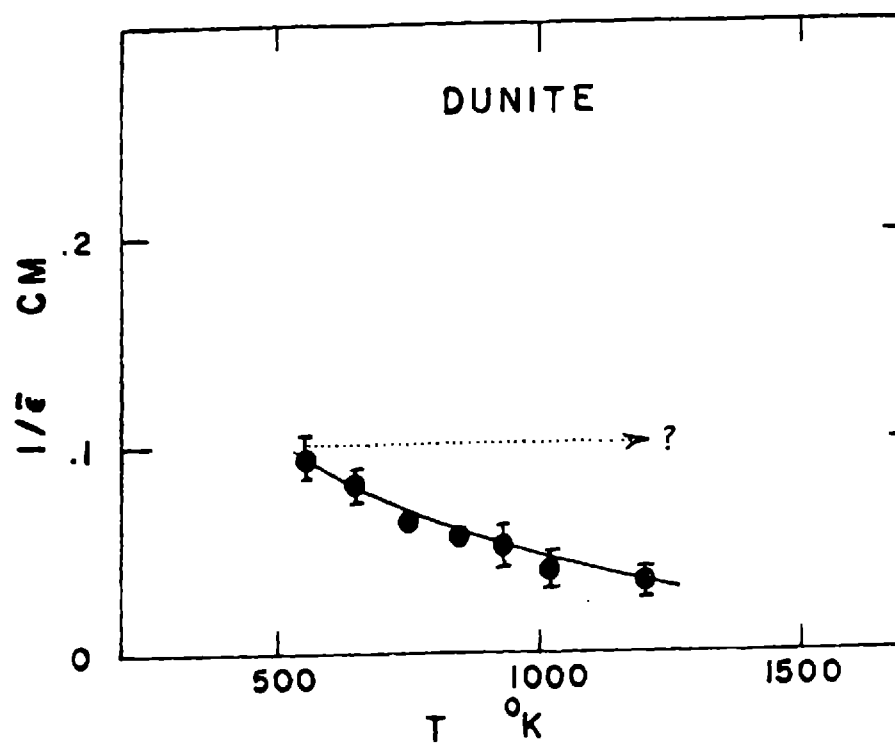


Figure 6.10 Total and radiative thermal conductivities in twin sisters dunite, $\text{Fo}_{95}\text{Fa}_5$. Dotted lines are for a hypothetical material without oxidation effect.

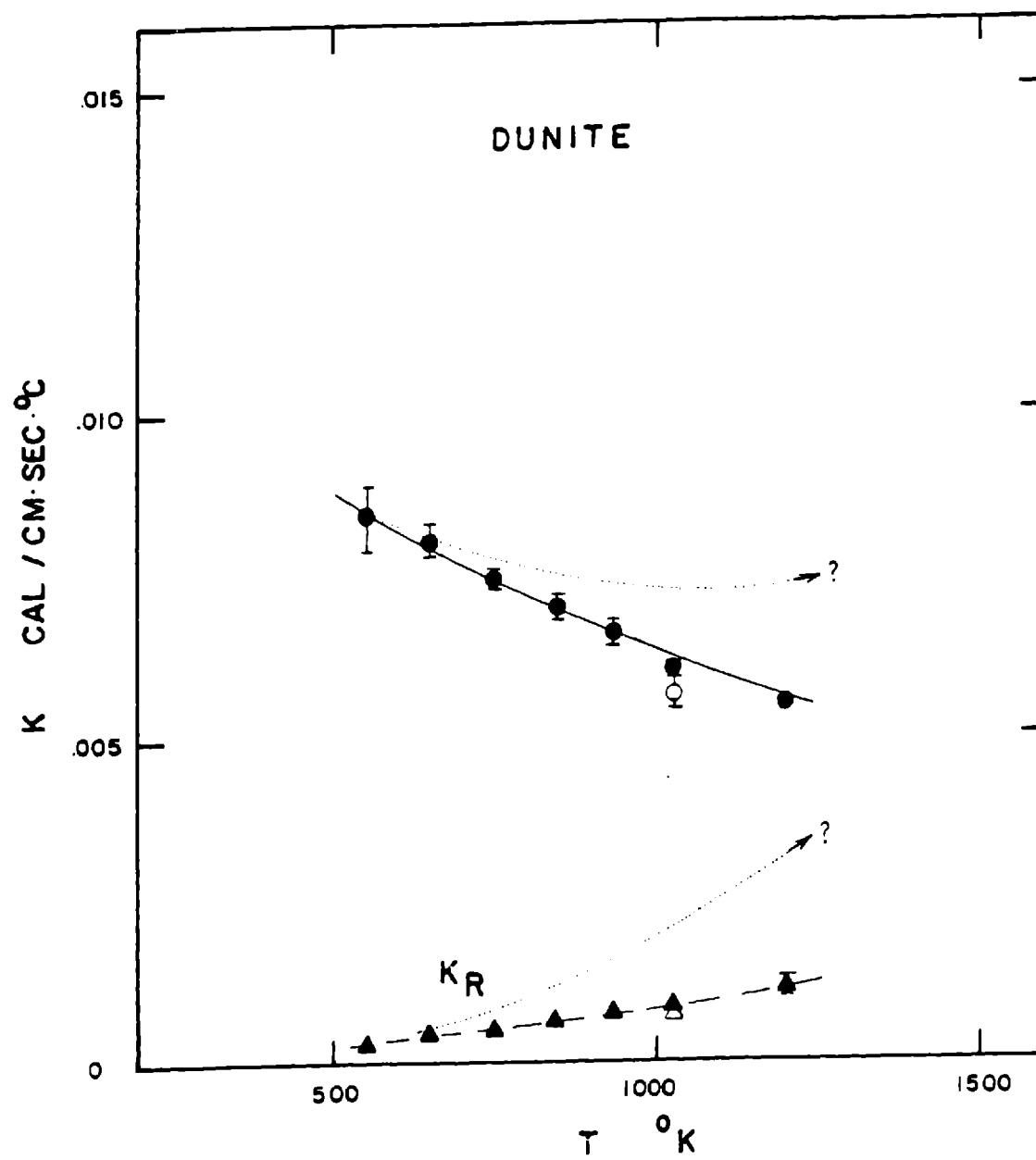


Table 6.11 Description of sample, enstatite
 $\text{En}_{90}\text{Fs}_{10}$, single crystal.

| Property | Value | Comment |
|--|--|---------------------------|
| Density | 3.32 g/cm ³ | picnometer |
| Refractive index | 1.68 | estimate from composition |
| Composition | En ₉₀ Fs ₁₀ | estimate from density |
| Thickness | 0.558 cm | |
| Mean Diameter | 1 cm | irregular rectangle |
| Appearance | | |
| before heating | dark transparent brown with some imperfections | |
| after heating | same, but somewhat deeper brown | |
| <u>Specific heat^a.232 + .080 x 10⁻³T - .006/(Tx10⁻³)²cal/g°C</u> | | |
| ^a as given by [Goranson, 1942]. | | |

Table 6.12 Results for enstatite $\text{En}_{90}\text{Fs}_{10}$, single crystal, range of good solutions at 90% confidence interval.

| Temperature $^{\circ}\text{K}$ | κ_L cm^2/sec | $1/\bar{\epsilon}$ cm | K cal/cm sec $^{\circ}\text{C}$ |
|--------------------------------|-------------------------------------|-----------------------|---------------------------------|
| 600 | .0110-.0134 | .062-.092 | .0100-.0120 |
| 756 | .0063-.0068 | .062-.068 | .0065-.0069 |
| 934 | .0057-.0058 | .041 | .0064-.0065 |
| 1025 | .0056-.0057 | .034-.036 | .0065-.0066 |
| 1218 | .0047 | .026 | .0060 |
| 1315 | .0040 | .025 | .0055 |
| 1405 | .0040-.0042 | .023-.024 | .0058-.0068 |
| 1503 | .0042 | .027 | .0067 |
| 1600 | .0040-.0044 | .022-.027 | .0068-.0071 |
| 1127 ^a | .0047 | .034 | .0059 |

^a a descending temperature point to check reproducibility.

Figure 6.11 Photon mean free path in enstatite, $\text{En}_{90}\text{Fs}_{10}$. The open circle is a point measured at descending temperature.

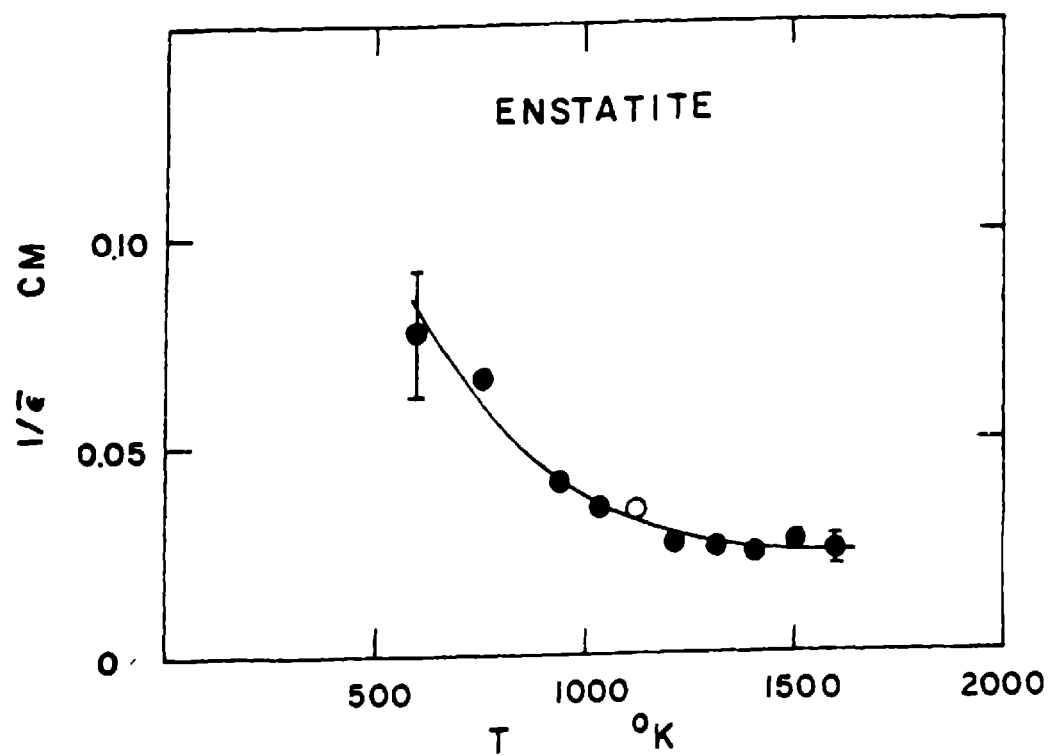
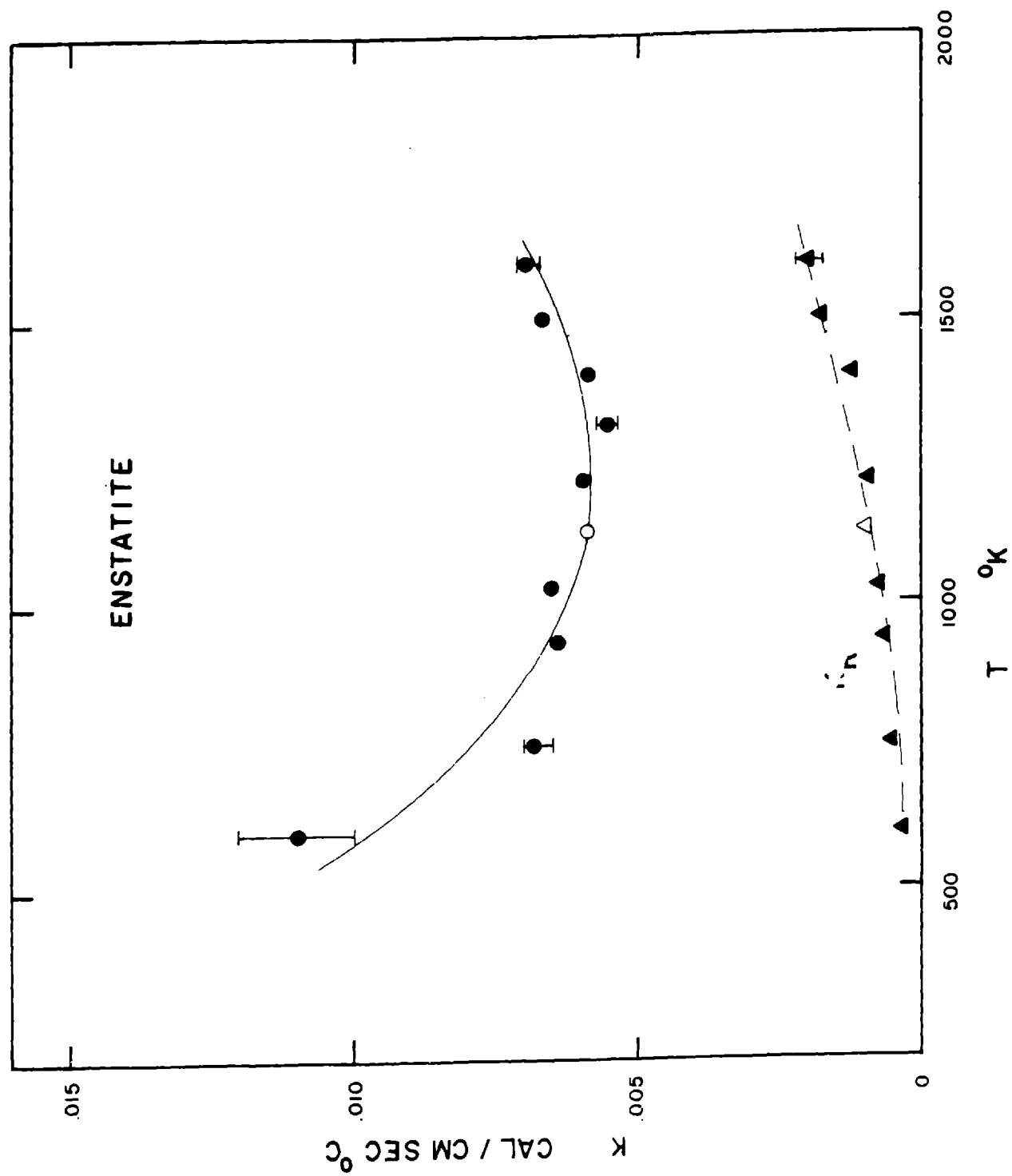


Figure 6.12 Total and radiative thermal
conductivities in enstatite $\text{En}_{90}\text{Fs}_{10}$.
Open circles are points measured at
descending temperature.



Discussion

The measurement of sintered aluminum oxide is intended primarily as a verification of the effectiveness of this technique. Sample description and results are given in Tables 6.1 and 6.2 and in Figures 6.1 and 6.2. The present total conductivity values agree well with the values for similar material of Lee and Kingery [1960]. Furthermore, our photon mean free path results follow a curve approximately proportional to Lee and Kingery's, though they have different values. However, we can account for this difference by using the $\cong 1\%$ porosity of our material (instead of their 0.25%) to calculate the scattering coefficient from equation (3.14). The photon mean free path in our material is typical of that in a strongly scattering porous medium. In such a medium, the decreasing wavelength of radiation associated with increasing temperature leads to greater radiation-pore interaction. Thus, scattering increases with temperature.

For sintered forsterite, the results are again typical of a strongly scattering material. Sample description and results are given in Tables 6.3 and 6.4 and in Figures 6.3 and 6.4. Agreement with the total thermal conductivity measurements of Kingery et al. [1954] is very good. The photon mean free path falls off somewhat more rapidly at high temperatures than one

would expect from pure scattering. This phenomenon is probably due to the effects of both scattering and absorption at high temperatures.

Sample description and results for an olivine ($\text{Fo}_{86}\text{Fa}_{14}$) single crystal are given in Tables 6.5 and 6.6 and in Figures 6.5 and 6.6. The photon mean free path values are similar to, but slightly less than those of Fukao et al. [1968] and Aronson et al. [1968]. This difference is probably caused by the greater iron content and the resulting increase of infrared absorption in the present specimen as compared to those of the previous experiments. At the highest temperatures, the mean free path has a value such that K_L and K_R are about equal. Only above about 2000 °K (which is beyond the range of this experiment), would the radiative conductivity, if extrapolated, begin to dominate.

Sample description and results for an olivine ($\text{Fo}_{92}\text{Fa}_8$) single crystal are given in Tables 6.7 and 6.8 and in Figure 6.7 and 6.8. The photon mean free path values again are similar to, but this time slightly greater than the results of Fukao et al. [1968] and Aronson et al. [1968]. This difference is due to the lower iron content of this specimen as compared to any of the previous specimens. As the temperature is increased to 1900 °K, the mean free path decreases; nevertheless, it is large enough in this crystal to cause K_R to dominate over K_L at all temperatures above

1200 °K.

The radiative conductivity in twin sisters dunite is rather low, even though the crystal grains are large and transparent (to the eye). Sample description and results are given in Tables 6.9 and 6.10 and in Figures 6.9 and 6.10. Apparently, a great deal of extinction is caused by absorption and scattering at the grain boundaries. However, the theoretical result of Aronson et al. [1967a], as shown by equation (3.13), negates the possibility that scattering alone completely accounts for the extra extinction. Thus, the extra extinction must be due in part to absorption. Unfortunately, most of the grain surfaces in this sample became red-brown in color before the conclusion of the experiment. This irreversible coloring of the grain surfaces is likely due to the breakdown of small amounts of serpentine and other impurities. Probably the results are not characteristic of this material under less oxidizing or more pure conditions. Without oxidation, one might surmise that a hypothetical dunite sample would have a photon mean free path that remains approximately constant near to its low-temperature value until about 1400 °K. Then, the bulk absorption, demonstrated by single crystals with similar olivine composition, begins to dominate. Curves for this hypothetical dunite are shown also in Figures 6.9 and 6.10.

The photon mean free path in enstatite is lower by

at least a factor of two over most of the temperature range, than in an olivine of comparable Fe/Mg ratio. As a result, K_R does not increase much with temperature, and little or no increase is observed in total conductivity. Sample description and results are given in Tables 6.11 and 6.12 and in Figures 6.11 and 6.12. This result is consistent with spectroscopic observations of the pyroxene structure made by Burns [1970] and White and Keester [1966] in which an absorption band not present in olivine is found at 1.9μ . This band probably blocks much of the near-infrared radiation that would otherwise contribute to K_R .

Thermal Conductivity of Mantle Olivine

The photon mean free paths and lattice thermal conductivities in the four olivine materials investigated here are summarized in Figure 6.13 and 6.14. Also shown are curves for a hypothetical mantle olivine with composition $Fe_{90}Fa_{10}$. This mantle olivine has the same infra-red spectral properties as the hypothetical dunite described above. Grain boundary absorption and scattering together limit the photon mean free path to a value not greater than 0.1 cm from 500 °K to 1400 °K. However, above 1400 °K the material acts spectrally as a single crystal. (The limitation at the middle temperatures could also be caused by the addition of some enstatite, which is more opaque than olivine, to the material.) The lattice conductivity of the

Figure 6.13 Summary of photon mean free path as a function of temperature in olivines, including hypothetical mantle material.

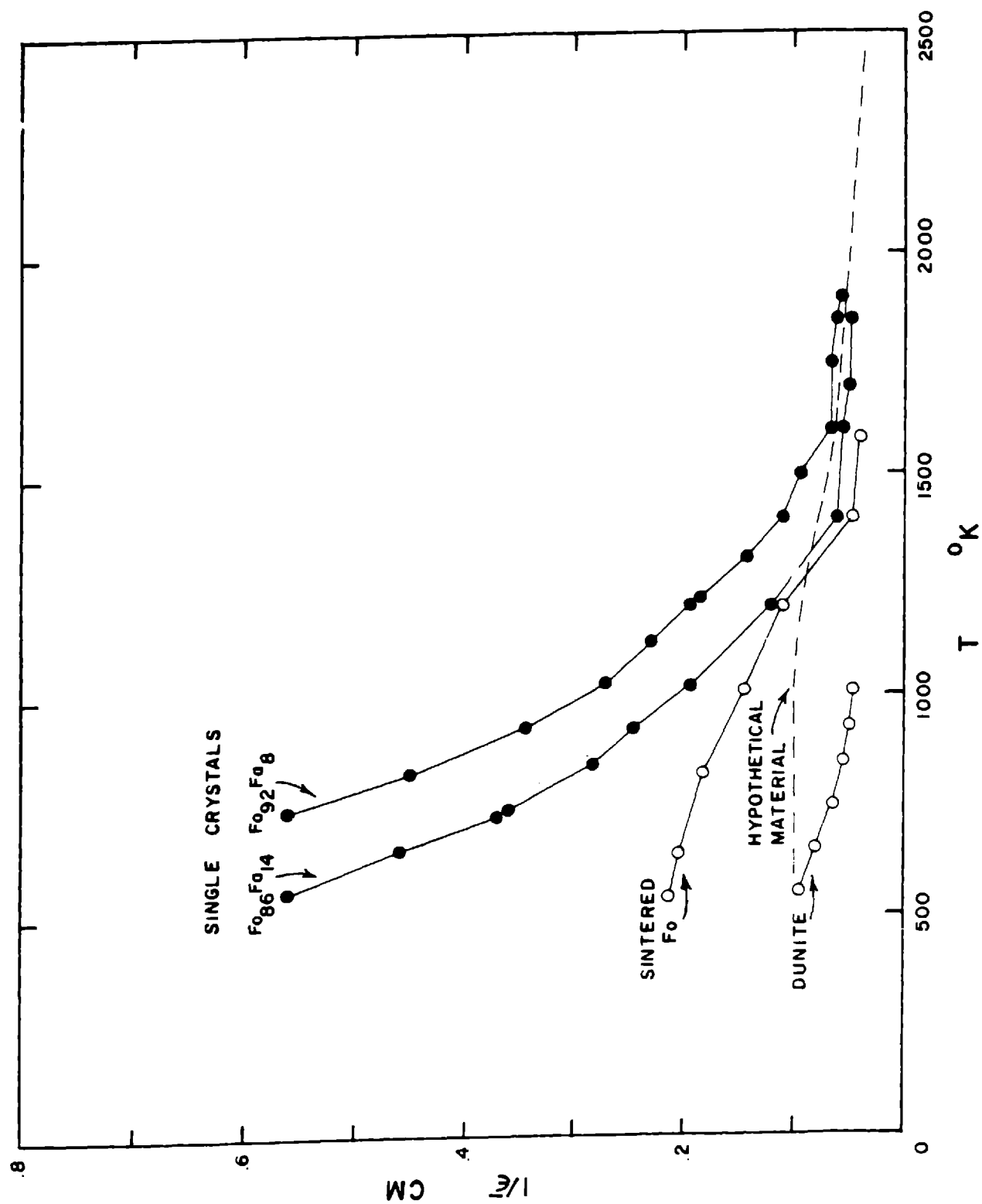
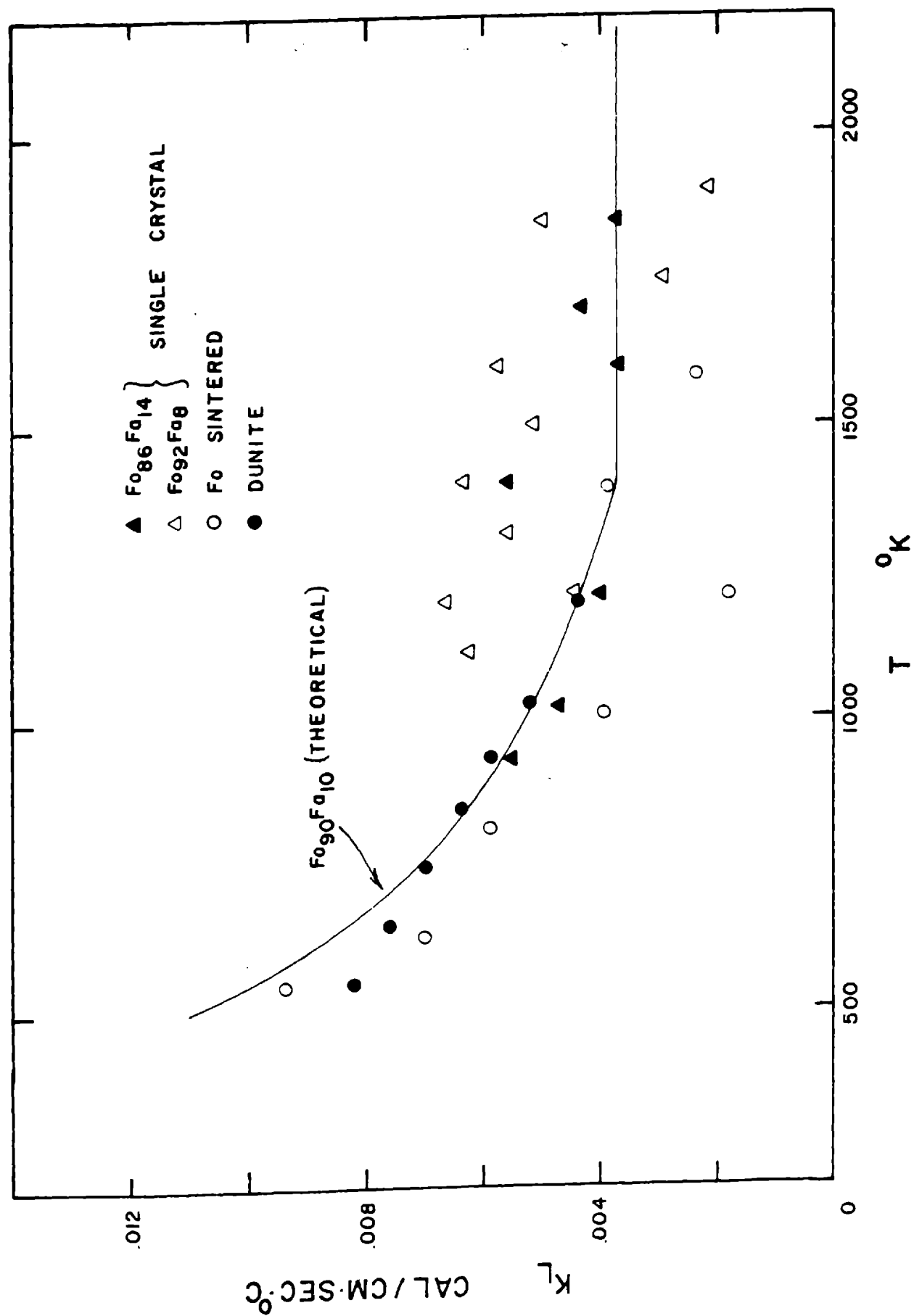


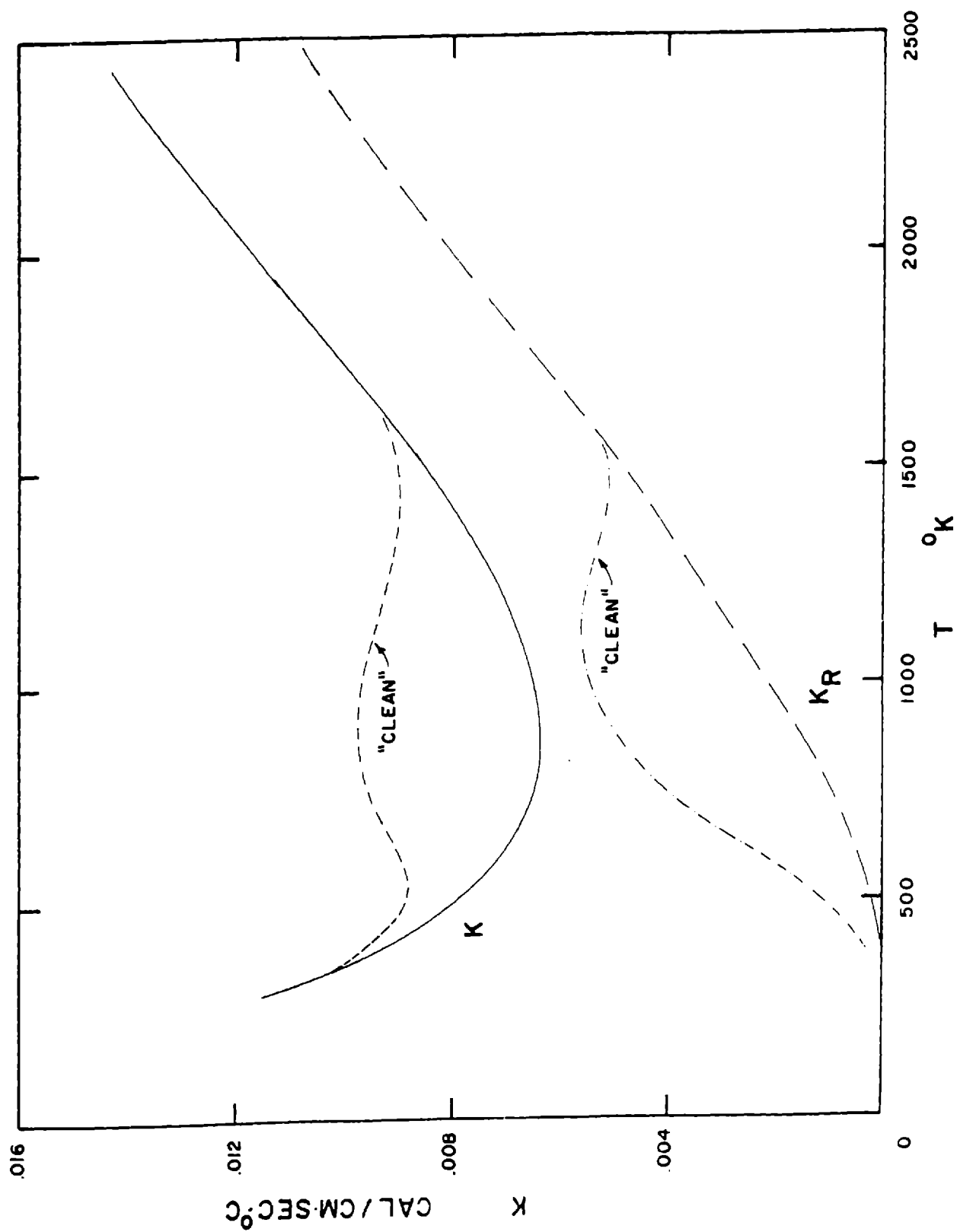
Figure 6.14 Summary of lattice thermal conductivity as a function of temperature in olivines, including hypothetical mantle material.



hypothetical material reaches its lower limit at 1200 °K, as suggested by the data shown in Figure 6.14.

The hypothetical mantle material has total and radiative conductivities shown as functions of temperature in Figure 6.15. The most important characteristics of the total conductivity are an initial decrease due to the T^{-1} dependence of lattice conductivity, and then a slow, almost linear increase due to the increase of the radiative component. If the hypothesized grain boundary extinction in the range 500 °K to 1400 °K did not occur, i.e. if the material were "clean", then the conductivity in this temperature range would be somewhat higher, as shown in Figure 6.15. But, because the upper mantle is probably not composed entirely of clear crystals, the lesser conductivity values are preferred. Above 1400 °K, the hypothetical material acts in every respect as a single crystal with olivine composition $\text{Fo}_{90}\text{Fa}_{10}$. Its total conductivity increases slowly, but remains less than its room temperature value of .011 cal/cm sec °C until above 2000 °K.

Figure 6.15 Total and radiative conductivities of hypothetical mantle material as functions of temperature. Curves labeled "clean" are for material without grain boundary absorption and scattering.



7. GEOPHYSICAL APPLICATIONS

In applying the results of this investigation to the earth, we assume the following thermal conductivities:

- (1) The lattice conductivity is given by the larger of

$$K_L = \frac{1}{30.6 + .21T}$$

$$K_{Lmin} = .003 + 3 \times 10^{-6} z \quad (7.1)$$

where z is the depth in km and T is the temperature in $^{\circ}K$. Units are cal/cm sec $^{\circ}C$.

- (2) The radiative conductivity is given by

$$K_R = 0 \quad \text{for } T \leq 500^{\circ}K \quad (7.2)$$

and

$$K_R = 5.5 \times 10^{-6} (T - 500) \quad \text{for } T > 500^{\circ}K$$

Equations (7.1) produce the theoretical curve for K_L in olivine of composition $Fe_{90}Fa_{10}$, as shown in Figure 6.14. Equations (7.2) are a piecewise linear approximation to the curve for K_R in the same material, as shown in Figure 6.15. K_R is assumed to be pressure independent. The values of $K = K_L + K_R$ obtained from equations (7.1) and (7.2) fall within the range of our data at all experimental temperatures. The equations are assumed accurate at all

depths and temperatures where olivine is the stable phase. They are less dependable, though possibly still usable, after the olivine-spinel transition. However, they are at best only a first guess after the spinel-post spinel transition.

Thermal Conductivity and Temperature in the Upper Mantle

We use the thermal conductivity given by equations (7.1) and (7.2) to compute steady-state temperature and conductivity distributions in a continental and two oceanic upper mantle models. For purposes of comparison, some of the calculations are done twice, once using the above conductivity, and once using the conductivity used by MacDonald [1963],

$$K = .006 + \frac{16 \sigma T^3}{\bar{\epsilon}} \quad \text{cal/cm sec } ^\circ\text{C} \quad (7.3)$$

with $\bar{\epsilon} = 10 \text{ cm}^{-1}$.

The three upper mantle models we use are based on those of Sclater and Francheteau [1970]. The properties of the models are summarized in Table 7.1. The first model is for the mantle beneath a continental shield; the second and third are for the mantle beneath old ocean basins. The difference between the two ocean basin models is that one has a lithosphere which is essentially depleted of radioactive sources with respect to the other. The depleted oceanic model has about the

Table 7.1 Properties of models used in upper mantle
temperature calculations

| Model | Continental shield | Ocean basin depleted | Ocean basin non-depleted |
|---|------------------------|-------------------------|-----------------------------|
| surface heat flow cal/cm ² sec | 1.05x10 ⁻⁶ | 1.1x10 ⁻⁶ | 1.1x10 ⁻⁶ |
| conductivity of crust cal/cm sec °C | .006 | .006 | .006 |
| Heat production in crust cal/cm ³ sec | 1.44x10 ⁻¹³ | .6x10 ⁻¹³ | .6x10 ⁻¹³ |
| Depth to Moho km | 30 | 10 | 10 |
| Heat production in lithosphere cal/cm ³ sec | .02x10 ⁻¹³ | .02x10 ⁻¹³ | .33x10 ⁻¹³ |
| Depth to base of lithosphere km | 200 | 110 | 110 |
| Heat production in mantle cal/cm ³ sec | .1x10 ⁻¹³ | .1x10 ⁻¹³ | .1x10 ⁻¹³ |

same temperature at the base of its lithosphere as the continental model, while the non-depleted oceanic model has about the same heat flux at the base of its lithosphere as the continental model.

The conductivity results, shown in Figure 7.1, have two interesting features. The first is that the present conductivity is predominantly lower than the comparison conductivity in all models. The present conductivity is always less than twice the room temperature conductivity of olivine. The second interesting feature is the existence of fine structure in the conductivity of the upper 50 km, as shown in the inset of Figure 7.1. In the upper 50 km of the continental model, both the present conductivity and the comparison conductivity are essentially constant or slowly increasing. The same is true for the comparison conductivity in the oceanic models. However, the present conductivity is quite different in the oceanic models. As depth increases, it first increases rapidly at the Moho, but then immediately begins to decrease due to the T^{-1} dependence of lattice conductivity. A minimum is reached at about 40 km, followed by the final, gradual increase. The present investigation indicates that the thermal conductivity is possibly as much as 30% higher immediately under the oceanic Moho than under the continental Moho.

The temperature results, given in Figure 7.2, show the effect of the lower present conductivity: The mantle temperatures are higher for all models. In fact,

Figure 7.1 Thermal conductivity in the
upper mantle.

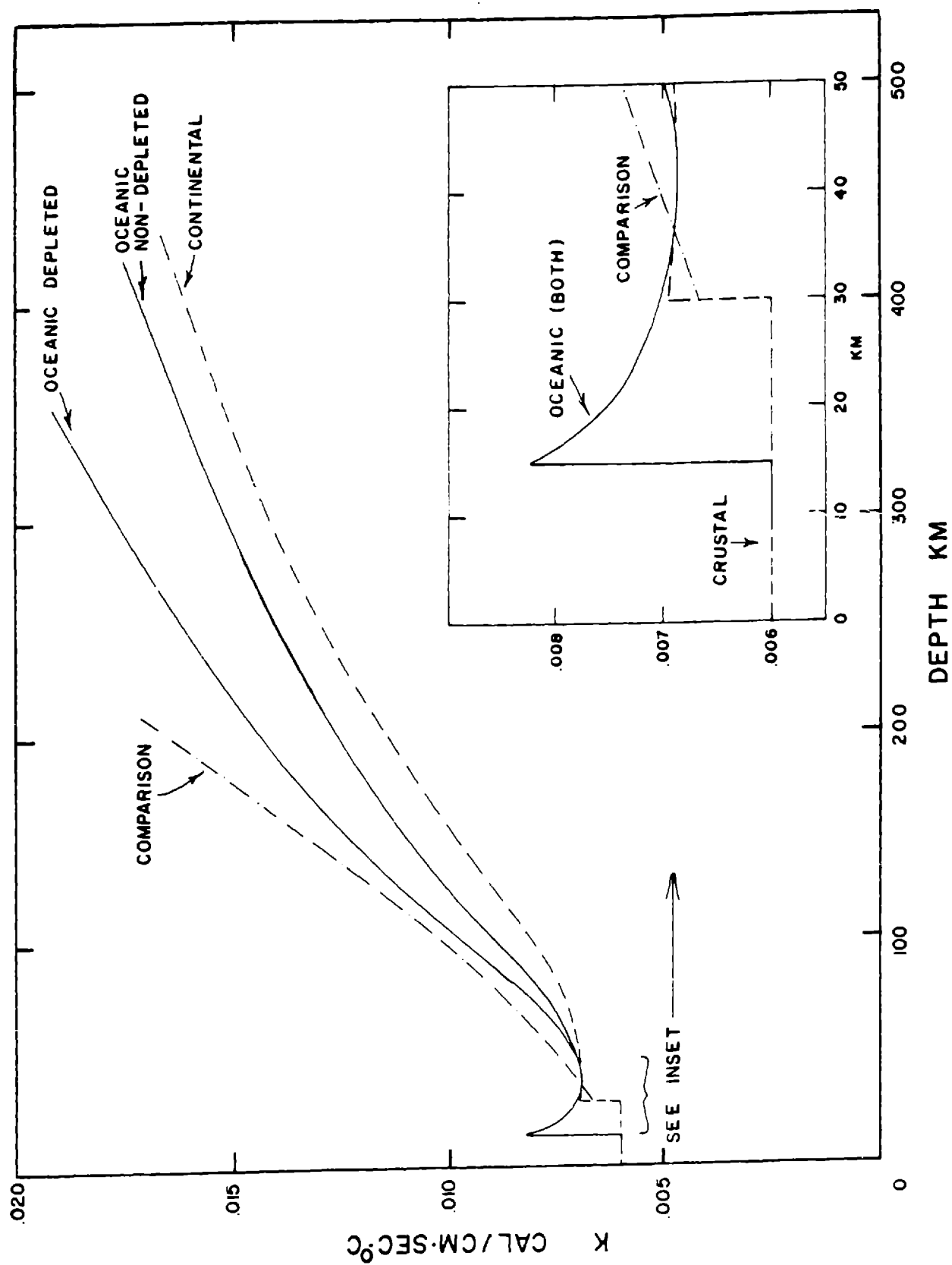
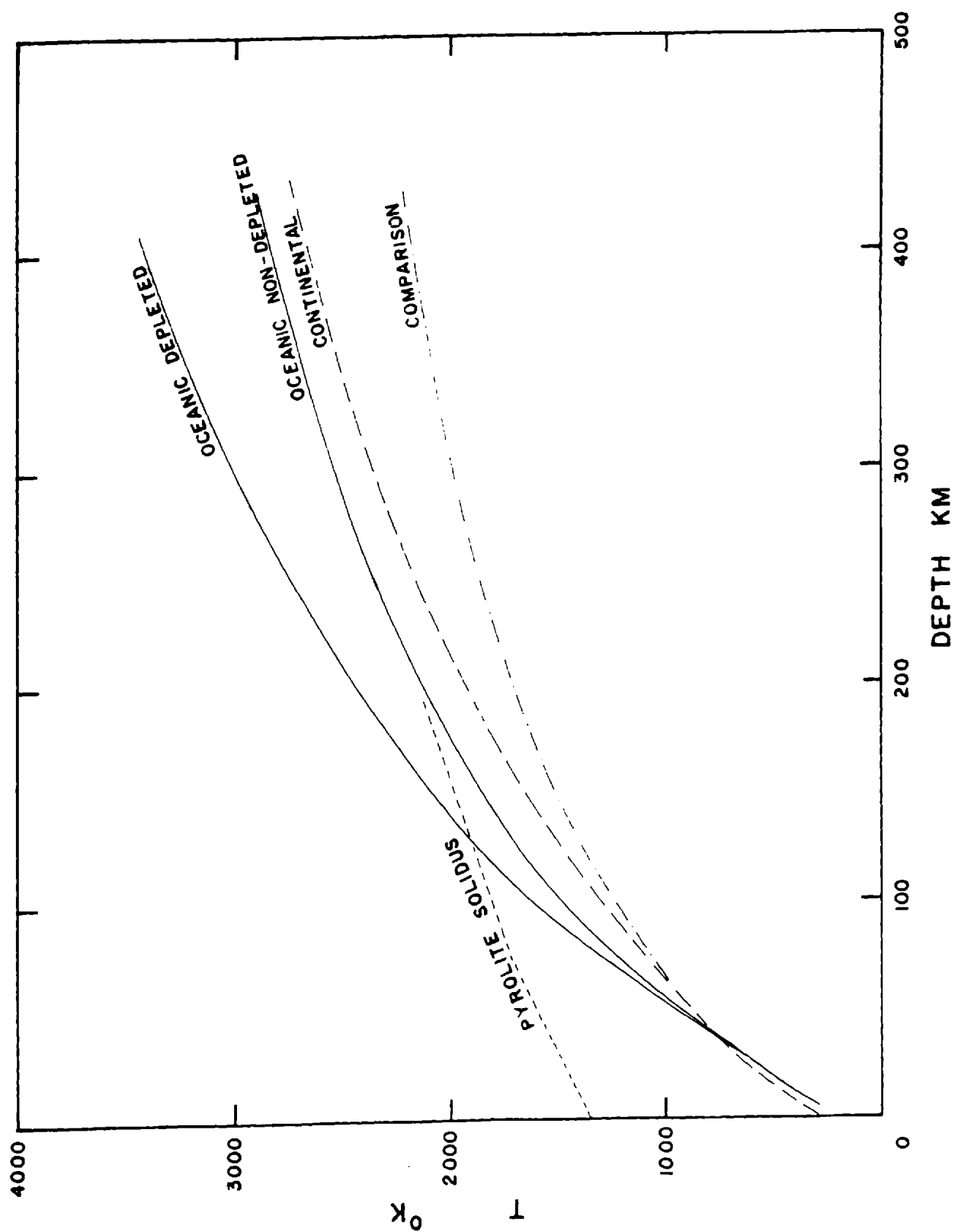


Figure 7.2 Temperature in the upper mantle. The pyrolite solidus is from Ringwood [1969].



the temperature in the depleted oceanic model rises rapidly enough to intersect Ringwood's pyrolite solidus at 130 km. To avoid large scale melting in this model, it would be necessary to invoke another mode of heat transfer, such as convection. The non-depleted oceanic geotherm reaches the pyrolite solidus more gradually and at grazing incidence. This result is in keeping with the notion of incipient melting at depths of 100 to 200 km.

Thermal Conductivity in the Moon

Sonett et al. [1971] find a temperature distribution in the moon based on an electrical conductivity profile obtained from their magnetometer data. This temperature, shown in Figure 7.3, may be used to infer the lunar thermal conductivity, (for an olivine moon) as shown in Figure 7.4. We have used the temperature-dependent conductivity of Figure 6.15, and have assumed a negligible pressure effect. The result is a nearly constant thermal conductivity at all depths, equal to about $.008 \pm .002$ cal/cm sec °C. For a material with grain boundary extinction, lattice conductivity dominates. Without grain boundary extinction, the lattice and radiative contributions are about equal.

Temperature Field of a Downgoing Slab

The temperature field of a downgoing slab has been computed using the thermal conductivity of equations (7.1)

Figure 7.3 Temperature in the moon
[Sonett et al., 1971].

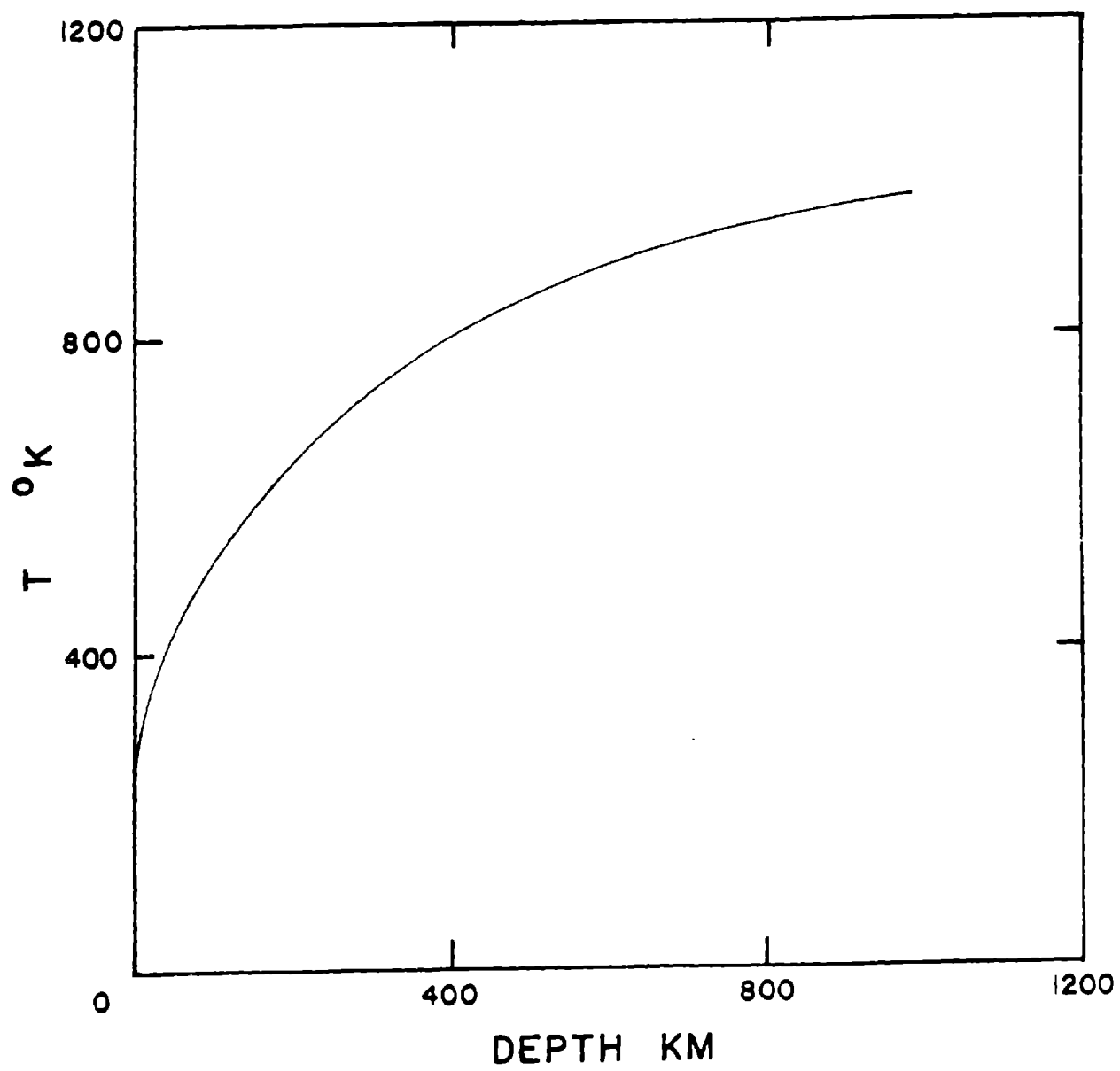
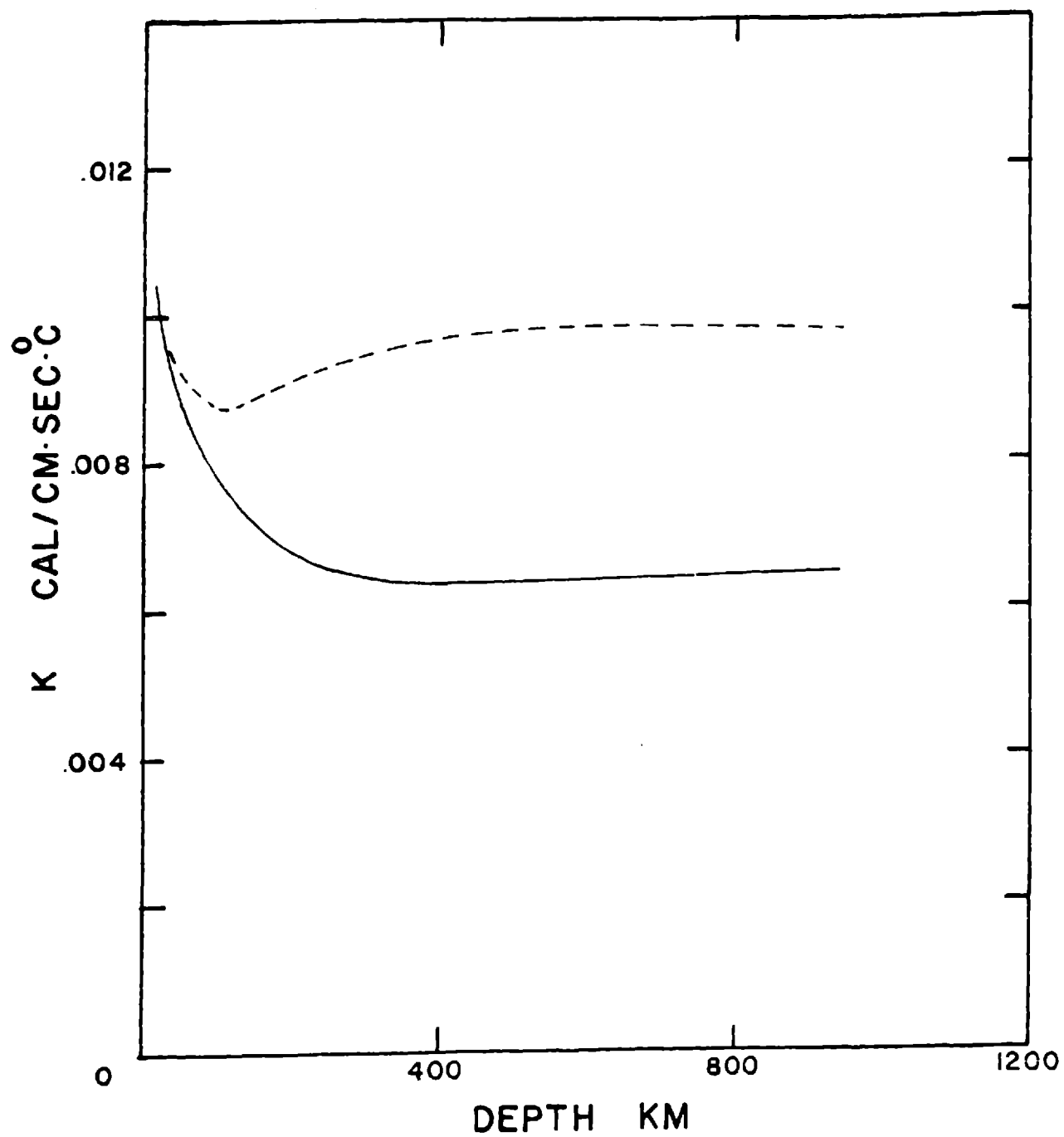
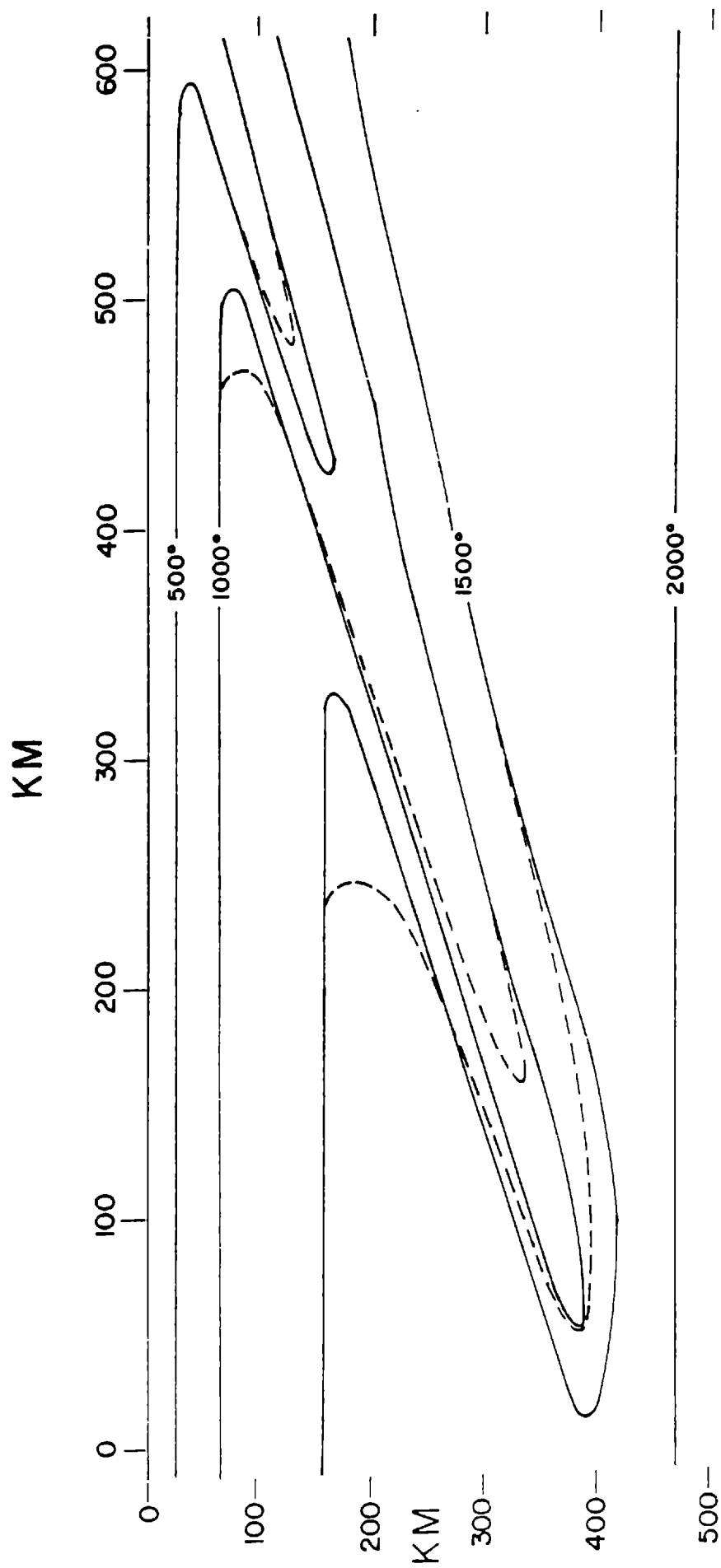


Figure 7.4 Thermal conductivity in the
moon.



and (7.2). The particular model chosen has a velocity of 8 cm/yr, descends at an angle of 45° , and includes all heating effects and phase changes. We have used N. Sleep's most recent version of the computer program developed for this problem by Minear and Toksöz [1970] and Toksöz et al. [1971]. The present results are compared to the original results in Figure 7.5 to show the effect of the new conductivity. Originally, the thermal conductivity was taken from MacDonald [1959]. It is similar to that given by equation (7.3). The major difference between the two conductivities is that the present is considerably smaller than the original at high temperatures. As a result, the slab remains cold further into the mantle, and temperature gradients are increased by as much as a factor of two at positions above and trailing the leading edge of the slab. This increased gradient implies a somewhat larger local stress and seismic effect than in the original model.

Figure 7.5 Temperature field of a down-going slab at $t = 9.45$ m.y. Slab thickness is 80 km, velocity is 8 cm/yr, and angle of descent is 45° . All heating and phase changes are included. The solid lines are for the present conductivity and the dashed lines are for the original. Temperatures are in $^\circ\text{C}$.



SUMMARY

In geophysically interesting materials, the dominant modes of heat transfer are lattice conduction and radiation. The lattice conductivity, K_L , decreases with temperature until a lower limit, K_{Lmin} , is reached. K_L increases with pressure. Radiative transfer is less easily characterized. The radiative conductivity, K_R , is proportional to $T^3/\bar{\epsilon}$, where $\bar{\epsilon}$ is the mean extinction coefficient. If $\bar{\epsilon}$ were constant, the radiative conductivity would increase very rapidly with temperature, but $\bar{\epsilon}$ is not constant. It varies with the transparency of the material in the near infrared. In silicates, this transparency decreases with temperature but is not strongly affected by pressure. As a result, K_R may increase only slightly or not at all with increasing temperature.

The above discussion suggests that a technique of measuring both K_L and K_R at high temperature would be desirable. Such a technique has been developed during the course of this investigation. It uses a CO_2 laser as a slowly oscillating heat source at one face of a disk-shaped sample. The resulting decaying temperature waves in the sample produce radiation at the other sample face which is sensed by an infrared detector. In general, the radiation seen by the detector appears to originate

from some position within the sample, rather than at the back face as it would for an opaque sample. A relationship is derived between the phase of the observed signal and the lattice thermal diffusivity and mean extinction coefficient of the sample, from which both K_L and K_R may be calculated. To our knowledge, this is a new technique and is the first to allow conductivity measurements made on a small, partially transparent sample to be accurately applied to the case of bulk material as in situ.

Measurements on several ceramics and silicates up to 1900 °K have proven the effectiveness of the technique. The most noteworthy result is that the mean extinction coefficient of olivine single crystals with composition near to $Fe_{90}Fa_{10}$ increases with temperature rapidly enough to make the total conductivity, $K_L + K_R$, at 1900 °K only slightly larger than its room temperature value.

Applications of the results lead to the following specific observations: (1) The upper mantle thermal conductivity is less than if there were a large radiative contribution. As a result, steady state thermal gradients and temperatures are greater. (2) On a smaller scale, the thermal conductivity in the first 50 km of the oceanic mantle differs from its continental counterpart. In the oceanic case, the conductivity first increases, then decreases, and then increases again. In the continental

case, less fine structure exists, and the conductivity increases more smoothly. The conductivity immediately below the oceanic Moho is perhaps 30% higher than below the continental Moho. (3) The internal conductivity of an olivine moon is approximately constant and equal to about one-half the earth value. (4) A downgoing slab with 8 cm/yr velocity remains colder and has a somewhat higher temperature gradient near to its leading edge than has been previously determined.

REFERENCES

- Aronson, J.R., S.W. Eckroad, A.C. Emslie, R.K. McConnell Jr., and P.C. von Thuna, The application of high temperature radiative thermal conductivity of minerals and rocks to a model of lunar volcanism, Report to National Aeronautics and Space Administration, Contract NAS9-5840, A.D. Little Co., 1967a.
- Aronson, J.R., S.W. Eckroad, A.C. Emslie, R.K. McConnell Jr., and P.C. Von Thuna, Radiative thermal conductivity in planetary interiors, Nature, 216, 1096, 1967b.
- Aronson, J.R., L.H. Bellotti, and R.K. McConnell, Infrared spectra and radiative thermal conductivity of minerals at high temperatures, Report to the National Science Foundation, Contract NSF-C541, A.D. Little Co., 1968.
- Birch, F., and H. Clark, The thermal conductivity of rocks and its dependence upon temperature and composition, Am. J. Sci., 238, 529, 613, 1940.
- Burns, R.G., Optical absorption of silicates, in The Application of Modern Physics to the Earth and Planetary Interiors, edited by W.K. Runcorn, p. 191, Interscience, New York, 1969.
- Carslaw, H.S., and J.C. Jaeger, Conduction of Heat in Solids, 510 pp., Oxford University Press, London, 1959.
- Chung, D.H., Elasticity and equations of state of olivine: effects of iron/magnesium ratio, J. Geophys. Res., 76, (in press), October, 1971.

- Clark, S.P., Radiative transfer in the earth's mantle, Trans. Am. Geophys. Union, 38, 931, 1957.
- Clark, S.P., Heat conductivity in the mantle, in The Earth's Crust and Upper Mantle, Geophys. Monograph 13, edited by P.J. Hart, p. 622, American Geophysical Union, Washington, D.C., 1969.
- Cowan, R.D., Proposed method of measuring thermal diffusivity at high temperatures, J. Appl. Phys., 32, 1363, 1961.
- Deem, H.W. and W.D. Wood, Flash thermal diffusivity measurements using a laser, Rev. Sci. Instrum., 33, 1107, 1962.
- Devyamkova, E.D., A.V. Pemrov, I.A. Smirnov, B. Ya. Moizhes, Fused quartz as a model material in thermal conductivity measurements, Soviet Phys. Solid St., 2, 681, 1960.
- Engelmann, F., and H.E. Schmidt, Heat transport in solids, Nuclear Sci. Eng., 24, 317, 1966.
- Fujisawa, H., N. Fujii, H. Mizutani, H. Kanamori, S. Akimoto, Thermal diffusivity of Mg_2SiO_4 , and NaCl at high pressures and temperatures, J. Geophys. Res., 73, 4727, 1968.
- Fukao, Y., On the radiative heat transfer and the thermal conductivity in the upper mantle, Bull. Earthq. Res. Inst. Tokyo Univ., 47, 549, 1969.
- Fukao, Y., H. Mizutani, and S. Uyeda, Optical absorption spectra at high temperatures and radiative thermal

conductivity of olivines, Phys. Earth Planet. Interiors,
1, 57, 1968.

Goranson, R.W., Heat capacity, heat of fusion, in Hand-
book of Physical Constants, edited by F. Birch, J.F.
Schairer, and H.C. Spicer, p. 223, Geological Society
of America, New York, 1942.

Horai, K., Thermal conductivity of rock-forming minerals,
J. Geophys. Res., 76, 1278, 1971.

Horai, K., and G. Simmons, Thermal conductivity of rock-
forming minerals, Earth and Planet. Sci. Lett., 6,
359, 1969.

Hughes, D.S., and F. Sawin, Thermal conductivity of dielectric
solids at high pressure, Phys. Rev., 161, 861, 1967.

Jamieson, J.C., and A.W. Lawson, High temperature heat
conductivity of some metal oxides, J. Appl. Phys.,
29, 1313, 1958.

Joffe, A.F., Heat transfer in semiconductors, Can. J.
Phys., 34, 1342, 1956.

Joffe, A.F., Two mechanisms for the conduction of heat,
Soviet Phys. Solid St., 1, 141, 1959.

Joffe, A.V., and A.F. Joffe, Thermal conductivity of semi-
conductor solid solutions, Soviet Phys. Solid St.,
2, 719, 1960.

Kanamori, H., N. Fujii, and H. Mizutani, Thermal diffusivity
measurement of rock-forming minerals from 400° to
1100 °K, J. Geophys. Res., 73, 595, 1968.

Kanamori, H., H. Mizutani, and N. Fujii, Method of thermal

- diffusivity measurement, J. Phys. Earth, 17, 43, 1969.
- Kingery, W.D., Thermal conductivity: XII, temperature dependence of conductivity for single-phase ceramics, J. Am. Ceram. Soc., 38, 251, 1955.
- Kingery, W.D., J. Franci, R.L. Coble, and T. Vasilos, Thermal conductivity: X, data for several pure oxide materials corrected to zero porosity, J. Am. Ceram. Soc., 37, 107, 1954.
- Kittel, C., Introduction to Solid State Physics, 646 pp., John Wiley, New York, 1966.
- Kopal, Z., Radiative transport of heat in lunar and planetary interiors, Icarus, 3, 8, 1964.
- Kourganoff, V., Basic Methods in Transfer Problems, 281 pp., Dover Publications, New York, 1960.
- Krumhansl, J.A., Thermal conductivity in semiconductors, J. Phys. Chem. Solids, 8, 343, 1959.
- Lawson, A.W., and J.C. Jamieson, Energy transfer in the earth's mantle, J. Geol., 66, 540, 1958.
- Lee, D.W., and W.D. Kingery, Radiation energy transfer and thermal conductivity of ceramic oxides, J. Am. Ceram. Soc., 43, 594, 1960.
- Lee, W.H.K., Effects of selective fusion on the thermal history of the earth's mantle, Earth Planet. Sci. Lett., 4, 270, 1968.
- Lubimova, E.A., Heat transfer by excitons in the earth's mantle, in Problems of Theoretical Seismology and

- Physics of the Earth's Mantle, edited by V.A. Magnitskii, p. 60, Office of Technical Services, Washington, D.C., 1960.
- Lubimova, E.A., Theory of thermal state of the earth's mantle, in The Earth's Mantle, edited by T.F. Gaskell, p. 232, Academic Press, London, 1967.
- MacDonald, G.J.F., Calculations on the thermal history of the earth, J. Geophys. Res., 64, 1967, 1959.
- MacDonald, G.J.F., The deep structure of continents, Rev. Geophys., 1, 587, 1963.
- Madden, T.R., and C.M. Swift, Jr., Magnetotelluric studies of the electrical conductivity structure at the crust and upper mantle, in The Earth's Crust and Upper Mantle, Geophys. Monograph 13, edited by P.J. Hart, p. 469, American Geophysical Union, Washington, D.C., 1969.
- Miner, J.W., and M.N. Toksöz, Thermal regime of a downgoing slab and new global tectonics, J. Geophys. Res., 75, 1397, 1970.
- Orr, R.L., High-temperature heat contents of magnesium orthosilicate and ferrous orthosilicate, J. Amer. Chem. Soc., 75, 528, 1953.
- Parker, W.J., R. J. Jenkins, C.P. Butler, and G.L. Abbot, Flash method of determining thermal diffusivity, heat capacity, and thermal conductivity, J. Appl. Phys., 32, 1679, 1961.

Pitt, G.D., and D.

on natural an

subjected to

Interiors, 2,

Pitt, G.D., and D.

dense media a

other ferroma

mantle condit

189, 1970b.

Pomeranchuk, I., Th

temperatures 1

Phys. USSR, 4

Pridmore-Brown, D.C

in disks and r

Reed, J.S., and H.F

metal ions in

Soc., 52, 307,

Ringwood, A.E., Com

mantle, in The

Geophys. Monog:

American Geoph.

Romashin, A.G., The

materials, High

Sclater, J.G., and

terrestrial hes

tectonic and ge

- upper mantle of the earth, Geophys. J. R. Astr. Soc., 20, 509, 1970.
- Serizawa, M., Thermal diffusivity measurements of ceramics by a modulated electron beam technique, Jap. J. Appl. Phys., 8, 792, 1969.
- Shankland, T.J., Band gap of fosterite, Science, 161, 51, 1968.
- Shankland, T.J., Transport properties of olivines, in The Application of Modern Physics to the Earth and Planetary Interiors, edited by W.K. Runcorn, p. 175, Interscience, New York, 1969.
- Shankland, T.J., Pressure shift of infrared absorption bands in minerals and the effect on radiative heat transport, J. Geophys. Res., 75, 409, 1970.
- Shaw, D., and L.A. Goldsmith, An apparatus to measure the thermal diffusivity of irradiated fuel specimens at temperatures up to 1200° by the flash method, J. Sci. Instrum., 43, 594, 1966.
- Smith, R.A., Semiconductors, 496 pp., Cambridge University Press, Cambridge, 1961.
- Sonett, C.P., D.S. Colburn, P. Dyal, C.W. Parkin, B.F. Smith, G. Schubert, and K. Schwartz, Lunar electrical conductivity profile, Nature, 230, 359, 1971.
- Sparrow, E.M., and R.D. Cess, Radiation Heat Transfer, 322 pp., Brooks/Cole Publishing Co., Belmont, Calif., 1966.

- Spitzer, D.P., Lattice thermal conductivity of semiconductors: a chemical bond approach, J. Phys. Chem. Solids, 31, 19, 1970.
- Sugawara, A., The precise determination of thermal conductivity of pure fused quartz, J. Appl. Phys., 39, 5994, 1968.
- Toksöz, M.N., J.W. Minear, and B.R. Julian, Temperature field and geophysical effects of a downgoing slab, J. Geophys. Res., 76, 1113, 1971.
- Van De Hulst, H.C., Light Scattering by Small Particles, 470 pp., John Wiley and Sons, Inc., New York, 1957.
- Vishnevskii, I.I., and V.N. Skripak, Radiative heat transfer in polycrystalline corundum, High Temperature, 1, 403, 1969.
- Wang, C., Density and constitution of the mantle, J. Geophys. Res., 75, 3264, 1970.
- Wheeler, M.H., Thermal diffusivity at incandescent temperatures by a modulated electron beam technique, Brit. J. Appl. Phys., 16, 365, 1965.
- White, W.B., and K.L. Keester, Optical absorption spectra of iron in the rock forming silicates, Am. Mineralogist, 51, 774, 1966.
- Whitmore, D.H., Excitation processes in ceramics and anomalous increase in thermal conductivity at elevated temperatures, J. Appl. Phys., 31, 1109, 1960.
- Wolfe, W.L., Optical materials, in Handbook of Military

Infrared Technology, edited by W.L. Wolfe, p. 315,
Office of Naval Research, Department of the Navy,
Washington, D.C., 1965.

Wray, K.L., and T.J. Connolly, Thermal conductivity of
clear fused silica at high temperatures, J. Appl.
Phys., 30, 1702, 1959.

Zharkov, V.N., On the thermal conductivity coefficient of
the earth's mantle, Bull. Acad. Sci. USSR Geophys. Ser.,
776, 1958.

Zhuze, V.P., O.N. Novruzov, and A.I. Shelykh, Thermal
conductivity near a continuous phase transition,
Soviet Phys. Solid St., 11, 1044, 1969.

Ziman, J.M., Electrons and Phonons, 554 pp., Oxford
University Press, London, 1960.

APPENDIX

Some of the terms approximated or deleted in the mathematical analysis of the experiment given in Chapter 5 are included more completely and accurately in the actual analysis we use for computation. These terms are considered here.

Radiation Leaving the Sample

For the case of a relatively transparent sample, internal reflection can contribute measurably to the emerging radiation. With one internal reflection included, equation (5.1) is replaced by

$$R_{\lambda}(t) = \int_0^D e_{b_{\lambda}}(x, t) e^{-\epsilon_{\lambda}(D-x)} dx + \left(\frac{n-1}{n+1}\right)^2 \int_0^D e_{b_{\lambda}}(x, t) e^{-\epsilon_{\lambda}(D+x)} dx \quad (A1)$$

where n is the index of refraction of the sample.

Temperature in the Sample

The temperature in the sample is given by

$$T = T_0 + T(x, t) \quad (A2)$$

where T_0 includes all time independent terms. The term T_0 may be expanded in the form

$$T_o = T_f + A - Bx \quad (A3)$$

where T_f is the furnace temperature, A is the uniform sample temperature increase due to laser heating, and B is a small gradient also caused by laser heating. Equations for A and B are found by applying the boundary condition, equation (5.9), to the steady-state case. The expressions for A and B which result are

$$A = B \left[\frac{\frac{-K_{eff}}{8\sigma T_f^3} - \frac{1}{\epsilon} \left(e^{-\epsilon D} - 2 E_4(\epsilon D) - \frac{1}{3} \right)}{E_3(\epsilon D) - \frac{1}{2}} \right] + D \quad (A4)$$

$$B = \frac{\sigma (T_d^4 - T_f^4)}{K_{eff}}$$

where T_d is the "apparent temperature" of the sample measured by the detector in a pyrometer mode (as mentioned in Chapter 4). K_{eff} is given by equation (5.10).

A series expansion of the fourth power of sample temperature is needed to obtain the equivalent of equation (5.6). This expansion, carried to the third term, is

$$T^4 = T_o^4 + 4 T_o^3 T(x, t) + 6 T_o^2 T^2(x, t) \quad (A5)$$

With division by $4T_0^3$, and the dropping of time independent terms, equation (A5) becomes

$$R(t) = \int_0^D T(x,t) e^{-\bar{E}(D-x)} dx + \frac{3}{2T_0} \int_0^D T^2(x,t) e^{-\bar{E}(D-x)} dx \quad (A6)$$

where T_0 is found from equations (A3) and (A4). (With internal reflections, the additional term given by equation (A1) also must be included.)

Square Wave Components of Flux and Temperature

The square wave heat flux generated by the laser is given by

$$F = -2iF_0 \sum_{j=1}^{\infty} \frac{e^{ij\omega t}}{j} \quad (A7)$$

Equation (A7) replaces equation (5.7). The resulting sample temperature wave which replaces equation (5.8) is

$$T(x,t) = \sum_{j=1}^{\infty} \left[U_j e^{-\beta_j x} e^{i(j\omega t + \delta_j)} + W_j e^{\beta_j x} e^{i(j\omega t + \psi_j)} \right] \quad (A8)$$

where U_j , W_j , δ_j , ψ_j , and β_j are found for each value of j as in Chapter 5. In practice, the sum of the terms for $j=1$ and $j=2$ is used. The combination of equations (A8) and (A6) then gives the desired expression for output signal at the detector.

Biographical Note

The author was born in New York City in 1942 under the sign of Leo, which was, by chance, simultaneously in conjunction with the conflicting forces of Natura and Technologia. His youth in Fair Lawn, New Jersey was dominated by the forces of Technologia, and to fulfill part of his destiny, he entered the Massachusetts Institute of Technology in 1960. There, he studied physics and enjoyed philosophy until he graduated in 1964 with a Bachelor of Science in Physics. Following the designs of Technologia, he traveled to Phoenix, Arizona to create integrated circuits for the Semiconductor Products Division of Motorola Incorporated. But, there in the Western wilds, where the influence of Natura was strong and loving, the author discovered that the world was not a transistor. He leaped from his bath shouting 'Eureka! The world is a semiconductor!' He raced back to MIT but this time to enter the Department of Earth and Planetary Sciences, where, with the help of a National Science Foundation Graduate Fellowship he could apply his physics to the study of the earth. As destiny has decreed, Technologia and Natura have been united, and they are one.

P. S. Say Hello to the folks back home.